UNIVERSITÉ DU QUÉBEC EN OUTAOUAIS

AN EFFICIENT PHOTOVOLTAIC POWER CONVERSION SYSTEM IN PARTIAL SHADING CONDITIONS

THÈSE
PRÉSENTÉE
COMME EXIGENCE PARTIELLE
DU DOCTORAT EN SCIENCES ET TECHNOLOGIES DE L'INFORMATION

PAR

REZA SANGRODY

JANVIER 2025

Cette thèse a été évaluée par un jury composé des personnes suivantes :

Dr. Soulaimane Berkane ..... Président du jury

Dr. Hani Vahedi ..... Membre du jury

Dr. Miloud Rezkallah ..... Membre du jury

Dr. Shamsodin Taheri ..... Directeur de recherche

Dr. Ana-Maria Cretu ..... Codirecteur de recherche

Thèse acceptée le : 17 février 2025

To my wife, Narges, and my daughter, Vina, whose unwavering support and sacrifices have been the cornerstone of this accomplishment.

Remerciements

This research project was conducted under the supervision of Prof. Shamsodin Taheri and the co-supervision of Prof. Ana-Maria Cretu. I am deeply grateful to both of my supervisors for their professional and patient guidance, characterized by their open-mindedness and genuine dedication. Their unwavering encouragement and support throughout my Ph.D. studies will undoubtedly be invaluable to my future career and life.

Also, I would like to thank Mr. Ali Abdallah Guire and Mr. Abdelkrim Chebihi for their exceptional help, patience, and friendly support in the laboratory. Their willingness to assist and positive attitude have made a significant difference throughout this project.

Finally, I want to express my deepest love and gratitude to my parents, my wife, and my daughter for their unwavering love, support, and inspiration. I am also profoundly grateful to my friend, Edris Pouresmaeil, for his invaluable help and support throughout my Ph.D. studies.

TABLE OF CONTENTS

List of Figures

List of Tables

List of Abbreviations

PV Photovoltaic

PS Partial Shading

MPP Maximum Power Point

GMPP Global Maximum Power Point

LMPP Local Maximum Power Point

MPPT Maximum Power Point Tracking

KVL Kirchhoff's Voltage Law

KCL Kirchhoff's Current Law

I-V Current Versus Voltage

P-V Power Versus Voltage

P&O Perturb & Observe

PSO Particle Swarm Optimization

GWO Grey Wolfe Optimization

ANN Artificial Neural Network

U-B Upper Boundary

L-B Lower Boundary

STC Standard Test Condition

LHS Left-Hand Side Scanning

RHS Right-Hand Side Scanning

PSO Particle Swarm Optimization

CCM Continuous Conduction Mode

CRM Critical Conduction Mode

DCM Discontinuous Conduction Mode

RMS Root Mean Square

IC Integrated Circuit

Résumé

Exploiter efficacement l'énergie photovoltaïque (PV) exige d'intégrer une conception sophistiquée dans chaque partie d'un système de production d'énergie PV. Cette exigence est particulièrement soulignée lorsque ces systèmes de production sont confrontés à des conditions de fonctionnement particulières. Parmi elles, les conditions d'ombrage partiel (OP) sont les plus critiques. Les conditions OP posent des défis importants pour différentes parties d'un système de production PV en déformant la courbe caractéristique PV convexe et en créant plusieurs points de puissance maximale (PPM). Des problèmes tels que le blocage à un PPM local (PPML), un temps de suivi prolongé et des fluctuations de puissance élevées sont des défis courants pour l'algorithme de suivi PPM (SPPM) dans ces conditions. Outre ces problèmes, si les conditions OP ne sont pas correctement différenciées de celles sans ombrage, le système de production PV ne peut pas réagir efficacement. Par conséquent, un mécanisme de détection de OP élaboré est essentiel pour un système de production PV. De plus, les conditions OP affectent l'efficacité des convertisseurs terminaux en réduisant la valeur de la tension de fonctionnement. Le fonctionnement à une valeur de tension basse diminue l'efficacité du convertisseur et augmente la contrainte sur ses composants.

Ce projet de recherche vise à obtenir un système de production PV efficace en abordant ces principaux problèmes dans trois objectifs : 1) concevoir une technique MPPT complète pour suivre le PPM global du système avec une qualité de réponse élevée telle qu'un temps de suivi court et de faibles fluctuations de puissance générée. 2) concevoir un détecteur OP élaboré pour reconnaître rapidement l'état OP avec la capacité de fonctionner dans des conditions d'atmosphère dynamique. 3) introduire un convertisseur haute performance capable de fonctionner dans une large plage de tension d'entrée. Deux solutions sont proposées pour atteindre le premier objectif. Tout d'abord, un estimateur ponctuel initial est conçu à l'aide d'un réseau neuronal artificiel (RNA) permettant à l'algorithme SPPM de trouver le pic absolu avec précision. Le concept de

cellule dominante est introduit pour réduire le nombre infini de modèles OP en limitant la valeur de tension PPM entre deux limites. Ensuite, un ensemble de données est fourni en utilisant ce concept avec des valeurs d'irradiation et de température pour former un modèle RNA. Pour atteindre le deuxième objectif, l'origine des dysfonctionnements OP traditionnels est étudiée et une approche de détection OP basée sur un convertisseur est introduite pour fournir toutes les informations nécessaires sur le système de production PV. Sa procédure de détection de OP rapide, précise et indépendante le rend adapté à diverses applications telles que le fonctionnement dans une atmosphère dynamique, les convertisseurs d'équilibrage de puissance, etc. Pour atteindre le troisième objectif, un nouveau convertisseur boost est proposé qui utilise la résonance sur une large plage de tension d'entrée. En plus de minimiser les pertes de commutation, d'autres pertes de puissance causées par la résistance de l'inducteur et la chute de tension aux bornes de la diode sont considérablement réduites, ce qui se traduit par une efficacité élevée. Toutes les approches proposées ont été testées en laboratoire en concevant les convertisseurs électroniques de puissance requis et les résultats expérimentaux démontrent leur efficacité dans des applications réelles.

Cette recherche peut être considérée comme une contribution importante à la conception et au développement de systèmes de production PV hautement efficaces, en particulier dans les régions froides.

Mots clés : Algorithme MPPT basé sur un réseau neuronal artificiel, Balayage de la courbe I-V des panneaux PV, Détecteur d'ombrage partiel basé sur un convertisseur, Optimiseur de puissance PV basé sur la résonance.

Abstract

Harnessing photovoltaic (PV) energy efficiently demands incorporating sophisticated design into every part of a PV energy-generating system. This requirement is especially highlighted when these generating systems face particular operating conditions. Among them, partial shading (PS) conditions are the most critical. PS conditions cause significant challenges for different parts of a PV generation system by deforming the convex PV characteristic curve and creating multiple maximum power points (MPPs). Issues such as getting stuck at a local MPP (LMPP), prolonged tracking time, and high-power fluctuations are common challenges for the MPP tracking (MPPT) algorithm under these conditions. Besides these problems, if PS conditions are not differentiated from the non-shading ones correctly, the PV-generating system cannot react effectively. Therefore, an elaborate PS-detecting mechanism is essential for a PV-generating system. In addition, PS conditions affect the efficiency of the terminal converters by reducing the operating voltage value. Operating at a low voltage value decreases the converter's efficiency and increases the stress on its components.

This research project aims to achieve an efficient PV generation system by addressing these main problems through three objectives: 1) devising a comprehensive MPPT technique to track the global MPP of the system with high response quality such as a short tracking time and low generated power fluctuations. 2) designing an elaborate PS detector to recognize the PS condition fast with the ability to operate in dynamic atmosphere conditions. 3) introducing a high-performance converter with the capability of working in a wide input voltage range. Two solutions are proposed to achieve the first objective. First, an initial point estimator is designed using an artificial neural network (ANN) allowing the MPPT algorithm to find the absolute peak accurately. The dominant cell concept is introduced to reduce the infinite number of PS patterns by limiting the MPP voltage value between two boundaries. Then, a dataset is provided by employing this concept along with irradiation and temperature values to train an

ANN model. To fulfill the second objective, the origin of traditional PS malfunctions is investigated and a converter-based PS detecting approach is introduced to provide all the necessary information about the PV generation system. Its fast, accurate, and independent PS detecting procedure makes it suitable for various applications such as operating in a dynamic atmosphere, power balancing converters, etc. To meet the third objective, a new boost converter is proposed that employs the resonance over a wide input voltage range. Besides minimizing switching losses, other power losses caused by the resistance of the inductor and the voltage drop across the diode are reduced significantly, resulting in high efficiency. All the proposed approaches were tested in the lab by designing the required power electronic converters and the experimental results demonstrate their effectiveness in real-world applications.

This research can be considered as an important contribution to the design and development of highly efficient PV generation systems, especially in cold regions.

Keywords: Artificial neural network-based MPPT algorithm, Scanning the I-V curve of PV panels, Converter-based partial shading detector, Resonance-based PV power optimizer.

Chapter 1

Introduction

1.1 Overview

Using fossil fuels to generate electricity contributes significantly to global warming. For example, 29% of emissions in the USA is because of burning coal and natural gas to generate the required electricity [1]. On the other hand, distributed power-generating plants using renewable energies increase the stability of the power system by avoiding transferring energy through long transmission lines and decreasing the demand during peak hours. One problem with renewable energy resources is their intermittent phenomenon, which can be solved by employing various energy resources simultaneously. In this regard, generating electricity using PV systems is important even in cold counties [2]. In addition, the unique advantages of the PV generation system such as the ability to be installed as a small-scale power generation system and fast technological advances to increase their efficiency and reduce their cost make them one of the ideal sources of energy. Considering these advantages, many countries have incentive policies to extend PV-generating systems. Canada, as a world leader in employing renewable energies to generate electricity [3], has the strategy of accelerating the deployment of PV energy [4]. Generating electricity employing the PV system in cold countries such as Canada is challenging. For example, snowy weather, which can affect the PV panel performance, should be investigated to develop a sophisticated generation system that can quickly detect PS conditions and generate the maximum possible energy. In this context, this thesis studies some of the problems related to cold climate conditions and contributes by introducing novel solutions. The first study is dedicated to devising a comprehensive MPPT algorithm for PV generation systems. To this end, two methods are proposed.

The first one is an initial point estimator based on an ANN model and the second one is a novel idea to scan the I-V curve of the PV system to detect the system's GMPP. In both approaches, fast GMPP tracking with low-generated power fluctuations is the main goal. The second study is dedicated to detecting the PS condition which is a global problem of the PV system in cold regions. This mechanism is essential to avoid energy losses caused by getting stuck in an LMPP. Also, it is necessary for maintaining and supervising a PV system. Finally, in the third study, a new resonance-based boost power optimizer is introduced to reduce the losses caused by the switching operation, resulting in a highly efficient PV generation system.

This research helps to build a highly efficient PV system, especially in cold countries where the PV systems are more liable to be in PS conditions. Especially, the proposed solutions are designed for a wide range of applications from low-capacity rooftop PV systems to high-capacity PV power plants.

1.2 Motivation of Research

In 2022, 4.5% of the total global electricity was generated by the PV generation systems (in sum 1300 TWh) making PV electricity the third largest renewable energy after hydroelectricity and wind power generation. However, its absolute growth was the largest one this year. The growth trend in PV generation capacity exceeded the other renewable sources and continued to grow so that it possessed a third-quarter of the capacity additions in 2023 and it will remain until 2028 [5]. PV generation systems have some advantages compared to wind and hydropower that make them an interesting source of energy. They are more predictable, can be installed in low capacity such as domestic applications, do not have moving objects, their reliability is high and their maintenance is simple. Also, new technologies are increasing the efficiency of PV generation [6], therefore, almost all countries are investing in this source of energy. As shown in Fig. 1.1, Canada's cumulative installed PV power is increasing significantly and reached 5.8 GW in 2023 from 221 MW in 2010 [7].

New technologies are making PV generation a more efficient, affordable, and reliable source of energy. While the efficiency of the PV panel at its early introduction was 10%, nowadays the efficiency is up to 26% [8] and even NASA devised a new PV cell with an efficiency as high as 40% [9]. Besides increasing its efficiency, reducing the price is another reason to extend the PV generation. As shown in Fig. 1.2, the solar panel price

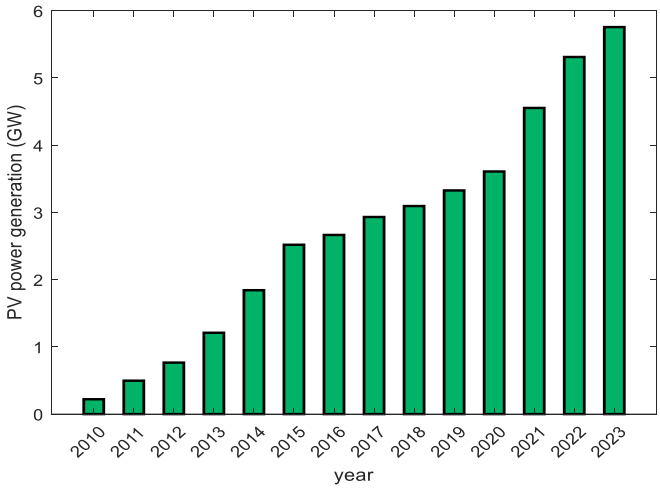

Figure 1.1: Canada cumulative PV generation from 2010 to 2023 [7].

was expensive at the beginning (100 $\$/W$ in 1975) but it decreased to 4.4 $\$/W$ in 2008. After this year, the rate of reducing the price increases significantly as it reaches around 0.26 $\$/W$ in 2022 [10].

Besides advancements in technology to increase the PV panels' efficiency and reducing their price, their utilization problems should be addressed to create more efficient PV generation systems. MPPT algorithms, specialized highly efficient power optimizers, and PV inverter features are some of the state-of-the-art research in this field. This thesis contributes to this research area by proposing innovative solutions associated with different problems of the existing PV generation systems.

1.3 Problem Statement

To build an efficient PV generation system, three main aspects should be taken into account. First, an MPPT algorithm or a replacement method should be designed to guarantee fast GMPP tracking with low power fluctuations. Second, the system should be equipped with a sophisticated PS detection mechanism to reinitiate the MPPT algorithm and avoid energy losses due to getting stuck in an LMPP. Finally, a highly efficient converter should be designed to work in a wide input voltage range and decrease losses such as switching and conducting ones. The following subsections discuss three problems associated with these three parts of an efficient PV generation system.

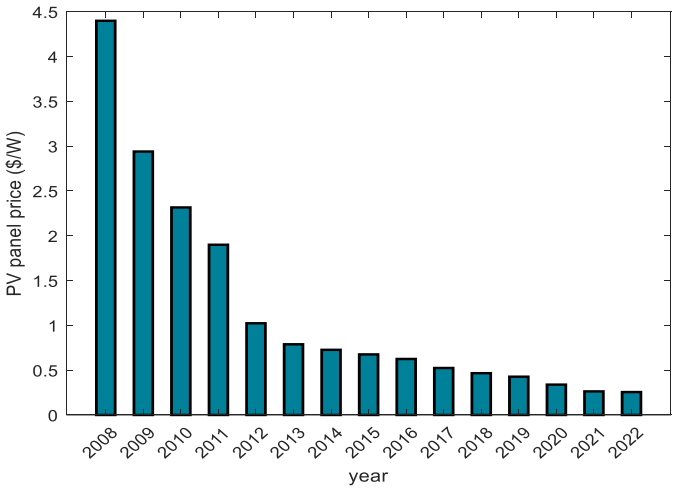

Figure 1.2: PV panel price from 2008 to 2022 [10].

1.3.1 Problem 1: Tracking the GMPP of the PV Generation in PS Conditions with High Response Quality

Despite the existence of various MPPT algorithms for PV generation systems, none of them can guarantee to track the GMPP with high-quality response characteristics such as tracking time and low fluctuations in the generated power. Therefore, there is a lack of a comprehensive solution in this field to maintain a high-quality response and track the GMPP, simultaneously. MPPT algorithms can be divided into traditional, optimization-based, and hybrid methods [11]-[17]. The main traditional MPPT methods are P&O [18]-[21], hill climbing [22]-[23], incremental conductance [24]-[25], incremental resistance [27], constant current [28]-[29], constant voltage [30], look-up table [31]-[32], curve fitting [33], etc. These algorithms are based on the convex P-V characteristic curve of a PV panel under uniform irradiation. In this condition, there is a single MPP on the P-V characteristics curve and the rate of power to voltage is positive at the left-hand side and negative at the right-hand side of the MPP. When PS conditions occur, the P-V characteristic curve is not convex and it has multiple MPPs, therefore, these algorithms get stuck in an LMPP resulting in high power losses in the generation system. Optimization-based algorithms were introduced to solve this problem. They select some initial duty cycles randomly, and then optimization techniques and heuristic methods are employed to track the GMPP in PS conditions. In addition, they were devised to improve other response qualities such as tracking time and power fluctuations in the tracking and steady-state periods. The main MPPT algorithms in this category are

PSO [34]-[41], GWO [42]-[46], cuckoo search [47], ant colony optimization [48], artificial bee colony [49], firefly algorithm [50], jaya algorithm [51], differential evolution [54]-[57], etc. Several initial points should be chosen and they should spread all over the entire search space to increase the probability of tracking the GMPP; therefore, the tracking time is longer in comparison to the traditional algorithms. Hybrid MPPT algorithms were introduced by combining traditional and optimization-based algorithms to take advantage of both of them [58]-[61]. For example, the PSO and P&O MPPT algorithms are combined to use the advantage of the PSO method in finding GMPP and the fast-tracking characteristic of the P&O method [58]. While hybrid methods offer many advantages compared to traditional and optimization-based algorithms, there is no guarantee to find the GMPP in the PS conditions.

A comprehensive solution for the MPPT algorithm should have the ability to track GMPP with certainty. In other words, it should be independent of the P-V curve characteristics or the number of duty cycles. Utilizing ANN techniques and scanning methods are two promising comprehensive solutions to track GMPP in PS conditions. Tracking GMPP by optimization-based MPPT algorithms in PS conditions depends on the number of initial duty cycles and their values. These quantities are chosen randomly; therefore, tracking the GMPP cannot be ensured. If the initial duty cycles are set close enough to GMPP or the search space is limited to an area around it, tracking the GMPP can be guaranteed. The I-V curve and its equivalent P-V curve change with different temperature and irradiation values. Consequently, the GMPP at a temperature and irradiation value can be estimated by applying the effects of these variables on the parameters of the P-V curve. In other words, the GMPP is a function of these variables; therefore, a dataset including the temperature, irradiation, and GMPP values can be prepared for a regression application. Then an ANN model can be trained to estimate this function. The output of this ANN model is the estimated value of GMPP and it can be used to limit the search space or choose the initial duty cycles for different MPPT algorithms. In this way tracking the GMPP will be ensured. This method was proposed in the previous research [62]-[65] but it still has some problems that should be addressed. The PS condition was considered a uniform pattern with different irradiation values of some PV panels within a string. This assumption and the resulting regression model are inaccurate because PS conditions occur as different shading values with an uneven shading pattern on the surface of a PV panel. However, the shading patterns are infinite, therefore, a method is required to limit their number

without losing the accuracy the GMPP voltage value. In addition, an approach should be designed to quantify them and employ the equivalent value for the regression model. Also, a measuring system such as a digital camera or irradiation sensors was used in the previous research to measure the irradiation value on each PV panel making it too complicated. Therefore, an approach should be designed to estimate the shading rate on the PV panel and avoid using irradiation sensors or digital cameras. Scanning the output characteristics of the PV panel provides all information such as open-circuit voltage, short-circuit current, irradiation value on the PV panel, the number and values of LMPP, and GMPP. Therefore, it can be considered as a comprehensive solution for the MPPT algorithms of the PV systems. There are two traditional implementations for this method. The first one is based on employing the boost power optimizer [66]-[74]. This converter is used for implementing the MPPT algorithm and boosting the PV voltage to the DC bus voltage. In the scanning application, the MPPT algorithm is paused and the converter operates for swiping the I-V curve of the PV panel. The advantage of this method is using the same converter both for the MPPT algorithm and for the scanning method. However, there are two drawbacks in the implementation of this method. First, the rating of the boost converter should be higher to implement the scanning method. Therefore, it cannot be implemented in an already installed system. Second, this method increases the temperature of the terminal capacitor caused by its fast discharging, consequently, the scan has a detrimental effect on the system lifetime. To alleviate this effect, there must be a long delay between two consecutive scans. Due to this delay, this method is not fast in comparison to the other MPPT algorithms. The second scanning method was introduced to avoid a short circuit at the terminal capacitor [75]-[78]. In this method, a separate scan circuit is placed between the PV panel and the terminal capacitor. In addition, an auxiliary capacitor is used for the scanning operation; therefore, the terminal capacitor does not suffer from the short-circuit current. This circuit has the same problem as the previous scanning method because the auxiliary capacitor experiences a high short-circuit current and its lifetime decreases.

1.3.2 Problem 2: A PS Detection Method Independent of Shading Occurrence Rate and Operating Point

The second problem in building a highly efficient PV generation system is the need for a fast and accurate PS condition detection method. The current PS-detecting methods can be categorized into two main groups. The first one is based on using digital cameras which can be counted as direct methods [79]-[83]. Besides detecting the PS condition, the rate of shading on the PV panels can be estimated by image processing methods. This method has several disadvantages that make it unfavorable for PS detection applications. This method increases the complexity and decreases the reliability of the system. On the other hand, image processing methods demand complicated processors. Regarding these issues, the second method, which implements the PS detection indirectly by measuring some parameters of the output characteristics such as the PV current and voltage, is more interesting and economical. This group can be divided into two categories to explain their operation, advantages, and disadvantages. The first category is based on measuring and calculating the difference between two samples of the generated power values [84]-[86]. This method is mainly used in the MPPT algorithm for reinitialization. The generated power changes suddenly for an operating voltage when the PS condition occurs; therefore, it can be a good criterion to detect the PS occurrence. On the other hand, the generated power is calculated almost in all MPPT algorithms, consequently, detecting the PS condition can be implemented easily using this approach. The main advantage of this method is its simplicity. But this method shows malfunction for three reasons. First, if PS happens slowly, the difference between two consecutive values is not high enough to be detected as the PS condition. Second, if the irradiation value decreases significantly but its pattern on the PV panel is uniform, the difference between two consecutive power values is high and the PS condition is detected. In an MPPT application, this problem does not affect the operation of the system, but in other applications such as power balancing, it causes a malfunction of the system. Finally, the third problem happens when the irradiation value on the PV panel is low and the shading pattern is even. Then the irradiation value becomes high and the PS occurs. In this condition, the PS is not detected. The second category of the current PS detection methods is based on measuring the anti-parallel diode voltage [87]. The anti-parallel diode of a PV panel in an array becomes forward-biased when the panel is in the shading condition and the current is higher than its short-circuit

current. Consequently, a small positive voltage across the anti-parallel diode means its parallel panel is in the PS condition. The implementation of this method is simple, but its accuracy depends on the operational point of the system. For example, if the GMPP is far from the open-circuit voltage of the PV panel, all diodes become reverse-biased and the PS condition is not detected.

1.3.3 Problem 3: Boost Power Converter Losses in Wide Input Voltage Ranges

Along with a sophisticated MPPT algorithm and a fast PS detection method, a low-loss power optimizer converter is crucial for a highly efficient PV generation system. This converter should operate in a wide input voltage range because when the PS conditions occur, it should be able to track the GMPP in low voltage ranges. Employing resonance to reduce converter losses is challenging in this condition and demands designing specialized converters. In a photovoltaic system, the output voltage of a boost power optimizer is in series with other power optimizers to generate the DC bus voltage for a solar string inverter. The inverter maintains the output voltage of the power optimizer at a constant value; therefore, the power optimizer controls the input voltage by adjusting the duty cycle to implement the MPPT algorithm. The valley switching method can be employed to increase the power optimizer's efficiency. This method uses the resonance between the converter's inductor and the output parasitic capacitance of the converter's MOSFET when the converter's diode turns off [88]-[100]. In the current control mode, the inductor's current rises when the MOSFET turns on until a reference current and it falls once the MOSFET turns off. When the current reaches the reference maximum current, a resonance occurs between the converter's inductor and the parasitic capacitance of the MOSFET and diode. The converter's diode turns on when its capacitance's voltage tends to be a positive value; therefore, the inductor's current falls to zero, and at this moment the converter's diode turns off. At this time, another resonance occurs between the previous elements that can be used to decrease the ON-state switching losses. It means that the next switching of the MOSFET is successfully done at the minimum point of this oscillating voltage. If the input voltage is more than half of the output voltage, the switching losses are not zero. This condition occurs when the non-shading condition exists and the voltage of the GMPP is close to the output voltage value. These losses are important from another viewpoint because the system usually

works in non-shading conditions, therefore, the efficiency of the system decreases significantly. Regarding this fact, using resonance is not helpful to reduce the boost power optimizer losses, consequently, a new topology should be introduced to take advantage of the resonance and increase the converter efficiency.

1.4 Objectives of Research

In the context of the problems defined in the previous section, designing a highly efficient PV-generating system, especially under PS conditions necessitates employing precise attention in its critical parts. As explained before, despite devising various MPPT algorithms for PV-generating systems, tracking the GMPP in PS conditions is not guaranteed. This issue and the low response quality increase the power losses in a PV generating system. In addition, a highly sophisticated MPPT algorithm is useless without a precise and fast PS detecting mechanism. Moreover, the potential generated power decreases during the PS condition, therefore, having a highly efficient converter at the terminal of the PV panel is more critical to supply sufficient energy to the load. Regarding these challenges, the goal of this thesis is to participate in the PV-generating system improvement by addressing its main issues and designing a low-loss PV-generating system that involves the development of new concepts, methods, and converters. To this end, the thesis has the following objectives:

- **Objective 1:** Propose, develop, implement and test a comprehensive MPPT algorithms in PS conditions employing an ANN model and a scanning method
- **Objective 2:** Propose, develop, implement and test a fast and independent operating PS detector
- **Objective 3:** Propose, develop, implement and test a high-efficiency boost power converter based on the resonance in a wide input voltage range

1.5 Methodology

To fulfill the above-mentioned objectives, this study is conducted based on preparing the required dataset in PS conditions, designing the I-V scanning, PS detector, highly efficient resonance-based converters, and validation employing simulation and experimental approaches. The proposed methodologies are described below in brief.

1.5.1 Methodology of Objective 1

An accurate ANN model is trained and used as the initial point estimator of the MPPT algorithms. The dominant PV cell concept is introduced to reduce the number of PS patterns over a PV module without losing accuracy. Then, a dataset is created by changing the shading value of the dominant cell and applying the effect of temperature and irradiation values on the I-V output characteristic. The shading value of the dominant cell is measured directly by employing the terminal boost converter; therefore, the implementation does not require to detect the PS pattern. Finally, a test setup was prepared and the ANN model was implemented in TMS320F28335 DSP microcontroller to validate the proposed method.

Another comprehensive MPPT technique is proposed by introducing a new idea to scan the I-V characteristic without applying a short circuit at the terminal capacitor. The output capacitance of a PV panel is negligible, therefore, the terminal capacitor behaves similarly to a voltage source if a short voltage pulse is applied between the PV panel and the terminal capacitor. In other words, the terminal voltage is constant while the PV voltage changes to satisfy the KVL. Based on this idea, an inductor is placed between the PV panel and the terminal capacitor. A converter is connected to the inductor to apply positive and negative voltage pulses. The right-hand and left-hand sides of the operating point are scanned by these pulses. Finally, the output I-V curve is achieved and provides all the required information about the GMPP, short-circuit current, and open-circuit voltage. The design procedure is explained by regarding an acceptable voltage drop at the terminal voltage in the worst operating condition. The pulse length and the inductor value are calculated as the main parameters of the converter. To validate the idea, a prototype circuit is designed and connected to the PV panel in different PS conditions. Then the scanned I-V curve was acquired to show the accurate and fast performance of the converter.

1.5.2 Methodology of Objective 2

A novel idea is proposed to detect the PS conditions fast and independent of the operating voltage value. Also, the speed of the PS occurrence does not have any effect on the PS detection result. A current pulse generator is placed in between the PV panel and the terminal capacitor to apply a rising current ramp. The I-V characteristic of the PV panel is detected and the PS condition is identified if there is any step on this

curve. A wave-shaping converter is used to generate the current ramp by switching the voltage drop across an inductor. The design of the PS detector converter is detailed by calculating the current pulse length and the inductor value under the worst operating conditions to ensure high-quality performance. In addition, the minimum switching frequency of the wave-shaping converter is calculated based on the CRM boundary to have low current fluctuations. Finally, a prototype circuit was prepared to evaluate the performance of the proposed idea. Some tests were conducted by connecting the PS converter to the PV panels in different PS conditions. The experimental results were provided which demonstrate the high performance and accuracy of the PS detector.

1.5.3 Methodology of Objective 3

The resonance voltage equation across the MOSFET of the boost converter in the traditional configuration is calculated to evaluate its performance in PS and non-shading conditions. Then, a new configuration is proposed to increase the efficiency by employing valley switching. Coupled inductors are used to minimize the resonance voltage minimum value to zero. This resonance voltage is calculated to design the converter. Also, the other main sources of losses such as the conducting losses of the MOSFET, inductor, and diode are calculated and compared to their equivalent in the traditional converter. Finally, a prototype converter is designed to verify the analyses. Some tests were conducted in a wide input voltage range with a constant output voltage to evaluate the performance in PS and non-shading conditions. The experimental results demonstrate the correctness of the analyses and the high efficiency of the proposed converter.

1.6 Statement of the Originality of the Thesis

The originality and contribution in each objective of this research are discussed separately.

1.6.1 GMPP Estimator and Stability and Steady State Analyses of MPPT Algorithms in the PS Conditions

Some research proposed GMPP estimators as a comprehensive solution to solve the problems of the MPPT algorithm. However, they did not take into account the PS

pattern and the shading rate on a PV panel while these parameters influence the value of the GMPP voltage. There are two reasons behind this problem. First, there are infinite PS patterns on a PV panel and second, a method is required to quantify the shading pattern. In this thesis, a method is introduced to limit the number of PS patterns. By defining the dominant PV cell and dominant PV module, the number of PS patterns can be limited without loss of accuracy. Therefore, a dataset can be prepared for an ANN MODEL to estimate the GMPP. In addition, a method is introduced to quantify the shading rate on a PV panel without using digital cameras. Moreover, stability and steady-state analyses of the PSO MPPT algorithm are performed for the first time in the literature. Apart from calculating the range of parameters for the stable response, it is shown that the GMPP estimator is essential in the PSO MPPT algorithm to avoid getting stuck at an LMPP. Also, the speed of tracking increases, and the fluctuation of power decreases significantly.

1.6.2 A novel method for scanning the output characteristics of the PV Panel

There is an electrolytic capacitor at the terminal of PV panels and applying a short circuit at this point causes a high amount of short-circuit current. Therefore, the probability of the terminal capacitor failure increases because of high temperature. A short circuit is required in the previous scanning methods; consequently, they have a detrimental effect on the lifetime of the system. In addition, the time interval between two consecutive scans should be high enough to avoid capacitor failure. In this thesis, a new idea for scanning the output characteristics of the PV panels is introduced which does not require a short circuit at the terminal capacitor; therefore, it does not have a detrimental effect on the lifespan of the system. Also, scans can be done consecutively without any delay between them. As a result, this scanning method can be used as a comprehensive solution to solve the problems of the GMPP tracking algorithms. Moreover, the scan circuit operates independently and does not require any change in the rating of the power optimizer elements such as its MOSFET and inductor. Independent operation of the scan system makes it suitable for verifying the PV panel condition. Consequently, it can be used for monitoring purposes if a problem occurs in the PV generation system.

1.6.3 Converter-Based and Fast PS Detection Converter

The current PS detection techniques have some deficiencies. To address them, the proposed PS detector is designed to apply a short-period pulse to the PV panel. Therefore, any difference in the shading ratio on the PV modules is revealed fast no matter if the difference is small or large. In addition, the rate of change in the PS occurrence does not influence the detection procedure of the proposed method. While, if the PS rate is slow, the PS detection method based on the comparison of two power values cannot detect the PS condition. Also, unlike the anti-parallel voltage drop measuring method, the proposed method operates well at low current operating points and the operating point does not affect its PS detection.

1.6.4 Introducing a New Resonance-Based Converter for PV Generation System

The proposed converter uses a coupled inductor and its resonance with the intrinsic capacitance of the MOSFET to implement the valley switching. This configuration is novel and the size of the coupled inductor as the most expensive component of the converter is the same as one of the traditional converter. Also, an extra parallel capacitor is not required for the resonance; therefore, the final price of the proposed converter is almost the same as the traditional one while offering greater reliability. In addition, contrary to the other resonance converters which only try to decrease the switching losses, other power losses are also reduced in the proposed converter.

1.7 Thesis Outline

The individual chapters of this thesis are organized as follows.

Chapter 2 is a literature review. The challenges of a PV system in PS conditions are explained in brief followed by three sections associated with the previous research one for each objective of this thesis. The existing MPPT algorithms and the efforts to devise a comprehensive MPPT technique are described in this section. The current PS detecting methods and their deficiencies are reviewed in another section to highlight the necessity of a fast and accurate PS detector. Finally, the last section is dedicated to using the resonance in the boost power optimizer for a wide input voltage range caused by the operation in the PS conditions.

Chapter 3 proposes two novel MPPT techniques as a comprehensive approach for PV generation systems. The first approach uses an ANN model as an initial point estimator, with the PSO optimization method applied as the MPPT algorithm. The second part is a new method to scan the I-V curve of the PV system without any detrimental effect on its lifetime. The implementation, design, and experimental verification are explained for both approaches.

Chapter 4 introduces a converter-based fast PS detecting method. The idea is described followed by its implementation and design procedure. The experimental results for a prototype circuit are presented at the end of this chapter to verify the effectiveness of the new approach in different PS scenarios.

Chapter 5 is dedicated to a novel boost power optimizer topology. It is designed to harness the resonance phenomena in a wide input voltage range. The operation states and the loss analyses are described for the traditional and proposed converters. A comparison is performed for the main sources of losses between the two converters to illustrate the high efficiency of the proposed converter. Finally, the experimental results are presented for a prototype circuit in low and high input voltage values to verify the analyses.

Chapter 6 summarizes the work presented in this thesis, highlights its contributions, and outlines potential topics for future research.

1.8 List of Publications

A list of the papers and reports derived from this project, which have been published so far or have been submitted, is given as follows:

Journal Papers:

[R1] Reza Sangrody, Shamsodin Taheri, Ana-Maria Cretu and Edris Pouresmaeil, "An Improved PSO-Based MPPT Technique Using Stability and Steady State Analyses Under Partial Shading Conditions", IEEE Transactions on Sustainable Energy, vol. 15, no. 1, pp. 136-145, January 2024.

[R2] Reza Sangrody and Shamsodin Taheri, "An Online Scanning Method to Detect the Output Characteristics of Photovoltaic Panels", IEEE Transactions on Industrial Electronics, vol. 71, no. 9, pp. 10831-108405, September 2024.

[R3] Reza Sangrody, Shamsodin Taheri and Edris Pouresmaeil, "Fast Partial Shading Detection and Performance Analyzing Method for Photovoltaic Generation", IEEE Transactions on Industrial Informatics, Under Review.

[R4] Reza Sangrody, Shamsodin Taheri and Edris Pouresmaeil, "High-Efficient Photovoltaic Power Optimizer Based on the Intrinsic Resonance and Coupled Inductors", IEEE Transactions on Power Electronics, Accepted, Early Access, January 2025.

Conference Papers:

[R5] Reza Sangrody, Shamsodin Taheri and Ana-Maria Cretu, " Scanning of I-V Curves of PV Generation Systems Using a Full Bridge Configuration", IEEE CCECE 2024 Conference.

Chapter 2

Literature Review

2.1 Introduction

In this chapter, first, the challenges of a PV system experiencing PS conditions are described. It is then followed by a literature review addressing the issues of traditional MPPT algorithms, conventional PS detection methods, and common power optimizer converters. The origin of traditional MPPT algorithms problems is clarified for their three categories namely traditional, optimization-based, and hybrid approaches. Then, the existing PS detectors are reviewed to provide an insight into their problems under different PS conditions. Finally, the literature related to the possibility of employing the resonance phenomenon to decrease power losses in wide input voltage ranges caused by the PS condition is discussed.

2.2 Challenges of a PV System Facing PS Conditions

PS conditions refer to uneven irradiation values on the surface of a PV panel or different irradiation values on one or several PV panels in a string. Therefore, the I-V curve or equivalently the P-V characteristic of the PV panel, differs from that in non-shading conditions. Multiple MPPs appear in this situation, causing energy losses in traditional PV systems [11]-[17]. If the GMPP of the P-V characteristic has a lower voltage value in comparison to the open-circuit voltage, the system may get stuck in an LMPP resulting in significant energy losses. In a PV generation system, the voltage at the GMPP changes due to atmospheric conditions such as insolation value and temperature. Therefore, the

system should continuously track this point to harvest the maximum potential energy. This operation is typically implemented by an MPPT algorithm to set the output voltage of the PV panels at the GMPP. Traditional MPPT algorithms are designed under the assumption of a single MPP in the P-V characteristic and of the convexity of this curve [18]-[33]. From this perspective, the PS condition is a significant challenge, leading to several issues such as getting stuck at an LMPP, long tracking time, and fluctuations of the output power during both tracking and steady-state periods, as reported in the research [34]-[61].

Every sophisticated PV generation system should have a PS detection mechanism. This mechanism is utilized within the MPPT algorithm to reinitialize and prevent getting stuck in an LMPP. Also, in other applications such as power balancing methods which aim at increasing the generated power, this detection is essential for their activation [101]-[107]. The traditional PS detection methods rely on comparing two samples of the generated power values and if their difference exceeds a predefined value, the PS condition is detected [84]-[86]. Monitoring the voltage drop across the terminal diodes is another method in this regard [87]. However, my thesis illustrates that all these methods exhibit malfunctions under certain conditions.

The power optimizer converter acts as an interface between the PV panels and the load. This converter increases the level of the PV panel voltage to the required value for the DC bus which supplies a combination of loads such as battery chargers, DC loads, and grid forming or grid following inverters. Another important task of this converter is adjusting the PV panels' voltage at the voltage value related to the GMPP. The reference value for this converter is usually prepared by the MPPT algorithm. In PS conditions, the voltage value of GMPP tends to be low; therefore, this converter should have a high voltage ratio to increase this value to the DC bus voltage level [108]-[109]. Also, the generated power decreases in PS conditions; consequently, if the converter has high power losses, the efficiency of the system decreases significantly.

2.3 Review of MPPT Algorithm Under PS Conditions

Traditional, optimization-based, and hybrid methods are three main categories of the MPPT algorithm in the PV generation systems [11]-[17]. The majority of MPPT algorithms are in the traditional category, all of which are based on the convex P-V curve of a PV panel under uniform irradiation. In this situation, there is a single MPP

and the rate of power to voltage is positive at the left-hand side and negative at the right-hand side of the MPP. P&O MPPT algorithm is one of the traditional algorithm that is used a lot in boost power optimizer and inverter applications [18]-[21], In this algorithm, the output voltage and current of the PV panel are measured to calculate the output power at a predefined interval. Subsequently, the current power value is compared with the previous one. If the difference is zero, the MPP is attained and the PV voltage should be kept constant. The PV voltage should be increased if the difference between two power samples and two voltage samples has the same sign, otherwise the output voltage should be reduced. The output voltage of the PV panel is adjusted by controlling the duty cycle of the power optimizer. Therefore, a proportional-integral controller or a constant step is used to control the duty cycle. This algorithm is simple and has the ability to track the GMPP of the P-V curve when the irradiation on the PV panel is uniform. However, if the PS occurs, it tracks the closest MPP to the initial point; therefore, it is liable to get stuck in an LMPP. Another algorithm in this category is the hill climbing MPPT algorithm [22]-[23] which is similar to the P&O method. The main difference lies in the fact that the variation in the generated power affects directly the duty cycle in the hill climbing MPPT algorithm which makes its implementation easier compared to the P&O MPPT algorithm. However, it has the same deficiencies as the P&O algorithm. These two MPPT algorithms utilize the slope of power value versus voltage value to adjust the PV voltage value. However, the slope of the PV current value versus the PV voltage value can be used directly to adjust the PV voltage. This method provides a better dynamical response and reduces the effect of noise and fluctuations. The incremental conductance MPPT algorithm employs this approach [24]-[25]. At the MPP, the derivative of power versus voltage is zero, therefore, it can be shown that the dynamical conductance at this point is equal to the rate of the PV current value to the PV voltage value. Also, It is greater than the rate of the PV current to the PV voltage on the left side and smaller than this rate on the right side of the MPP point. As a result, a comparison between the instantaneous conductance value and the ratio of the PV current to the PV voltage can be employed as a good criterion to detect the MPP. This condition is satisfied in all MPPs no matter if they are the GMPP of the P-V curve or not; therefore, this algorithm is liable to get stuck at an LMPP. The PV voltage value is greater than the PV current value at the MPP; therefore, the rate of voltage to current is greater than its inverse value. In other words, in real applications where there exist noise and fluctuations [26], if the dynamic resistance is employed instead of the dynamic

conductance, the MPPT algorithm can track the MPP more accurately. In this regard, incremental resistance MPPT algorithm [27] was introduced, however, this algorithm is based on the convexity of the P-V curve similar to the previous MPPT algorithms and is liable to get stuck at an LMPP. Fast MPP tracking procedure can be achieved by constant current [28]-[29], constant voltage [30], look-up table [31]-[32], and curve fitting [33] MPPT algorithms. These methods are not accurate enough because they are based on some assumptions that are affected by atmospheric conditions. For example, the voltage value at the MPP value is equal to $0.8 \times V_{oc}$ where V_{oc} is the open-circuit voltage value of the PV panel. This value and the coefficient changes as a function of temperature, irradiation value, type of PV panel, etc. There are other traditional MPPT algorithms such as beta method, current sweep approach, one cycle control, etc. and all of them are based on the convexity of the P-V curve, as a result, they are prone to get stuck in an LMPP in the PS conditions.

Getting stuck in an LMPP is the main problem of traditional MPPT algorithms and optimization-based MPPT techniques were employed to solve this problem. Selecting some initial points and evolving them using an optimation approach are the common characteristics of all these MPPT methods. Besides tracking the GMPP of the system, improving other response qualities such as tracking time and power fluctuations are other objectives of these algorithms. PSO MPPT algorithm is one of the powerful methods in this category [34]-[41]. The PSO method is a mathematical interpretation of the collaborative behavior exhibited by creatures in nature to find food or for other purposes. Therefore, in this method, the optimal position which is the maximum value of a cost function is searched by the cooperation among particles in a search space. The evolution of each particle is controlled by its own best position and the globally best position found by the entire community of particles so far. Particles in the MPPT application are duty cycles of a DC-DC converter, therefore, they are scalar values which makes the implementation easier. Changes for a particle have three components. The first component keeps the particle in the previous trajectory while the second and the third components tend to change the particle's position towards its best position and the global best position found so far. A lot of duty cycles as initial particles should be generated and spread all over the search space in this algorithm to guarantee finding the GMPP. Otherwise, the GMPP may be missed and an LMPP is found. Another solution to avoid getting stuck in an LMPP is decreasing the difference between the new and old duty cycles by selecting small coefficient values to have small changes. Therefore, the

PSO MPPT algorithm has long tracking time, consequently, the fluctuation in the generated power and the power losses are high. Also, there is no criterion to determine the sufficient number of particles (duty cycles) to ensure the GMPP tracking. In addition, this optimization method is based on random numbers; therefore, the generated power fluctuations caused by duty cycle variations during the tracking phase will be significant. GWO MPPT algorithm is another method in this category. GWO is an optimization method inspired by the hunting behavior of grey wolves which are one of the most successful predators in nature. In GWO MPPT algorithm, the best, second best, and third best duty cycles are chosen as alpha, beta, and delta wolves which determine how the duty cycles should change [42]-[46]. The other duty cycles are called omega wolves and their values do not influence the value of other duty cycles. The distance of each duty cycle to alpha, beta, and delta duty cycles is calculated and its average is used for its updating. In general, this algorithm is similar to the PSO MPPT algorithm, therefore, it suffers from the same deficiencies. Cuckoo search [47], ant colony optimization [48], artificial bee colony [49], firefly algorithm [50], jaya optimization [51], team-game optimization [52], and whale optimization [53] are some of other MPPT algorithms in this category which are based on cooperation between the individuals. In addition, there are other MPPT algorithms based on competitive algorithms such as genetic and differential evolution MPPT algorithms [54]-[57].

The traditional MPPT algorithms have the problem of getting stuck at an LMPP in the PS conditions. On the other hand, the optimization-based MPPT algorithms have long tracking times and high power fluctuations. Therefore, hybrid MPPT algorithms were devised to solve the previous MPPT algorithm problems by combining them [58]-[61]. Despite better performance in comparison to traditional and optimization-based algorithms, finding the GMPP still cannot be guaranteed. Traditional MPPT algorithms may get stuck in an LMPP because they are designed based on the convex P-V curve in non-shading conditions. Also, optimization-based MPPT algorithms may fail to track the GMPP because there is no criterion to choose the number of duty cycles. Therefore, despite the fact that combining these two groups of MPPT algorithms improves the response qualities, it cannot solve the problem of getting stuck in an LMPP.

Tracking the GMPP of the system independent of the initial point values and the PV output characteristics is the main feature of a comprehensive MPPT algorithm. The ANN model and scanning of the output I-V curve are employed to fulfill this feature in the PS conditions. The performance of the optimization-based MPPT algorithms

depends on the value and number of initial points. Therefore, choosing them randomly which is common cannot guarantee tracking the GMPP of the system. In other words, limiting the search space around the GMPP and spreading the initial points in this area ensures finding the GMPP. The irradiation, temperature, and shading value change the I-V curve of the PV panel and its GMPP voltage value. It means that the voltage value associated with the GMPP is a function of these atmospheric parameters. Therefore, a regression application can be used to calculate the GMPP value by preparing a dataset. This function is highly nonlinear and the linear regression method is not a good choice in this application as shown in Appendix A. Therefore, an ANN model can be used to solve this problem. The initial point can be spread around the GMPP value from the output of this model [62]-[65]. This method is promising however it has some problems that should be addressed to make it more effective. The PS patterns are infinite on a PV panel, therefore, the previous research regarded the PS as some PV modules with different uniform irradiation in a string of the PV modules. This assumption is not correct and produces a large error, consequently, their ANN model is not accurate. Another obstacle to having a precise model is quantifying the PS pattern. In general, a method should be devised to limit the number of PS patterns without losing the accuracy and to quantify them and use this value for the ANN model. Finally, if the shading rate is measured electrically instead of using digital cameras or irradiation sensors, the resulting system is more reliable and simple.

The I-V characteristic of the PV panel provides almost all information such as open-circuit voltage, short-circuit current, irradiation value on the PV panel, the number and values of LMPP, and GMPP. On the contrary to other MPPT techniques, sweeping this curve can be used to track the GMPP directly and can be counted as a comprehensive MPPT method. Two approaches were introduced in the literature for this technique. In the first one, the terminal boost converter is used for scanning the I-V curve as shown in Fig. 2.1 [66]-[74]. In this application, this converter is used both for implementing the MPPT algorithm and the scanning the I-V curve. First, the system is working at the operational point (OP) then the MOSFET (Q) turns on to apply a short circuit at the terminal of the PV panel, therefore, the PV current and voltage become I_{SC} and zero, respectively. The scan starts at this point by turning off the MOSFET and sampling the PV current and voltage. The PV current decreases from short-circuit current to zero because the output voltage (V_O) is greater than the PV voltage even when the PV voltage is at its open-circuit voltage. The advantage of this method is using the same

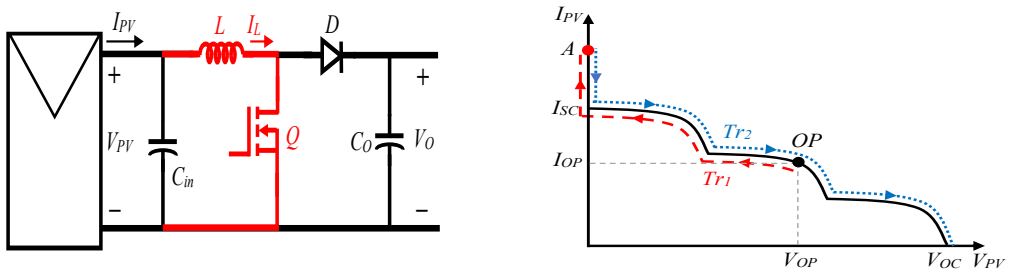

(a) (b)

Figure 2.1: The boost power optimizer scanning method. (a) The boost power optimizer. (b) The scanning trajectories for the boost converter.

converter both for the MPPT algorithm and for the scanning method. However, there are some drawbacks in the implementation of this method. When the MOSFET applies a short circuit at the terminal of the PV panel, the maximum current value is high in comparison to the operating current, therefore, the MOSFET and the inductor should have higher rating values in comparison to the usual boost power converter. Another disadvantage of this method is increasing the temperature of the terminal capacitor (C_{Tr}) caused by its fast discharging, consequently, the scan has a detrimental effect on the lifetime of the system. To decrease this effect, there must be a long delay between two consecutive scans. Regarding this delay, this method is not fast in comparison to the other MPPT algorithms. The second scanning method is based on employing a separate scanning circuit which is placed between the PV panel and the terminal capacitor [75]-[78]. This circuit has its own capacitor as an auxiliary one for the scanning procedure instead of using the terminal capacitor. In this way, the terminal capacitor does not experience the shout circuit and its effects. However, the auxiliary capacitor should be sufficiently large to provide enough time constant. Also, this capacitor suffers from the same problem as the terminal capacitor of the first scanning method. Therefore, both scanning methods cannot be reliable in practice.

2.4 Review of the PS Detection Approaches

There are two main methods for PS detection namely direct and indirect approaches. In the first one, image processing techniques are used by analyzing the output of digital cameras to detect the PS conditions and the depth of shading over the PV panels [79]-

[83]. Increasing the complexity and decreasing the reliability of the system are some disadvantages of this method compared to the second one. The second approaches detect the PS condition by measuring the PV current and voltage, therefore, they are considered indirect methods. They can be divided into two categories based on their PS detection technique.

The generated power value changes suddenly when the PS occurs, therefore, the difference between two power value samples is a good criterion to detect the PS condition [84]-[86]. Also, the PV power value is calculated almost in all MPPT algorithms, therefore, this method can be implemented easily in the system. Fig. 2.2-(a) illustrates the operation of this method on the P-V output characteristic of a PV system. The solid blue curve shows the P-V output characteristic before the PS condition and the operating power is P_{OP_O}. When PS occurs, the red dashed curve shows the new P-V output characteristic. As seen, the difference between the new operating power value and the old one can be a good criterion for detecting the PS condition. The main advantage of this method is its simplicity. But this method shows malfunction for three reasons. First, as illustrated in Fig. 2.2-(b), if PS happens slowly, the difference between two consecutive values (difference between P_1 and P_2 and then between P_2 and P_3) is not high enough to be detected as the PS condition. The second reason is exhibited in Fig. 2.2-(c). Supposing the irradiation value decreases significantly but its pattern on the PV panel is uniform, therefore, the difference between two consecutive power values is high and the PS condition is detected. In an MPPT application, this problem does not affect the operation of the system, but in other applications such as power balancing, it causes a malfunction of the system. Finally, the third problem happens when the irradiation value on the PV panel is low and the shading pattern is even. Then the irradiation value becomes high and the PS occurs. In this condition, the PS is not detected. As seen in Fig. 2.2-(d), the operating point is on the P-V curve of the dotted green curve (P_1) before the PS condition which is related to a low irradiation value. Then the PS condition occurs which is shown by the red dashed curve and the generating power value for the new operating point is P_2. As seen, the difference between the power values may be not large enough to be detected as the PS condition.

When the PS condition happens and the PV current is higher than the short-circuit current of a PV module, its diode becomes forward-biased, therefore, measuring this voltage can be a good criterion to detect the PS condition. This method is used in the second category of the PS detection method [87]. Fig. 2.3-(a) shows this method for

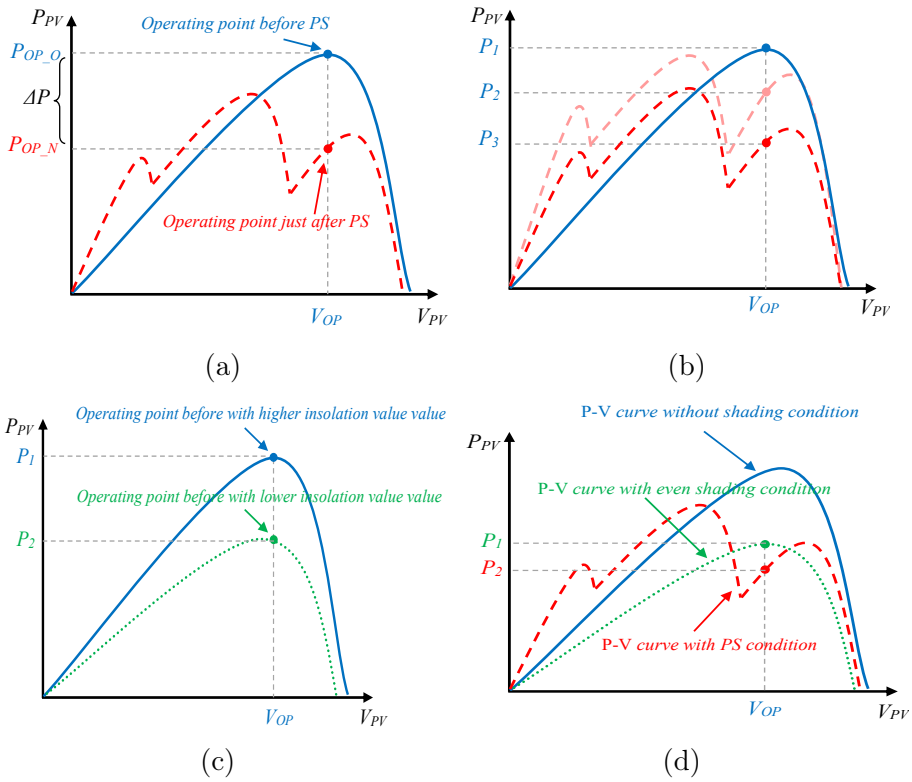

Figure 2.2: The PS detection by comparing two consequence power generated values. (a) The operation. (b) Malfunction case 1. (c) Malfunction case 2. (d) Malfunction case 3.

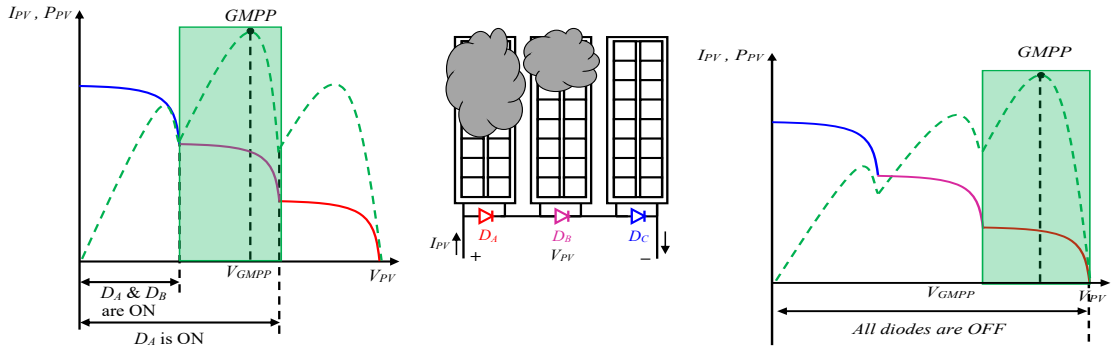

(a) (b)

Figure 2.3: The PS detection by measuring the voltage drop across the anti-parallel diode. (a) The operation. (b) Malfunction case 1.

three PV panels. As seen, the GMPP of the P-V characteristics is in the area where D_A is conducting, therefore, the voltage drop across this diode is a small positive value while D_B and D_C are reverse-biased. The implementation of this method is simple, but its accuracy depends on the operational point of the system. For example, as seen in Fig. 2.3-(b), the GMPP is in the shaded area where all diodes are reverse biased and PS is not detected.

2.5 Review of Valley Switching Based PV Power Optimizer

While the GMPP voltage value is around the open-circuit voltage in non-shading conditions, it can be a very low value, depending on the shading depth in PS conditions. Therefore, the boost power optimizer should be able to operate in a wide input voltage range to track the GMPP [108]-[109]. Decreasing converter losses using resonance is challenging in this condition and demands designing specialized converters. Fig. 2.4 shows a conventional boost power optimizer for a PV system. The output voltage is in series with other power optimizers to produce the DC bus voltage for a solar string inverter. The inverter maintains the output voltage of the power optimizer at a constant value; therefore, the power optimizer controls the input voltage by adjusting the duty cycle to implement the MPPT algorithm. The valley switching method can be employed to increase the power optimizer's efficiency. This method uses the resonance

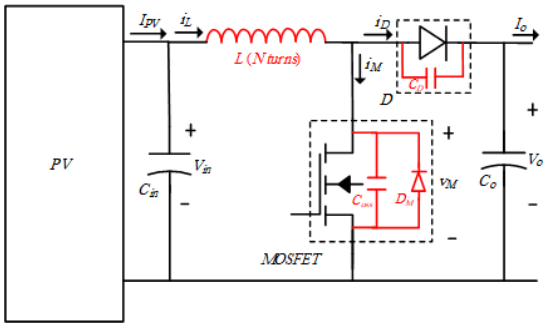

Figure 2.4: The main elements of the boost converter in the valley switching control.

between the converter's inductor (L) and the output parasitic capacitance of the converter's MOSFET (C_{oss}) when the converter's diode turns off [88]-[100]. In the current control mode, the inductor's current rises when the MOSFET turns on till a reference current and it falls once the MOSFET turns off. When the current reaches the reference maximum current, the converter's diode turns on and the inductor's current falls to zero leading to turning off the converter's diode. At this time, a resonance occurs that can be used to decrease the ON-state switching losses. It means that the next switching of the MOSFET is successfully done at the minimum point of this oscillating voltage.

If the input voltage is more than half of the output voltage, the minimum resonance voltage and the switching losses become zero. This situation occurs when the non-shading condition exists and the voltage of GMPP is close to the output voltage value. These losses are important from another perspective because the system usually works in non-shading conditions, therefore, the efficiency of the system decreases significantly. Regarding this fact, using resonance is not helpful to decrease the boost power optimizer losses, consequently, a new topology should be introduced to take advantage of the resonance and increase the efficiency of the converter.

Chapter 3

Comprehensive Solutions for MPPT Algorithms

3.1 Introduction

Two methods are introduced in this chapter as promising comprehensive MPPT algorithms. The first approach is based on an ANN model as the initial point estimator. The PSO technique is used as an application for this model. The concept of a dominant cell is explained and employed for addressing challenging problems such as quantifying PS patterns, limiting the infinite number of patterns, and measuring the depth of shading value electrically. It is shown that the generated model is more accurate than the previous models. The second technique is devising a novel scanning idea to avoid applying a short circuit at the terminal capacitor. In this way, the scanning operation does not have any detrimental effect on the lifetime of the system. Different implementations comprising isolated and non-isolated configurations are described to put the idea into practice. The experimental verifications were done for both methods by designing the required converters and coding the microcontroller. The results prove the correctness of the analyses and support the ideas.

3.2 An ANN-based Comprehensive MPPT Algorithm

In this section, the PSO method is chosen as one of the most sophisticated MPPT algorithm [34]-[41], and the problems of PS conditions are discussed and solved using

an ANN model. First, stability and steady-state analyses of this method are discussed to justify using the proposed method. Then the proposed method is explained in two subsections. The PS pattern reduction is described using the operation of PV cells in shading conditions. finally, a dataset is prepared and an ANN model is used to estimate the GMPP of the PV system. In this way, problems of MPPT algorithms in PS conditions such as getting stuck at an LMPP, long tracking time, fluctuations of power, etc. are solved.

3.2.1 Stability and Steady State Analyses of the PSO MPPT Algorithm

Equation (3.1) shows the relationship between the i^{th} duty cycle in iteration $k+1$ (d_i^k+1) and its value in iteration k (d_i^k) in the PSO MPPT algorithm [34]-[41].

$$\begin{aligned} &d_i^{k+1} = d_i^k + \Delta d_i^{k+1} \quad , \quad i = 1, 2, \ldots, N_d \\ &\Delta d_i^{k+1} = \omega \Delta d_i^k + c_1 r_1 \left(P_{best\_i} - d_i^k\right) + c_2 r_2 \left(G_{best} - d_i^k\right) \end{aligned} \tag{3.1}$$

where P_{best_i}, G_{best}, N_d and ω are the best duty cycle for particle i, the best duty cycle among all duty cycles, the number of particles and the momentum value, respectively. As seen, changes for particle i have three components. The first component keeps the particle in the previous trajectory while the second and the third components tend to change the particle's position towards its best position and the global best position found so far in the community. The coefficients of the second and third components are $c_1 r_1$ and $c_2 r_2$, respectively. While c_1 and c_2 are constant values, r_1 and r_2 are random values between 0 and 1. Similar to other optimization-based algorithms, a lot of duty cycles as particles should be generated and spread all over the search space in the PSO MPPT algorithm to guarantee finding the GMPP. Otherwise, the GMPP may be missed and an LMPP is found. Another solution to avoid getting stuck at an LMPP is decreasing the difference between the new and old duty cycles by selecting small values for ω, c_1, and c_2. Therefore, the PSO MPPT algorithm has the main issues of long tracking time and high fluctuations in the generated power. Also, there is no criterion to determine the sufficient number of particles (duty cycles) to ensure the GMPP tracking. Moreover, it is based on random numbers; therefore, the generated power fluctuations caused by the duty cycle variations during the tracking phase can be significant.

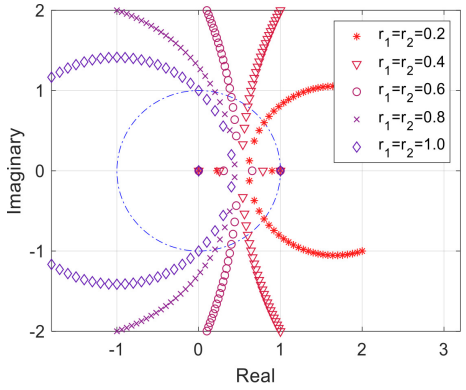

Figure 3.1: Poles of the system by changing c_1, c_2, and ω between 0 and 5 for different values of r_1 and r_2.

The relation between two consecutive iterations can be obtained using some manipulations as follows.

$$d_i^{k+1} = (1 + \omega - c_1 r_1 - c_2 r_2)\, d_i^k - \omega d_i^{k-1} + c_1 r_1 P_{best\_i} + c_2 r_2 G_{best} \tag{3.2}$$

The Z-transform of this equation can be obtained.

$$D_i(Z) = \frac{1}{(Z - (1 + \omega - c_1 r_1 - c_2 r_2) + \omega Z^{-1})} \times \frac{c_1 r_1 P_{best\_i} + c_2 r_2 G_{best}}{1 - Z^{-1}} \tag{3.3}$$

The transfer function is the first part of (3.3) which is a second-order system and (3.4) are its poles. These poles are exhibited in Fig. 3.1 by changing c_1 , c_2 and ω between 0 and 5 for different values of r_1 and r_2. As seen, the magnitude of the poles is greater than 1 for a range of these parameters, therefore, the system is unstable for these values.

$$Z_{1,2} = \frac{1}{2}\left(N \pm \sqrt{N^2 - 4\omega}\right) \;, N = 1 + \omega - (c_1 r_1 + c_2 r_2) \tag{3.4}$$

To ensure that the system remains stable, the magnitude of all poles must be less than 1. The required conditions for a stable response are achieved as follows.

$$\begin{aligned} &\omega \leq 1 \\ &0 \leq c_1 r_1 + c_2 r_2 \leq 2 + 2\omega \end{aligned} \tag{3.5}$$

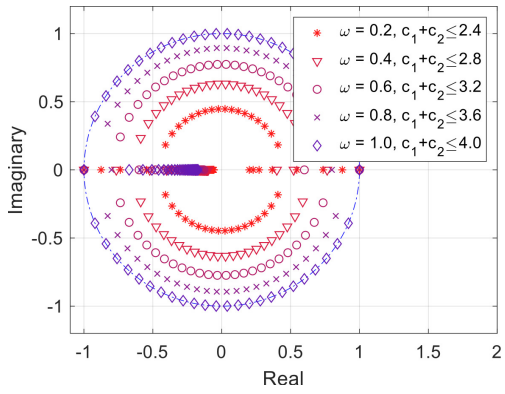

Figure 3.2: Poles of the system by changing c_1, c_2, and ω and satisfying the stability constraints.

r_1 and r_2 are randomly chosen between 0 and 1, and their values must be set to 1 in (3.5) to determine the boundary condition and to guarantee the stability of the algorithm.

$$\begin{aligned} &\omega \leq 1 \\ &0 \leq c_1 + c_2 \leq 2 + 2\omega \end{aligned} \tag{3.6}$$

Fig. 3.2 shows the poles of the system when the constraints of (3.6) are satisfied for r_1 and r_2 equal to 1 and changing the value of ω between 0.2 and 1.0. As seen all poles stay inside the unit circle, therefore the system is stable. Equations (3.4) and (3.6) allow us to verify the stability of the PSO technique. For instance, Fig. 3.3 shows both poles of the system which were calculated using (3.4) for two values of ω and different values of $c_1 + c_2$. As seen, if the value of $c_1 + c_2$ and ω are set to 3.0 and 0.3, respectively, one pole is outside of the unit circle and the PSO becomes unstable. In this case, according to (3.6), the required value of $c_1 + c_2$ must be less than 2.6 to ensure the stability of the algorithm. For this value of $c_1 + c_2$, if ω changes to 0.6, both poles are placed inside the unit circle and the PSO becomes stable.

While equation (3.6) guarantees a stable response of the algorithm, it is not sufficient to ensure that the algorithm converges to the GMPP. Hence, a steady state analysis is necessary to ensure that the GMPP is tracked. The following final value theorem can be used to evaluate the steady state:

$$d_i(\infty) = \lim_{Z \to 1} \left(\left(1 - Z^{-1}\right) D_i(Z) \right) = \frac{c_1 r_1 P_{best\_i} + c_2 r_2 G_{best}}{(c_1 r_1 + c_2 r_2)} \tag{3.7}$$

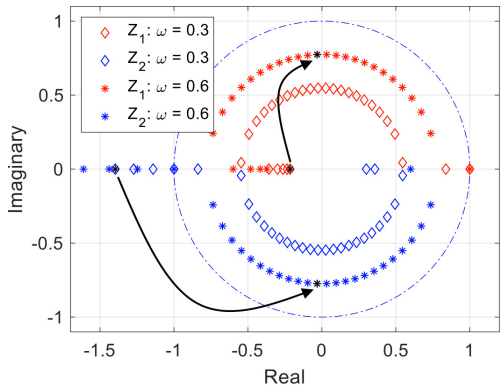

Figure 3.3: Poles of the system for $\omega = 0.3$ and $\omega = 0.6$.

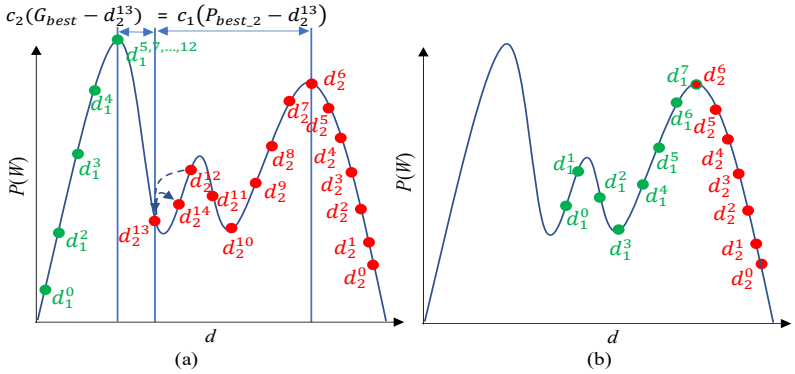

Figure 3.4: PSO steady-state response using two different initial conditions (Green dots: particle number 1 and Red dots: particle number 2).

Equation (3.7) indicates that the steady state response of each particle has two components. One of them is related to the personal best position of the particle i (P_{best_i}) and the other one is associated with the global best position found (G_{best}) in the system. If these two values become equal during evolution, the particle converges toward G_{best}. r_1 and r_2 are random numbers between 0 and 1, therefore, if the weight of the second component ($c_1 r_1 (P_{best\_i} - d_i^k)$) is higher than the third component ($c_2 r_2 (G_{best} - d_i^k)$), $d_i^k + 1$ moves toward P_{best_i} and vice versa. On the other hand, if ($P_{best_i} - d_i^k$) and ($G_{best} - d_i^k$) are evolving in different directions, the convergence time increases. This phenomenon is shown in Fig. 3.4-(a), in which particle number 2 (d_2) came back towards its best-experienced value (d_2^6) instead of going towards the global best position of the system (d_1^5) at iteration 14^{th} (d_2^{14}). In addition, if the G_{best} is not the GMPP, i.e. none of the particles experience it, they converge to an LMPP, as shown in Fig.

3.4-(b). Traditionally two measures can be taken to address this problem. Either the particles can be chosen from the leftmost and rightmost boundaries (duty cycles near 0 and 1) or choosing a lot of particles and spreading them all over the search space. In both classical solutions, values of c_1 and c_2 must be chosen low enough to have a small step in each iteration and to experience the GMPP (G_{best}) during evolution. These solutions increase the tracking time and fluctuations of the generated power. Therefore, it can be concluded that the PSO algorithm still suffers from some deficiencies when it is employed as the MPPT algorithm such as getting stuck at an LMPP, slow convergence time, and considerable fluctuations during finding the GMPP.

The main issues of the PSO algorithm are getting stuck in the LMPP, a high power fluctuation during evolution, and the low speed of convergence. However, these issues cannot be addressed, individually. In other words, improving one of these issues may deteriorate the other issues. For example, to solve the issue of getting stuck in the LMPP, the number of particles should be large and the coefficients should be small to ensure that at least one particle experiences the GMPP. However, these solutions increase the fluctuation in the generated power and decrease the speed of convergence. On the other hand, if the coefficients are chosen as big values to increase the speed of convergence and to decrease the fluctuation, instability issues arise. If the initial particles are spread around the GMPP, as shown in Fig. 3.5, the problem of getting stuck in the LMPP is solved. In addition, fluctuations in the generated power decrease, and the speed of convergence increases. Furthermore, It can be shown that the term related to the particle's own best position can be omitted, therefore, its fluctuation will be eliminated. In addition, the coefficients of the PSO MPPT algorithm can be set to larger values because having small steps to avoid getting stuck at an LMPP is not required. Supposing the PSO algorithm works in a convex area around the GMPP; therefore, the formula of the traditional PSO presented in (3.1) can be changed to (3.8).

$$\begin{aligned} d_i^{k+1} &= d_i^k + \Delta d_i^{k+1} \quad , \quad i = 1, 2, \ldots, N \\ \Delta d_i^{k+1} &= \omega \Delta d_i^k + c_g \left(G_{best} - d_i^k \right) \end{aligned} \tag{3.8}$$

where c_g is a constant value. In comparison to (3.1), the second component related to the best personal experienced particle ($c_1 r_1 (P_{best\_i} - d_i^k)$) is omitted in (3.8) and the coefficient related to the global best particle (c_g) is not adjusted randomly. In fact, when the search space is convex around the GMPP, the ($G_{best} - d_i^k$) term always shows the direction towards the GMPP while the ($c_1 r_1 (P_{best\_i} - d_i^k)$) term may show the other

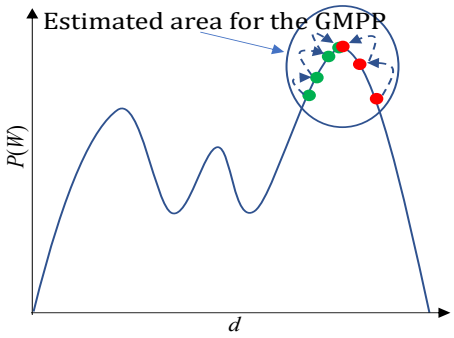

Figure 3.5: The performance of the proposed method around the GMPP (Green dots: particle number 1 and Red dots: particle number 2).

direction. In other words, the $(c_1 r_1(P_{best\_i} - d_i^k))$ term is sometimes in the direction of the best particle and thus increases the speed of convergence and on the other hand, it is sometimes in the opposite direction and slows down the convergence time. Hence, this term has been eliminated and the best duty cycle of the system has been tracked with a constant step. Equation (3.8) can be rewritten to show the relation between two consecutive particles for the proposed PSO algorithm.

$$d_i^{k+1} = (1 + \omega - c_g)\, d_i^k - \omega d_i^{k-1} + c_g G_{best} \tag{3.9}$$

The Z-transform of this equation is shown in (3.10).

$$D_i(Z) = \frac{1}{Z - (1 + \omega - c_g) + \omega Z^{-1}} \frac{c_g G_{best}}{1 - Z^{-1}} \tag{3.10}$$

For the sake of the system stability, the magnitude of poles must be lower than 1 leading to the following criteria.

$$\begin{aligned} &\omega \leq 1 \\ &0 \leq c_g \leq 2 + 2\omega \end{aligned} \tag{3.11}$$

Equation (3.12) shows the steady state response of the system that is G_{best}.

$$d_i(\infty) = \lim_{Z \to 1} \left(\left(1 - Z^{-1}\right) D_i(Z) \right) = G_{best} \tag{3.12}$$

As seen in (3.12), the steady-state analysis shows that all particles converge in G_{best} if there exists one MPP in the searching space. Therefore, based on this steady-state

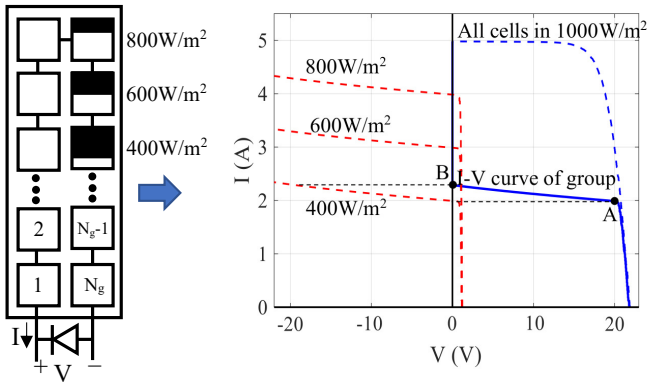

Figure 3.6: Partial shading effects on the I-V curve of PV panel.

analysis, the proposed MPPT algorithm can find the GMPP accurately if the convex zone around it is properly determined.

3.2.2 PS Pattern Reduction

There are an infinite number of PS patterns for a PV panel depending on atmospheric parameters such as temperature and solar irradiation. Each PS pattern features a unique I-V curve and consequently a GMPP. For each PS pattern, there are upper and lower boundaries around the MPP. Fig. 3.6 shows a group of PV cells in which three cells are in different shading conditions, i.e. 400 $\frac{W}{m^2}$, 600 $\frac{W}{m^2}$ and 800 $\frac{W}{m^2}$. Also, the irradiation for the remaining cells is 1000 $\frac{W}{m^2}$. As seen, the I-V curve bends at point A because the cell with the lowest irradiation (400 $\frac{W}{m^2}$) limits the current. Also, the diode turns on at point B and clamps the voltage on the zero level. Therefore, the I-V curve of the group is affected dominantly by the cell with the lower irradiation and the other cells have a low effect on this curve. In other words, the I-V curve of the cell with the lowest irradiation (the most shading area) can represent the equivalent I-V curve of the group. This curve gives the U-B of the voltage at the GMPP of the group. On the other hand, if there is more than one cell with the same lowest irradiation, the I-V curve changes. The maximum change occurs when all cells of that group have the same irradiation equal to the lowest one (uniform shading condition). This curve is the L-B of the I-V curve of the group. Hence, as highlighted in Fig. 3.7, a general strategy can be used to determine the U-B and L-B as follows: under PS conditions, we consider the I-V curve of the cell with the lowest irradiation (red dashed circle in Fig. 3.7) as a U-B and the L-B is the equivalent I-V curve of the group taking into account that all cells have the same lowest

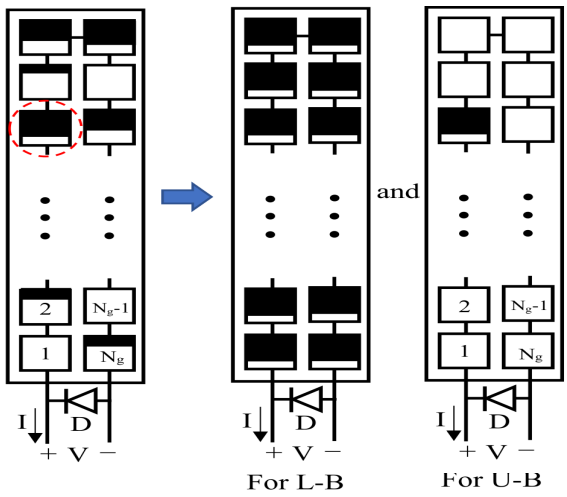

Figure 3.7: Shading patterns for the upper and lower boundaries.

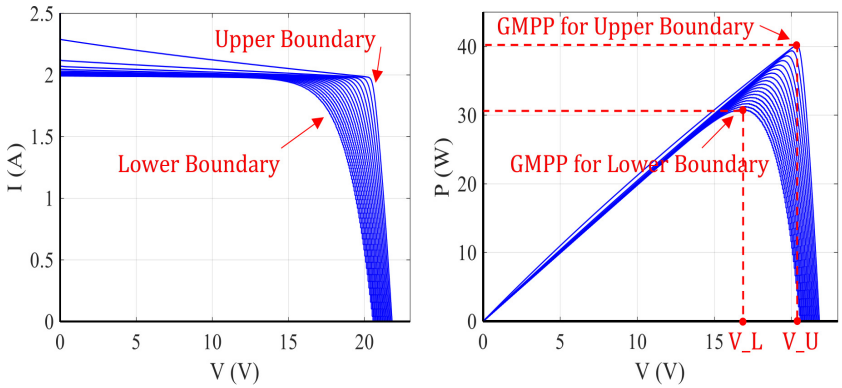

Figure 3.8: The I-V and P-V curves for the upper and lower boundaries.

irradiation level. Fig. 3.8 shows these boundaries for the ET-M53695 PV panel when the temperature, irradiation value, and the lowest irradiation are 25 ^oC, 1000 $\frac{W}{m^2}$ and 400 $\frac{W}{m^2}$, respectively. The curves between these boundaries are achieved by increasing the number of cells with the lowest but the same irradiation. The voltage at the GMPP for the L-B can be calculated analytically using a closed-form formula while this value for the U-B can be calculated numerically. An ANN model is used to implicitly capture the voltage for the U-B as a function of temperature, irradiation, and irradiation value of the cell with the lowest irradiation level.

The I-V curve of a PV cell in a shading condition can be achieved using the single-diode model as follows [114].

$$I_C = K_{sh} I_{ph} - I_o \left(e^{\frac{q\,(V_C + R_S I_C)}{a K_t T}} - 1 \right) - \frac{(V_C + R_S I_C)}{R_P} \times \left(1 + K_d \left(1 - \frac{(V_C + R_S I_C)}{V_{br}} \right)^{-n_d} \right) \tag{3.13}$$

where I_{ph}, I_o, R_S, R_P, a, q, K_t, T, K_{sh}, K_d, n_d and V_{br} are photo-generated current, inverse saturation current, series, and parallel resistance, diode ideality factor, electron charge, Boltzmann constant, the temperature in Kelvin, shading depth, the fraction of current involved in avalanche breakdown, avalanche breakdown exponent and breakdown voltage, respectively. To obtain the L-B of the GMPP as shown in Fig. 3.7, all cells should receive equal irradiation. Thus, when all cells experience the same shading condition, the part related to the inverse bias of (3.13) can be omitted and the voltage of a group with N_g cells versus its current can be achieved using (3.14).

$$I = I_{ph} - I_o \left(e^{\frac{q\,(V + R_{SG} I)}{a N_g K_t T}} - 1 \right) - \frac{(V + R_{SG} I)}{R_{PG}} \qquad R_{SG} = N_g R_S \;\;,\;\; R_{PG} = N_g R_P \tag{3.14}$$

The parameters of (3.14) can be calculated using the datasheet in the STC. R_S and R_P have a low effect on the I-V curve; therefore, they can be regarded as constant values. To apply the effect of temperature, irradiation, and shading depth (K_{sh}) rather than STC, the following equation can be used [113]-[121].

$$I_{ph} = I_{ph\_STC} \left(1 + C_{TI} \left(T - T_{STC} \right) \right) K_{sh} \qquad K_{sh} = \frac{G}{G_{STC}} \tag{3.15}$$

$$I_o = I_{o\_STC} \left(\frac{T}{T_{STC}} \right)^3 e^{\left(\frac{E_g}{K_t} \left(\frac{1}{T_{STC}} - \frac{1}{T} \right) \right)} \tag{3.16}$$

$$V_{oc\_T} = V_{oc\_STC} \left(1 + C_{TV} \left(T - T_{STC} \right) \right) \tag{3.17}$$

$$V_{oc} = f_{V_{oc\_ir}}\left(V_{oc\_T}\right) \tag{3.18}$$

$$a_{STC} = \left(\frac{V_{oc}}{V_{oc\_STC}} \frac{T_{STC}}{T} \frac{Ln\left(\frac{I_{ph\_STC}}{I_{o\_STC}} + 1\right)}{Ln\left(\frac{I_{ph}}{I_o} + 1\right)} \right) a \tag{3.19}$$

where C_{TI}, G, E_g, V_{oc}, f_{Voc_ir} and C_{TV} are temperature-dependent coefficient for photo generated current, irradiation value, material band gap (1.121 eV), open circuit voltage and its function related to the irradiation, and temperature-dependent coefficient of the open circuit voltage, respectively. The open-circuit voltage (V_{oc}) of a group can be obtained by setting the current to zero in (3.14).

$$0 = I_{ph} - I_o \left(e^{\frac{qV_{oc}}{aN_gK_tT}} - 1 \right) - \frac{V_{oc}}{R_{PG}} \tag{3.20}$$

The following equations show some assumptions that are correct for real PV panels.

$$\begin{aligned} &I_o \ll 1 \\ &\frac{R_S}{R_P} \ll 1 \\ &V - R_S\frac{P}{V} \simeq V \\ &V + R_S\frac{P}{V} \simeq V \\ &\frac{V}{R_P} \ll 1 \end{aligned} \tag{3.21}$$

where P is the generated power. The following result can be achieved using (3.20) and taking into account assumptions presented in (3.21).

$$I_{ph} \simeq I_o e^{\frac{qV_{oc}}{aN_gK_tT}} = I_o e^{MV_{oc}} \quad , \quad M = \frac{q}{aN_gK_tT} \tag{3.22}$$

The P-V equation can be obtained by multiplying V to both sides of (3.14) and applying $I = \frac{P}{V}$.

$$P = VI_{ph} - VI_o \left(e^{M\left(V + R_{SG}\frac{P}{V}\right)} - 1 \right) - \frac{(V^2 + R_{SG}P)}{R_{PG}} \tag{3.23}$$

The voltage value at the GMPP can be achieved by setting the derivative of P with respect to V to the zero value.

$$\frac{\partial P}{\partial V} = 0 = I_{ph} - I_o \left(e^{M\left(V+R_{SG}\frac{P}{V}\right)} - 1 \right) - \\ -I_o M \left(V - R_{SG}\frac{P}{V}\right) \left(e^{M\left(V+R_{SG}\frac{P}{V}\right)} \right) - \frac{2V}{R_{PG}} \tag{3.24}$$

Applying (3.21) to (3.24) yields:

$$0 = I_{ph} - I_o e^{MV} (1 + MV) \tag{3.25}$$

I_{ph} can be replaced by (3.22), then (3.26) can be obtained by some manipulations.

$$e^{M(V_{oc}-V)} = (1 + MV) \tag{3.26}$$

To solve this equation, the exponential component can be replaced by its Taylor series around open-circuit voltage (V_{oc}).

$$e^{M(V_{oc}-V)} \simeq 1 - M (V - V_{oc}) + \frac{1}{2} M^2 (V - V_{oc})^2 \tag{3.27}$$

Therefore, the voltage at the GMPP can be obtained by replacing (3.27) into (3.26) and solving it.

$$V = V_{GMPP} = \left(\sqrt{V_{oc} + \frac{2}{M}} - \sqrt{\frac{1}{2M}} \right)^2 - \frac{1}{2M} \tag{3.28}$$

For example, this value for the ET-M53680 PV panel ($a_{STC} = 1.398$ and $N_g = 18$) is $17.69\,V$ in the STC condition that is close to the voltage value ($17.64\,V$) available in the datasheet. This proves the accuracy of the formula to calculate the voltage value at the GMPP in the even irradiation. The upper boundary of the voltage at the GMPP can be calculated when only one cell with the lowest irradiation is in the shading condition as highlighted in Fig. 3.7. For a group with N_g cells, (3.29) shows the required equation

that must be solved for the voltage and current in each condition.

$$V_{series} = (N_g - 1)\, V_{normal} + V_{shaded}$$
$$V = \begin{cases} V_{series} & , \quad V_{series} > 0 \\ 0 & , \quad V_{series} \leq 0 \end{cases} \tag{3.29}$$

where V_{shaded} and V_{normal} are the voltage of cells in the shading ($K_{sh} < 1$) and non-shading condition ($K_{sh} = 1$), respectively, which are calculated using (3.13). This equation cannot be solved analytically because it is highly nonlinear. Instead, a dataset can be prepared by solving it numerically under different irradiation, temperature, and shading depths (K_{sh1} and K_{sh2} for this PV panel with two PV groups) of the cell as inputs and the upper boundary of the voltage at the GMPP as an output. These boundaries for one PV group of the ET-M53680 PV panel are shown in Fig. 3.9 by changing the irradiation value, temperature, and shading depth. Also, these boundaries for this PV panel are shown in Fig. 3.9-(d) which is comprised of two PV groups.

3.2.3 The ANN Method and Solving the Problems

A dataset is prepared for ET-M53695 PV panel by changing the temperature, insolation value, and shading rate for its two modules and calculating the voltage at GMPP. In fact, the voltage at GMPP is a function of four variables. It is a regression problem and an ANN model with 4 neurons in the input layer and one neuron in the output layer was used for this application. The ANN model is shown in Fig. 3.10. Two hidden layers with 5 neurons in each layer are used which has the best performance. Also, implementing this ANN in the microcontroller is simple because it requires one 4×5 matrix between the input and the first input layer, one 5×5 matrix between two hidden layers, and one 5×1 vector at the output layer. The bias vectors are two 5×1 vectors and the *tansig* transfer function was chosen. To increase the speed of calculation and optimize the codes, a look-up table is used instead of using the *math* library.

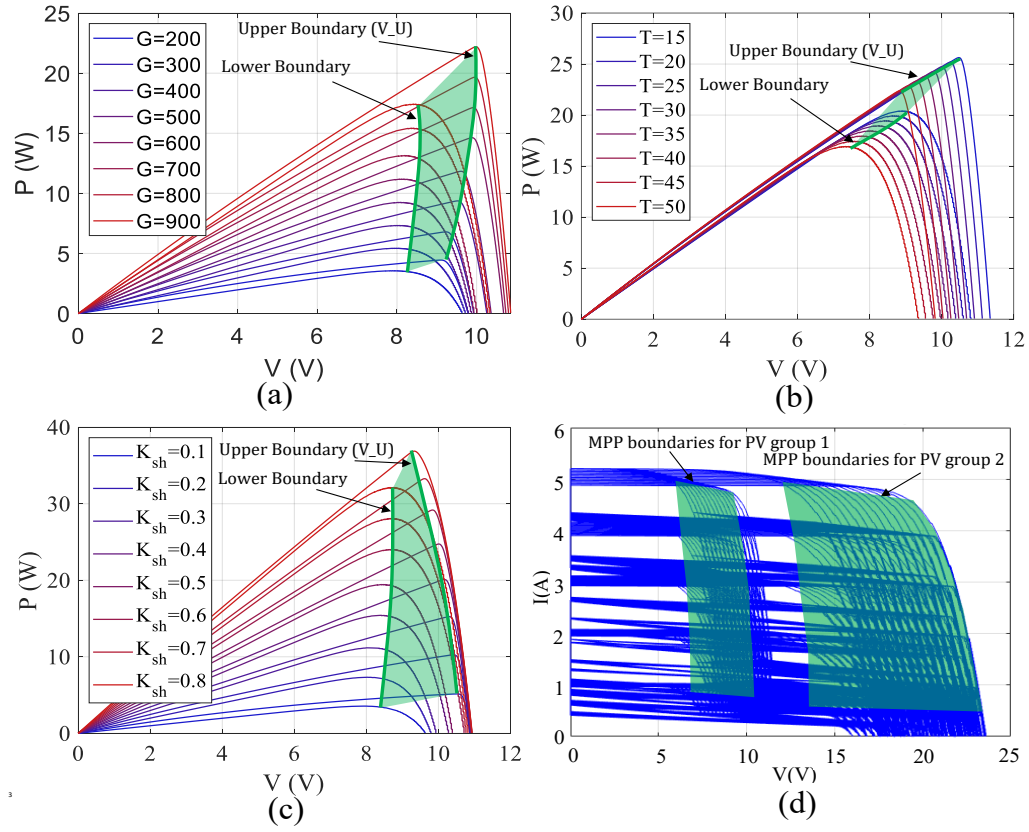

Figure 3.9: The GMPP boundaries for a PV group of the ET-M53680 PV panel for (a) different irradiation values, (b) different temperatures, (c) different shading depths and (d) for this PV panel (two PV groups).

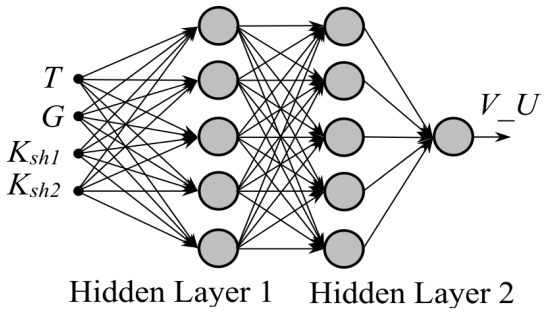

Figure 3.10: The ANN for estimating GMPP.

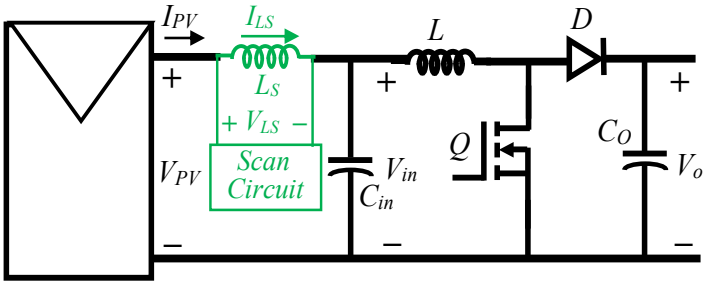

Figure 3.11: The proposed circuit for scanning the I-V curve.

3.3 Converter Based Scanning the Output Characteristics of PV Panels

Fig. 3.11 shows the basic notion behind the proposed circuit to fulfill the aims of a sophisticated scanning circuit. As seen, an inductor is placed between the PV panel and the terminal capacitor. This inductor can be in the form of a pair of mutual and isolated inductors or a usual one. The *Scan Circuit* is a power electronic converter that applies a positive or negative voltage across the inductor L_S. The voltage value of the PV panel, terminal capacitor, and inductor have the following relation.

$$V_{PV} = V_{in} + V_{LS} \tag{3.30}$$

In addition, when the *Scan Circuit* is off, the inductor and the PV panel are in series, therefore, their currents are equal.

$$I_{PV} = I_{LS} \tag{3.31}$$

It is well-known that the output capacitance of the PV panels is negligible [122], therefore, it can be ignored. It means that if a voltage is applied across the inductor L_S in a short time, the output voltage of the PV panel changes while V_{in} can be assumed constant because C_{in} is a large capacitor in comparison to the output capacitance of the PV panel. Fig. 3.12 exhibits the operation of the circuit. The scanning procedure can be divided into two steps namely the LHS step and the RHS one. First, the *Scan Circuit* is off and the current of the PV panel is equal to the current of L_S (point OP).

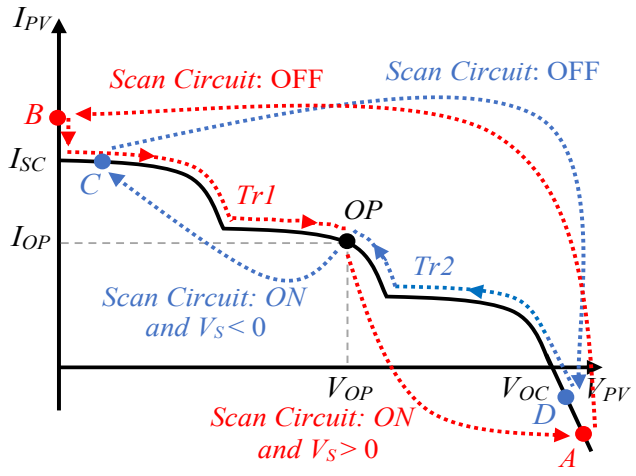

Figure 3.12: The scanning trajectories for the proposed circuit.

3.3.1 LHS Step

In this step, the left-hand side of point OP on the I-V curve is scanned. The *Scan Circuit* applies a positive voltage across the inductor L_S, therefore, the voltage of the PV panel increases according to (3.30) and jumps to point A. Also, the current of the inductor L_S increases during this time and reaches to a maximum predefined value (I_{max}) because a positive voltage is applied across it. Then, the *Scan Circuit* turns off, consequently, the current of the PV panel becomes again equal to the current of the inductor L_S (point B). The PV panel voltage value is lower than V_{in} at this point, as a result, V_{LS} becomes negative and the current of the inductor L_S starts to decrease and tracks the I-V curve of the PV panel (T_{r1}) and reaches the point OP.

3.3.2 RHS Step

In this step, the right-hand side of point OP on the I-V curve is scanned. The *Scan Circuit* applies a negative voltage across the inductor L_S and the voltage of the PV panel jumps to a lower voltage (point C). On the other hand, because of the negative voltage, the current of the inductor L_S decreases to a minimum predefined current (I_{min}). At this moment, the *Scan Circuit* turns off, therefore, the current of the PV panel becomes equal to the current of the inductor L_S (point D). The voltage across the inductor L_S is positive at this point because the voltage of the PV panel is greater than V_{in}, consequently, the current of the inductor starts to increase and scans

the trajectory T_{r2}. When this current reaches to the point OP, the voltage of the PV panel is equal to V_{in}, consequently, the current of the inductor remains at the point OP.

3.3.3 The Implementation of the Proposed Idea

The *Scan Circuit* should have the ability to apply a positive and negative voltage to the inductor L_S in a short period of the time. Several DC/DC switching power supply topologies can be used as the *Scan Circuit* by eliminating their output capacitor and rectifiers. There are two main categories for converters namely isolated and non-isolated ones. The flyback converter as an isolated *Scan Circuit* that is the simplest and most economical type in this category is selected in this work. Also, the full bridge non-isolated scan circuit is described because capacitors are not used in this configuration, resulting in an increase in its reliability. No matter which type of converter is used in each category, the operation of the *Scan Circuit* is the same; therefore, the generality of the analyses is kept.

3.3.3.1 The Implementation Using the Isolated Transformer

Fig. 3.13 shows the required converter which is comprised of two flyback converters to generate the positive and negative voltages. RHS converter is used to apply the negative voltage and right-hand side scanning step. On the other hand, LHS one is used to apply the positive voltage and to scan the left-hand side of the operating point. As shown in Fig. 3.12, the voltage of the PV panel jumps to point A when the switch Q_1 turns on, as a result, a current flows from C_{in} towards the PV panel which decreases its voltage. Diode D_S is used to avoid this problem. This diode sets the point A to the open-circuit voltage of the curve. Also, when the switch Q_2 turns off to scan the I-V curve, the scanning procedure begins from point D and the PV panel draws current from C_{in} again which decreases its voltage. Diode D_P can be used to avoid this problem by preparing a path for the inductor current.

These converters can be combined and built into a converter similar to a push-pull one as shown in Fig. 3.14. However, contrary to the push-pull converter, the secondary winding current of this converter flows when the MOSFETs are turned off. In fact, it is a combination of two flyback converters. Fig. 3.15 exhibits the operation of this circuit in LHS mode. When Q_1 turns on, the PV voltage jumps to V_A and its current becomes zero. As long as the switch Q_1 is ON, the magnetizing current (I_m) increases from I_{OP}

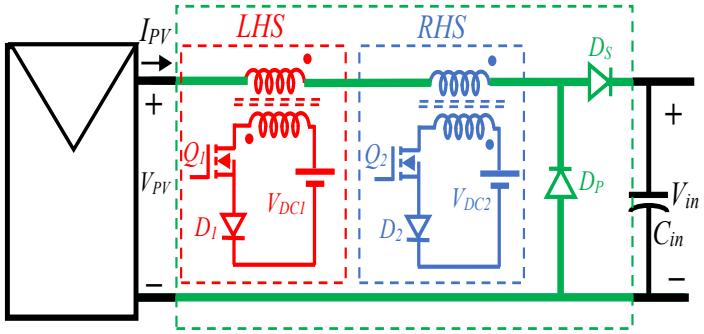

Figure 3.13: The implementation of the proposed technique using two flyback converters.

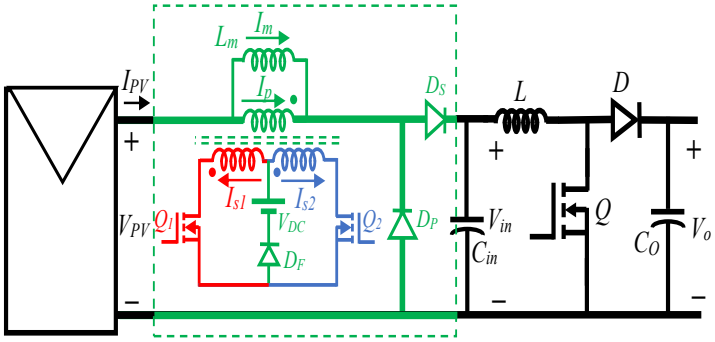

Figure 3.14: The implementation of the proposed technique.

and reaches I_B. At this moment, Q_1 turns off and the voltage across the magnetizing inductance becomes negative, consequently, its current begins to decrease. The inductor L_m and the PV panel are in series during this time, therefore, the I-V curve is scanned in this period. Finally, the voltage of the PV panel reaches the voltage of C_{in} and the current of L_m remains at I_{OP}. Fig. 3.16 exhibits the operation of the scanning circuit in RHS mode. When Q_2 turns on, the voltage of PV panel jumps to V_C. Also, I_m decreases and when it reaches I_D, the switch Q_2 turns off at this point. Therefore, I_m which is equal to I_{PV} starts to increase because the voltage of the PV panel (V_{PV}) is greater than V_{in}. The RHS begins at this point until the current of the PV panel reaches to I_{OP}.

3.3.3.2 Implementation Using an Inductor

A full bridge converter can be used to apply the positive and negative voltage across the inductor L_S. Fig. 3.17 shows this topology. Switches Q_1 and Q_3 act simultaneously

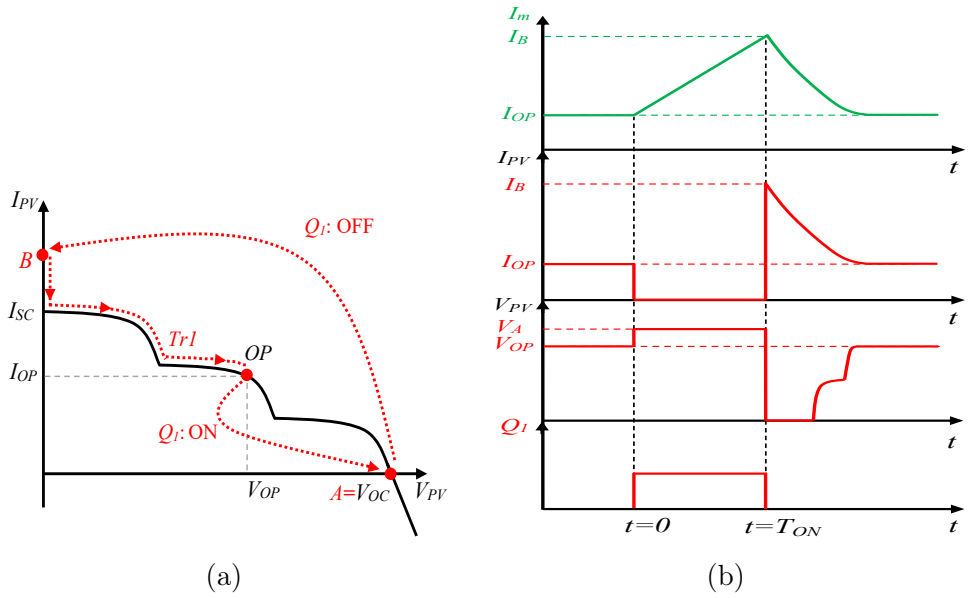

(a) (b)

Figure 3.15: The trajectory and waveforms when Q_1 acts. (a) The trajectory. (b) The waveforms.

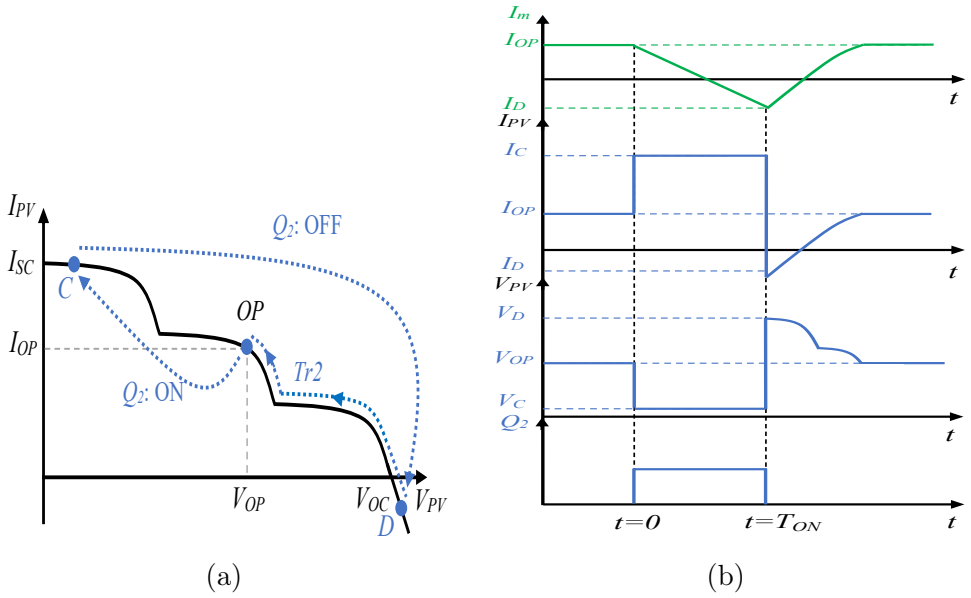

(a) (b)

Figure 3.16: The trajectory and waveforms when Q_2 acts. (a) The trajectory. (b) The waveforms.

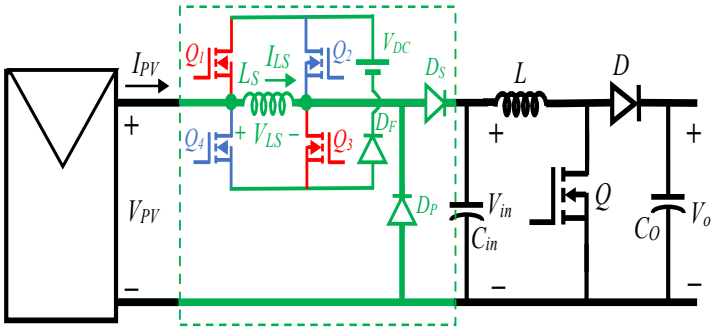

Figure 3.17: The implementation of the proposed technique using a non-isolated converter.

to do the LHS scanning phase and switches Q_2 and Q_4 operate together to implement the RHS scanning one. Fig. 3.18 shows the operation of the circuit in LHS and RHS modes. As seen, when switches Q_1 and Q_3 turn on, the current and voltage of the PV panel jump to point A (the open-circuit voltage point). As long as these switches are ON, the current of inductor L_S increases and reaches to the point B. The LHS scanning begins by turning off the aforementioned switches. In this condition, the voltage across inductor L_S is negative and its current which is equal to the current of the PV panel decreases. When the current of the inductor L_S becomes equal to I_{OP}, the voltage across this inductor becomes zero and the current of the inductor L_S and the PV panel remains at this point. On the other hand, when the switches Q_2 and Q_4 turn on, the voltage of the PV panel jumps to point C. The RHS phase starts by turning these switches off and jumping the PV panel current to point D. The voltage across the inductor L_S is positive at this point, therefore, the current of this inductor which is equal to that of the PV panel increases and reaches the point OP.

3.3.4 The Effect of the Non-Ideal Inductor or Transformer

Among non-ideal elements in Fig. 3.14, the inductor or transformer has significant effects on the operation of the circuit since they carry the current in both scanning phases and all switching states. Therefore, the effect of non-ideality in this element is regarded. When the transformer or inductor is non-ideal, the operation of the system is a bit different. Here, the wire resistance effect and leakage inductance for non-ideal transformer is explained, however, the same condition occurs for the non-ideal inductor. Fig. 3.19-(a) exhibits the primary current and the secondary voltage of the transformer

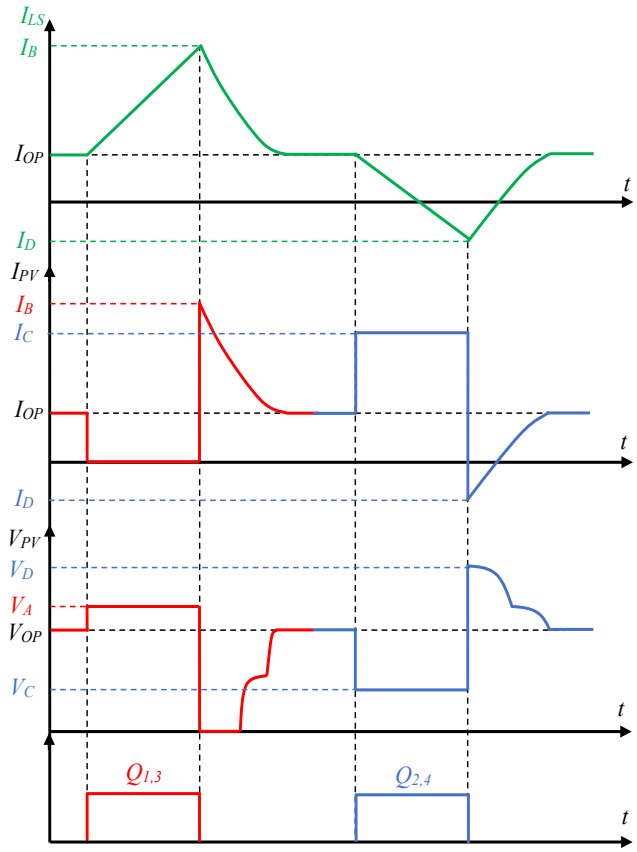

Figure 3.18: The waveforms for full bridge non-isolated scan converter.

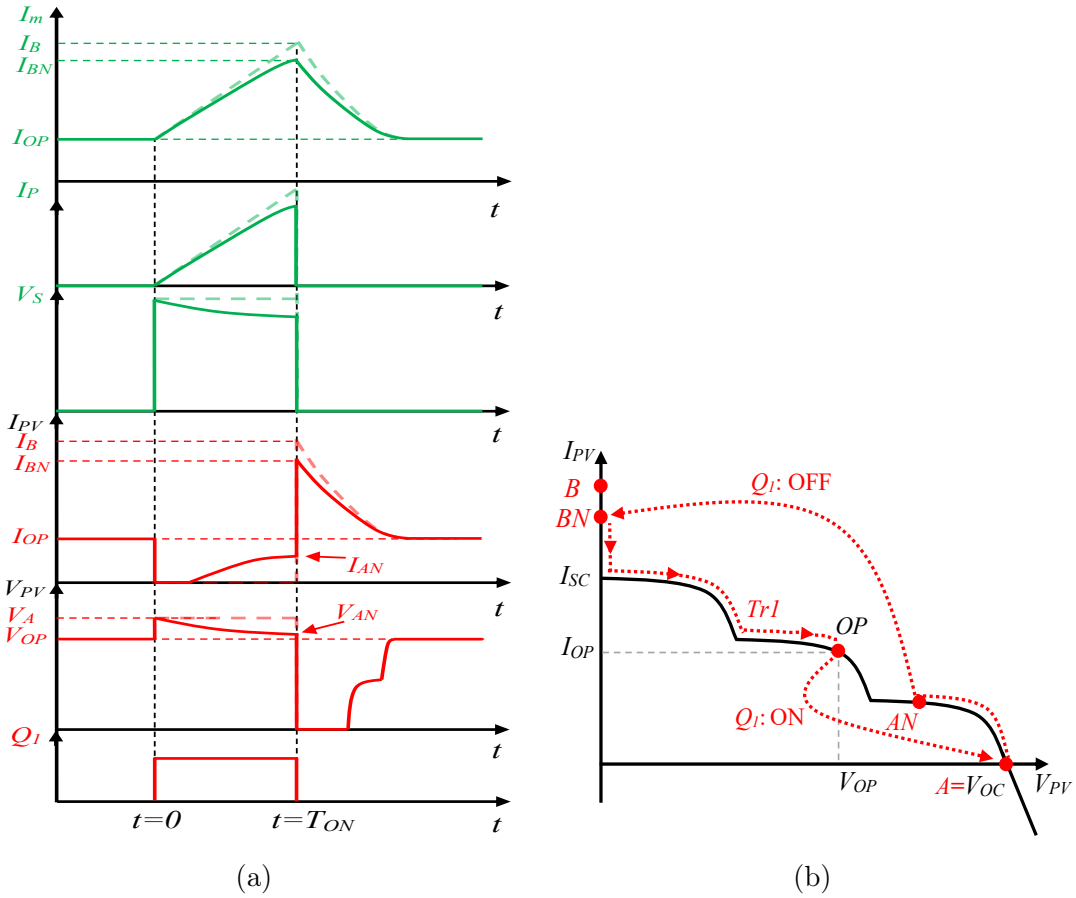

Figure 3.19: The trajectory and waveforms when Q_2 acts for non-ideal inductor. (a) The trajectory. (b) The waveforms.

when Q_1 turns on in Fig. 3.14. As seen, the primary current (I_P) increases; therefore, the voltage drops across the resistance of the wires and the leakage inductances go up. Consequently, the primary voltage and the secondary voltage are not constant and start to decrease. When Q_1 turns off, the waveforms are almost the same as an ideal condition, because the magnetizing current acts as a current source, and the resistances and leakage inductances do not have significant effects on the operation of the scanning procedure. Fig. 3.19-(b) shows the trajectory in this condition for the LHS mode. As seen, contrary to the ideal condition, point A moves towards the operating voltage (point AN) and does not remain at point A. The same condition occurs when switch Q_2 turns on for the RHS mode.

3.3.5 Designing the Required Converter

During LHS phase, a positive voltage is applied to the inductor L_m, and its current (i_m) can be calculated based on (3.32) in this period (T_{Neg}).

$$\begin{aligned} L_m \frac{di_m(t)}{dt} &= V_{DC} \\ i_m(t) &= I_{OP} + \frac{V_{DC}}{L_m} t \end{aligned} \tag{3.32}$$

i_m increases and reaches I_B at the end of this period. Then *Scan Circuit* turns off to scan the left-hand side of the operating point and (3.33) shows this current.

$$\begin{aligned} L_m \frac{di_m(t)}{dt} &= V_{PV} - V_{in} \\ i_m(t) &= I_B + \frac{(V_{PV} - V_{in})}{L_m} t \end{aligned} \tag{3.33}$$

$$(V_{PV} - V_{in})$$

is negative during LHS phase, therefore, i_m decreases and finally reaches I_{OP}. On the other hand, (3.34) and (3.35) show the current of the inductor L_m in the RHS mode when the *Scan Circuit* turns on and turns off, respectively.

$$\begin{aligned} L_m \frac{di_m(t)}{dt} &= -V_{DC} \\ i_m(t) &= I_{OP} - \frac{V_{DC}}{L_m} t \end{aligned} \tag{3.34}$$

$$\begin{aligned} L_m \frac{di_m(t)}{dt} &= V_{PV} - V_{in} \\ i_m(t) &= I_D + \frac{(V_{PV} - V_{in})}{L_m} t \end{aligned} \tag{3.35}$$

Contrary to (3.33), $(V_{PV} - V_{in})$ in (3.35) is positive during RHS phase, therefore, i_m increases and at last hits I_{OP} again. V_{in} decreases when the *Scan Circuit* turns on (point A for LHS and point C for RHS) and reaches its minimum value. Because the generated power of the PV panel is almost zero at these points and the load power is supplied by C_{in}. As soon as the *Scan Circuit* turns off, V_{in} recovers and at the end of the scanning period reaches to V_{OP} again. Therefore, the maximum values of the MOSFET ON-time (T_{Neg} for LHS and T_{Pos} for LHS) are determined by the maximum voltage drops of V_{in} ($\Delta V_{in\_\max}$). I_{OP} is supplied to the load by the PV panel before

the scanning procedure but when it begins, both C_{in} and the PV panel must supply the load. Consequently, the voltage of V_{in} decreases. Supposing C_{in} supplies k percent of the load current, therefore, its voltage and maximum voltage drops can be calculated through (3.36) and (3.37).

$$\begin{aligned} C_{in}\frac{dv_{in}(t)}{dt} &= -kI_{OP} \\ v_{in}(t) &= V_{OP} - \frac{kI_{OP}}{C_{in}}t \end{aligned} \tag{3.36}$$

$$\begin{aligned} \Delta V_{in\_\max} &= V_{OP} - V_{in\_\min} \\ V_{in\_\min} &= V_{OP} - \frac{kI_{OP}}{C_{in}}T_{ON\_\max} \end{aligned} \tag{3.37}$$

T_{ON_max} is the maximum allowable time where the *Scan Circuit* can be turned on and can be calculated as follows.

$$T_{ON\_\max} = C_{in}\frac{V_{OP} - V_{in\_\min}}{kI_{OP}} \tag{3.38}$$

k is a low value because the PV panel generates power during the scanning procedure. As explained above T_{ON_max} is the maximum value of T_{Neg} and T_{Pos}.

$$\begin{aligned} \max\left(T_{Neg}\right) &\leq T_{ON\_\max} \\ \max\left(T_{Pos}\right) &\leq T_{ON\_\max} \end{aligned} \tag{3.39}$$

To calculate the maximum value of L_m, assume T_{Neg} and T_{Pos} are equal to T_{ON_max}.

$$\begin{aligned} T_{Neg} &= T_{ON\_\max} \\ T_{Pos} &= T_{ON\_\max} \end{aligned} \tag{3.40}$$

On the other hand, when the *Scan Circuit* turns off, the current of the inductor L_m must be greater than the short-circuits current in the LHS mode ($I_B \geq I_{SC}$) and less than zero in the RHS mode ($I_D \leq 0$). I_B and I_D can be calculated using (3.32), (3.34) and (3.40). Therefore, (3.41) and (3.42) show the upper limit of the inductance in LHS and RHS phases, respectively.

$$L_m \leq \frac{V_{DC}}{(I_{SC} - I_{OP})}T_{ON\_\max} \tag{3.41}$$

$$L_m \leq \frac{V_{DC}}{I_{OP}}T_{ON\_\max} \tag{3.42}$$

L_m and V_{DC} can be determined by (3.41) and (3.42) and using the boundaries of the current and the voltage of the PV panel which are shown in (3.43).

$$\begin{aligned} I_{PV\_\min} \leq I_{OP} \leq I_{PV\_\max} \\ V_{PV\_\min} \leq V_{OP} \leq V_{PV\_\max} \end{aligned} \tag{3.43}$$

where I_{PV_min}, I_{PV_max}, V_{PV_min} and V_{PV_max} are the minimum and maximum values of the operation currents and voltages of the PV panel, respectively. The minimum value of L_m depends on the output capacitance of the PV panel. If it is chosen inappropriately small, the resonance frequency related to L_m and the output capacitance of the PV panel increases, leading to current oscillations. The minimum value of L_m is by far less than its maximum value knowing the fact that the output capacitance of the PV panel is negligible. Consequently, if the value of L_m is close to its maximum value, undesirable oscillations can be avoided.

3.4 Experimental Verification

In this chapter, the experimental results are divided into two subsections. The first part is dedicated to the proposed MPPT solution based on the ANN model and the second subsection is allocated to the scanning converter.

3.4.1 A Comprehensive ANN-based Approach to Solve Problems of MPPT Algorithms

The experimental setup shown in Fig. 3.20 mainly consists of a boost converter as a power optimizer, the TerraSAS PV simulator to produce the arbitrary I-V curve for the ET-M53695 PV panel in the PS condition, a battery and a resistive load. The MPPT algorithms are implemented in the TMS320F28335 DSP microcontroller. In addition, the output current and voltage of the PV simulator is connected to corresponding sensors which prepare the isolated measurements for the analog to digital peripheral of the microcontroller. Other parameters of the setup are presented in Table 3.1.

To examine the performance of the proposed technique to estimate the voltage boundaries, different shading conditions were created manually on the ET-M53695 PV panel as shown in Fig. 3.21. Fig. 3.22 shows the I-V and P-V curves for L-B and U-B boundaries measured by the I-V 400W Photovoltaic Panel Analyzer. The U-B boundary is

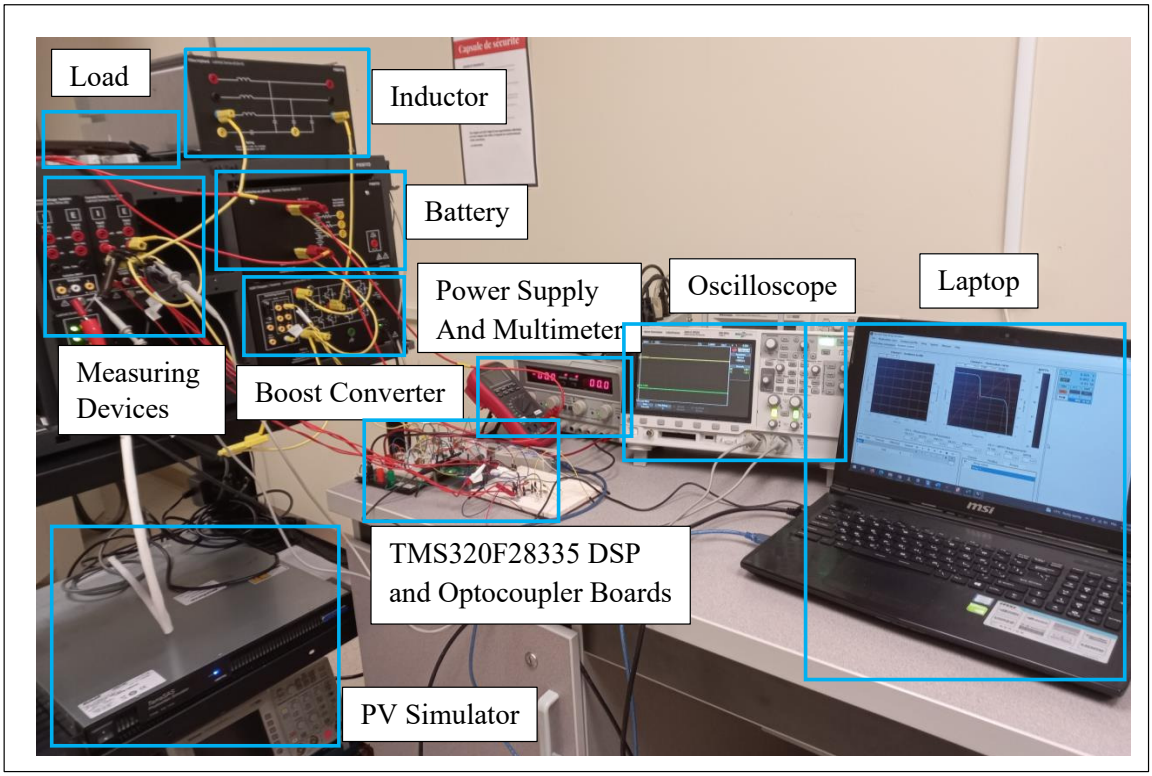

Figure 3.20: The experimental setup for the ANN-based MPPT algorithm verification.

Table 3.1: Parameters of the system for the ANN-based MPPT algorithm verification.

Parameter	Description	Value
V_o	Output voltage	$50\,V$
f_{sw}	Switching frequency	$20\,kHz$
C_{in}	Input capacitor	$220\,\mu F$
C_o	Output capacitor	$220\,\mu F$
L	Converter inductor	$1\,mH$

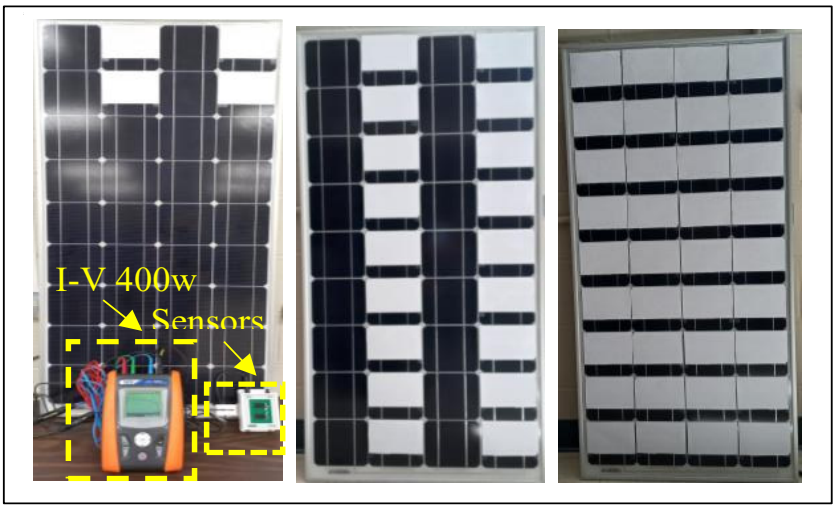

Figure 3.21: The ET-M53695 PV panel in PSC connected to I-V 400W Photovoltaic Panel Analyzer.

determined by the cell with the highest shading condition and the L-B boundary is determined by the even shading condition. The photo-generated current that is almost equal to the short circuit current can be used to calculate the depth of shading for the cell with the highest shading condition.

When the I-V curve starts to bend, the current is around 1.4 A and the short circuit current in STC (1000 $\frac{W}{m^2}$ and 25 ^oC) for this panel is 5 A. Also, C_{TI} for this panel is 0.042 $\%/\,^oC$ and the temperature in this test was 55 ^oC, therefore, the depth of shading for the dominant cell (K_{sh}) is 28 %. C_{TV} for this panel is -0.336 $\%/\,^oC$ and the nonlinear curve of open circuit voltage versus temperature is available in the datasheet. Thus, the calculated open-circuit voltage as per (3.17) and (3.18), is 20.23 V. The diode ideality factor and M for this condition are 1.235 and 1.59 according to (3.19) and (3.22), respectively. Consequently, the lower boundary of the voltage at the GMPP is 16.60 V based on (3.28). This value is 16.72 V according to the measurement which shows the accuracy of (3.28) to calculate the lower boundary of the voltage value at the GMPP. The upper boundary of the voltage at the GMPP is achieved by the neural network which is equal to 18.28 V that is in good accordance with the measured value from Fig. 3.22 i.e. 18.39 V.

To evaluate the capability of the proposed MPPT algorithm in finding the GMPP in PS conditions, two I-V curves are taken into account as shown in Fig. 3.23. In the first case (Fig. 3.23-case (a)), the P-V curve includes two peaks at (17.5 V, 57 W) and

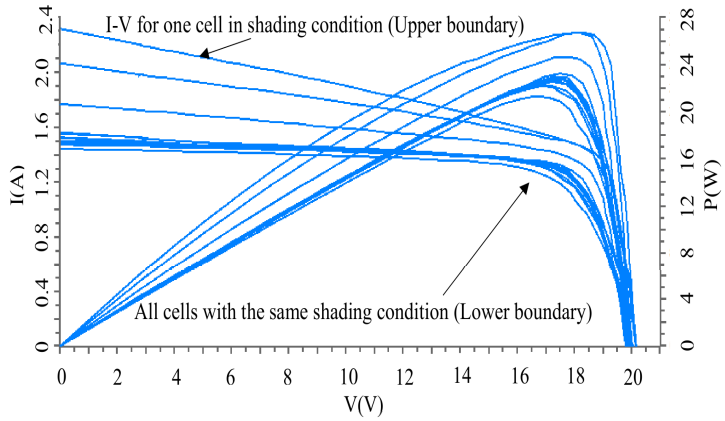

Figure 3.22: The I-V and P-V curves of the ET-M53695 PV panel measured by the I-V 400W Photovoltaic Panel Analyzer.

(37.5 V, 37 W) where the GMPP occurs at a lower voltage. In the second case (Fig. 3.23-case (b)), the P-V curve features two peaks at (17.5 V, 57 W) and (37.5 V, 72 W) and the GMPP occurs at a higher voltage. A series of experiments are carried out using the traditional PSO technique to highlight its weakness to find the GMPP. Three duty cycles are regarded (0.1, 0.5 and 0.8) as particles. Also, ω, c_1 and c_2 are set to 0.3, 0.2 and 0.5, respectively.

Fig. 3.24 shows the current, voltage and generated power using the traditional PSO method for case (a). As seen the GMPP is detected, but the tracking time is high and it takes 1.8 sec to reach the steady state condition.

This long tracking time has detrimental impact on the generated power because it leads to power fluctuations. By setting c_2 to 0.8, the convergence time decreases to 1 *sec*; however, as seen in Fig. 3.25, the LMPP is detected. Thus, in spite of using the traditional PSO MPPT method, getting stuck in the LMPP is unavoidable. Also, to prove the stability analysis, the random values (r_1 and r_2) are set to 1 and the parameters are set to 0.3, 0.2 and 2.3 for ω, c_1 and c_2, respectively. According to (3.6), the sum of c_1 and c_2 must be less than 2.6 while it is 2.5, therefore a stable response is expected.

As seen in Fig. 3.26, though the response is stable, the convergence time is excessive. On the other hand, when the parameters are set to 0.3, 0.2 and 2.5, the sum of c_1 and c_2 is 2.7 which is greater than 2.6 and the system becomes unstable. Fig. 3.27 shows the instability of the current, voltage and power.

The proposed MPPT method is also implemented experimentally for both PS conditions shown in Fig. 3.28 and ω and c_g are set to 0.2 and 0.7, respectively. This figure

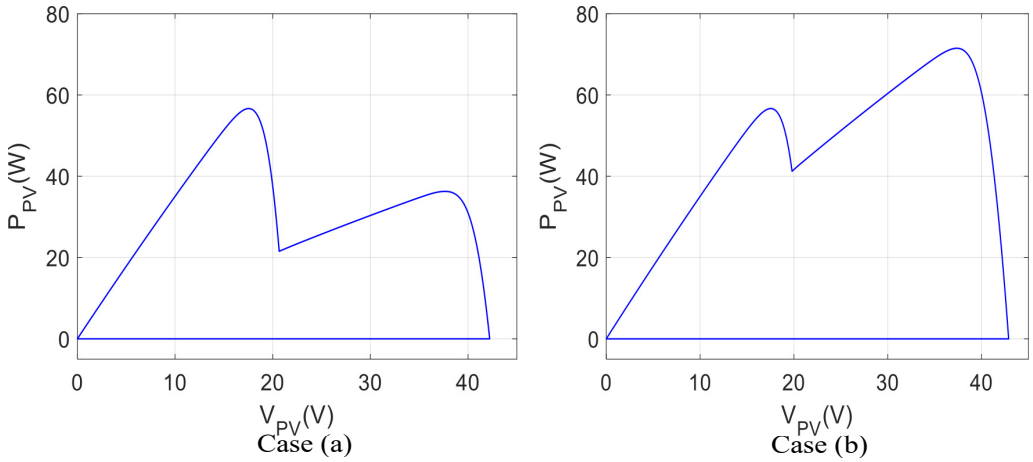

Figure 3.23: The P-V curve of the PV panel for experimental verification of the ANN-based MPPT algorithm.

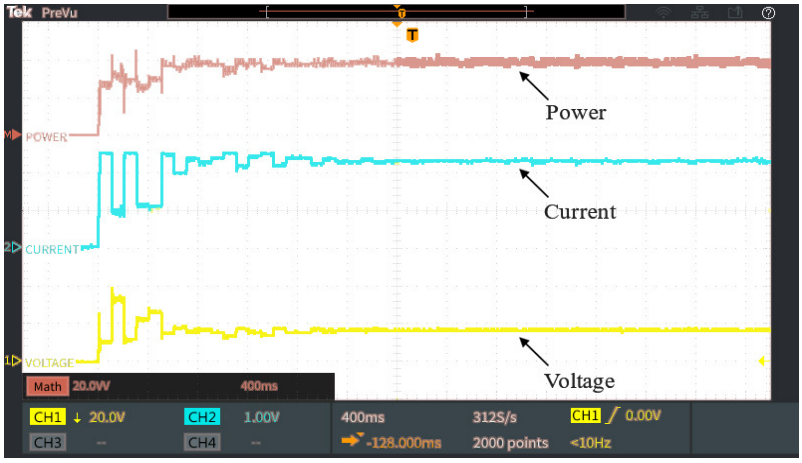

Figure 3.24: Generated power, voltage and current using traditional PSO algorithm for ω, c_1 and c_2 equal to 0.3, 0.2 and 0.5, respectively.

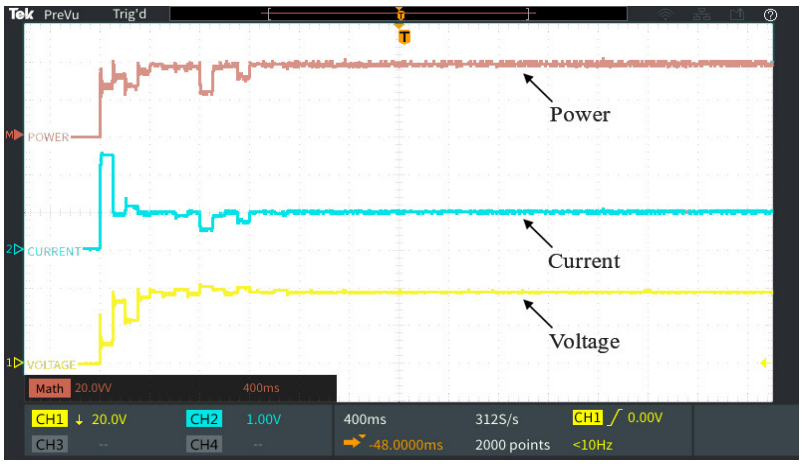

Figure 3.25: Generated power, voltage and current using traditional PSO algorithm for ω, c_1 and c_2 equal to 0.3, 0.2 and 0.8, respectively.

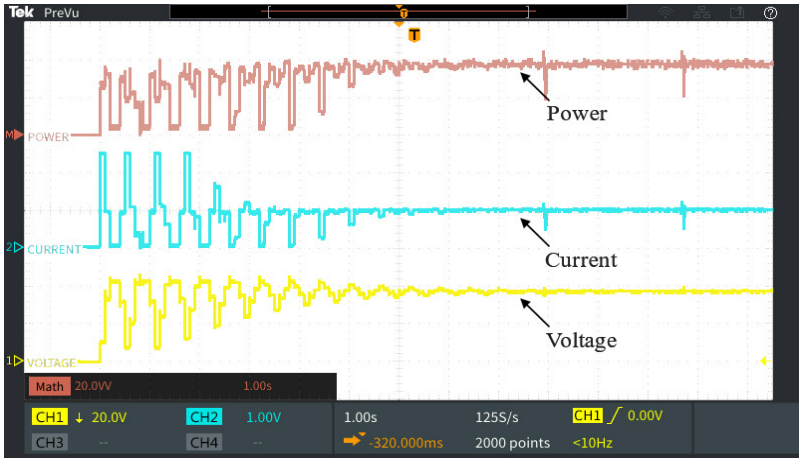

Figure 3.26: Generated power, voltage and current using traditional PSO algorithm for ω, c_1 and c_2 equal to 0.3, 0.2 and 2.5, respectively.

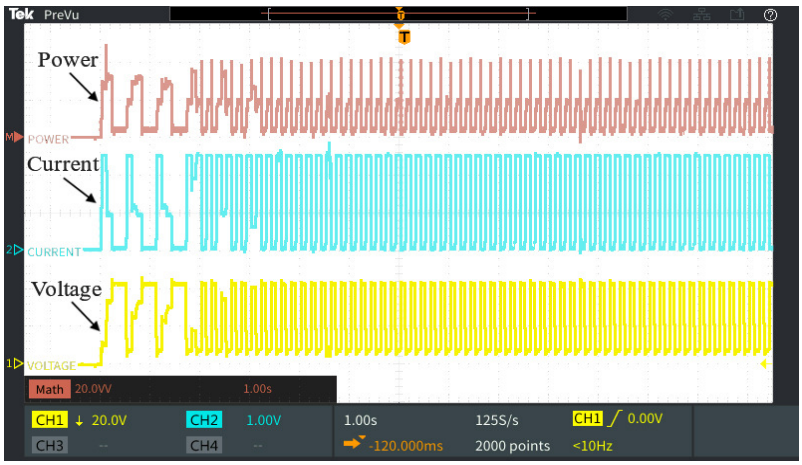

Figure 3.27: Generated power, voltage and current using traditional PSO algorithm for ω, c_1 and c_2 equal to 0.3, 0.2 and 2.7, respectively.

shows the current, voltage and power for case (a) where the GMPP occurs at a lower voltage. To highlight the capability of the proposed technique in terms of the convergence time and fluctuation, Fig. 3.29 compares the generated power of the proposed solution with that of the traditional PSO technique. As seen, the convergence time of the proposed method is around 200 $msec$ and decreases significantly in comparison to the traditional PSO method which is 1.8 sec. Also, because of this short tracking time, the fluctuations on the generated power are considerably improved and the energy losses are decreased. In this case, the harvested energy is 91 % and 98 % at $t = 2$ sec using the traditional PSO and the proposed one, respectively, which represents an improvement of 7 %.

Due to the fact that the upper and lower boundaries for the area in where the GMPP exists are determined in the proposed PSO MPPT method at the initial step, it converges to the GMPP fast. In addition, since the search area, limited between two boundaries, is a convex area, therefore, the term related the best personal particle is eliminated. Hence, the fluctuation in the generated power is considerably decreased in the proposed technique. In fact, it is challenging to determine the values of the coefficients in the traditional PSO technique as large changes in particles evolution may lead to a fast convergence while it has the risk of failing to find the GMPP as seen in Fig. 3.25. This issue has been solved in the proposed technique in a way that the coefficient c_g in (3.8) can be chosen a larger value in comparison to the values of c_1 and c_2 in (3.1) to decrease the response time. However, the criterion of (3.11) for the proposed method should be

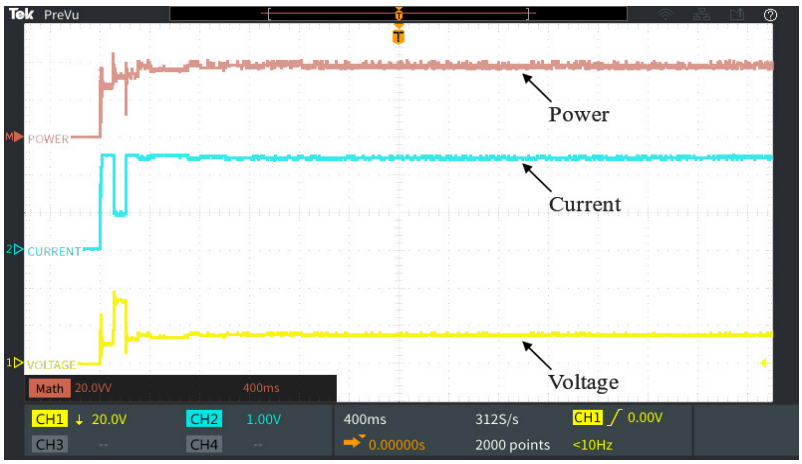

Figure 3.28: Generated power, voltage and current using the proposed PSO algorithm for case (a) and ω and c_g equal to 0.2 and 0.7, respectively.

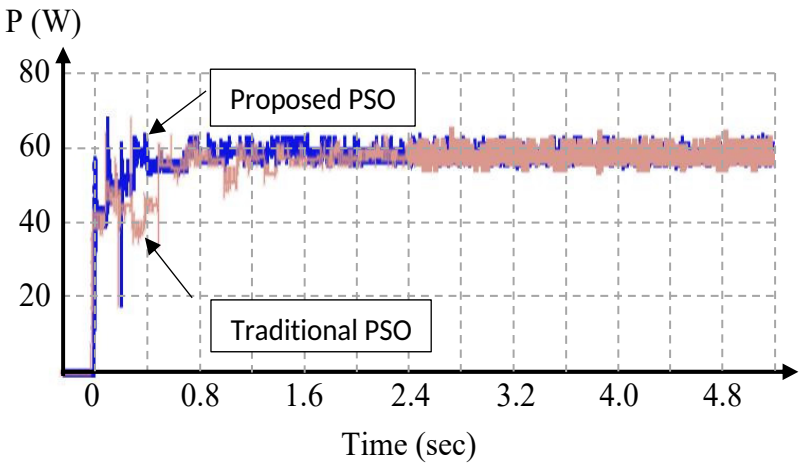

Figure 3.29: Generated power using the traditional and proposed PSO MPPT algorithms.

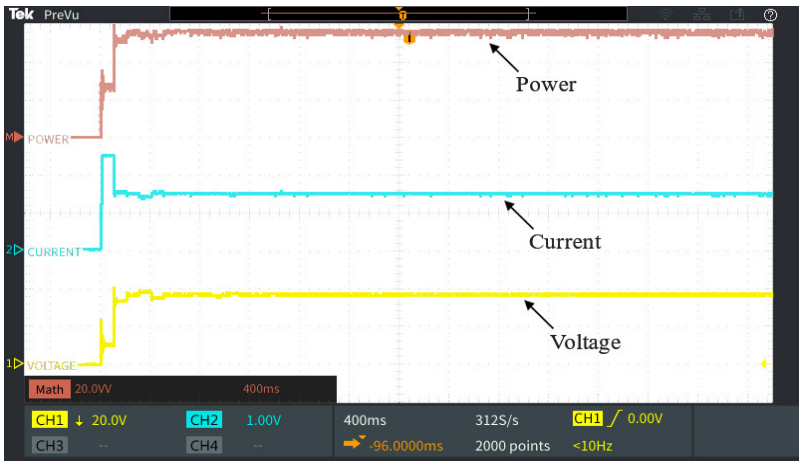

Figure 3.30: Generated power, voltage and current using the proposed PSO algorithm for case (b) and ω and c_g equal to 0.2 and 0.7, respectively.

satisfied for the stability purpose leading to the GMPP tracking. In spite of this fact, fluctuations still exist in the generated power in steady state condition even using the proposed method because of the momentum value in (3.8). This part cannot be omitted because if GMPP changes as a result of variations in the irradiation value, temperature, etc., the proposed PSO is required to find the new GMPP. Fig. 3.30 shows the voltage, current and power when the proposed MPPT tracks the GMPP for case (b); similar to case (a), the proposed MPPT algorithm is able to find the GMPP fast, with negligible fluctuations. In addition, contrary to the traditional PSO technique, it avoids getting stuck in the LMPP.

3.4.2 Converter Based MPPT Method

3.4.2.1 Simulation Results

The simulation setup mainly consists of the ET-M53695 PV panel, the proposed converter with an isolated transformer and a resistive load connected to the output. The values for I_{SC}, V_{OC} and peak power of the PV panel are 5.57 A, 22.5 V and 95 W, respectively. Also, it is comprised of two modules of PV cells with 18 cells in each module and its maximum power point is around $0.8 \times V_{OC} = 18\ V$. Consequently, for each module, this value is around 9 V. As a result, the operating voltage of the PV panel is between 9 V and 18 V. In addition, the insolation is regarded between 20% and

100% of nominal one, therefore, the operating current is between 1 A and 5 A.

$$\begin{aligned} 1 \leq I_{OP} \leq 5 \\ 9 \leq V_{OP} \leq 18 \end{aligned} \tag{3.44}$$

Moreover, it is supposed that 10% of voltage drop in V_{in} is acceptable and k in (3.38) is regarded as 0.1 to avoid having large L_m, however, the value of k should be checked after calculation of L_m to have the acceptable voltage drop at the terminal. T_{ON_max} can be calculated using (3.38) and (3.44). C_{in} is regarded as 470 uF, therefore, the minimum value of T_{ON_max} is 761.4 $usec$. This time can be longer by adding an extra capacitor in parallel with C_{in} to implement the scanning circuit using a simpler and cheaper microcontroller which has slower analog to digital peripheral. V_{DC} is chosen 10 V, so L_m can be calculated according to (3.41) and (3.42).

$$L_m \leq 1.903mH \tag{3.45}$$

$$L_m \leq 1.523mH \tag{3.46}$$

Consequently, L_m must be less than 1.523 mH in which the value of 1.0 mH was used for the simulation. As it was mentioned, the value of k should be checked to ensure the voltage drop is in the acceptable range. When the MOSFET of the scan circuit turns on, the load is supplied only by the terminal capacitor, therefore, the equivalent resistance of the load and the terminal capacitor (C_{in}) are connected as a resistive-capacitive circuit. The equivalent resistances of the load at 5 A and 1 A for V_{OP} equal to 18 V are 3.6 Ω and 18 Ω, respectively, therefore, the time constants are 1.692 $msec$ and 7.520 $msec$. On the other hand, when the MOSFET turns on, the required time to increase the current of L_m from 5 A and 1 A to a value more than the short-circuit current of the PV panel (5.5 A) is 0.05 $msec$ and 0.45 $msec$, respectively. According to the time constant of the output stage (1.692 $msec$ and 7.520 $msec$ for 5 A and 1 A, respectively), the voltage drops at $t = 0.05$ $msec$ is 2.91% when I_{OP} is 5 A and it is 5.81% at $t = 0.45$ $msec$ for I_{OP} equals to 1 A, consequently, the value of k is suitable. When the voltage drop is more than 10% with a specific value of k, a parallel capacitor can be added at the terminal or the value of L_m can be chosen as a smaller value. Since the PV panel under study has two PV modules, therefore, the I-V curve includes two MPPs in partial shading conditions. The voltage and current levels related to these MPPs depend on the irradiation and

temperature. Hence, different partial shading scenarios are defined and the performance of the proposed method is examined to scan the I-V curve. Fig. 3.31 and Fig. 3.32 show different I-V curves corresponding to two different irradiation patterns i.e., high and low partial shading conditions as well as the simulated waveforms of the current and voltage of the PV panel. Two cases namely case (a) where the operating point is in a lower voltage value and case (b) where this point is set in a higher voltage value are considered. The current and voltage waveforms for both left-hand side and right-hand side scanning operations are shown consecutively from top to bottom that prove the proposed scanning analyses. The same procedure was repeated in low partial shading conditions to validate the proper operation of the scanning converter as shown in Fig. 3.32.

The capability of the proposed scanning technique was also examined when the PV panel is in a dynamic environment. For example, when the PV panel is mounted on a moving object, as a result, the value and direction of the irradiation change rapidly. In this condition, a fast GMPP detection method is essential to avoid energy losses. One of the main advantages of the proposed method is its short response time to detect the IV curve. Therefore, it can be used to detect the GMPP and to increase the amount of the harvested energy in this condition. To simulate this condition, the irradiation value was changed from 200 $\frac{W}{m^2}$ to 1000 $\frac{W}{m^2}$ and vice versa in 1 sec as shown in Fig. 3.33-(a). Fig. 3.33-(b) shows the response of the proposed circuit which operates every 50 $msec$. In other words, the GMPP is detected every 50 $msec$, however, the detection period can be decreased to provide a very fast response time. In this simulation, the period of the GMPP detection can be decreased to a value less than 10 $msec$ because the operation of the scanner circuit takes around 6.5 $msec$ with the above-mentioned parameter values.

3.4.2.2 Experimental Results

Fig. 3.34 shows the experimental setup consisting of a resistive load, the TMS320F28335 DSP microcontroller, the ET-M53695 PV panel, the scanning converter, current and voltage sensors, power supplies and an oscilloscope. Other parameters of the setup are presented in Table 3.2.

The nominal power of the PV panel is 100 W, therefore, $EE42$ ferrite core was used to design the transformer to handle this amount of power. The maximum current of the secondary winding is 5 A and the effective area of the core is 233 mm^2, consequently, the number of turns in the secondary winding is 71 turns regarding the maximum flux

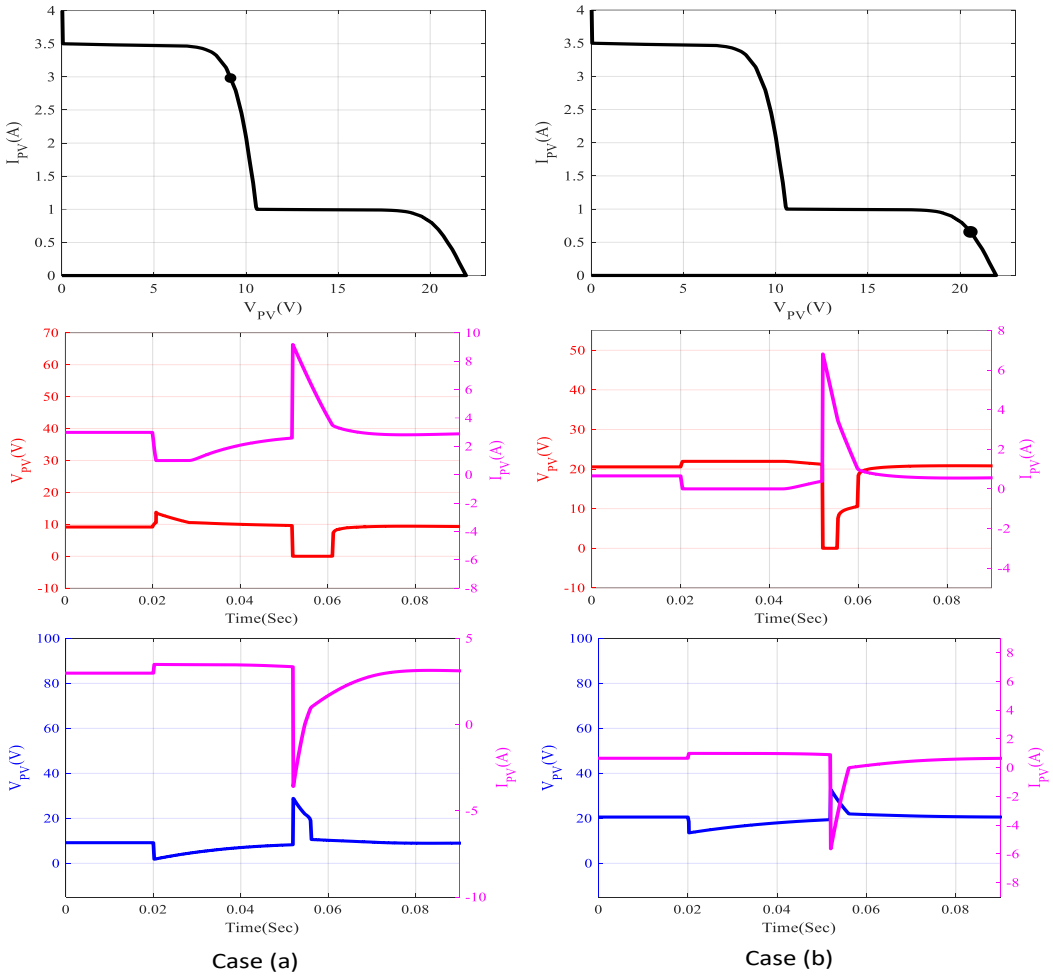

Figure 3.31: The waveforms for high partial shading ratio (from top to bottom: the I-V curve of the PV panel, the left-hand side scanning current and voltage waveforms and the right-hand side scanning current and voltage waveforms).

Table 3.2: Parameters of the system for the I-V scanning circuit verification.

Parameter	Description	Value
L_m	Magnetizing inductance	$1\,mH$
C_{in}	PV panel terminal capacitor	$470\,\mu F$
$Q_{1,2}$	Mosfets	$IRF3205LPBF$
$D_{S,P,F}$	Diodes	$ST15150$
V_{DC}	DC voltage source	$10\,V$

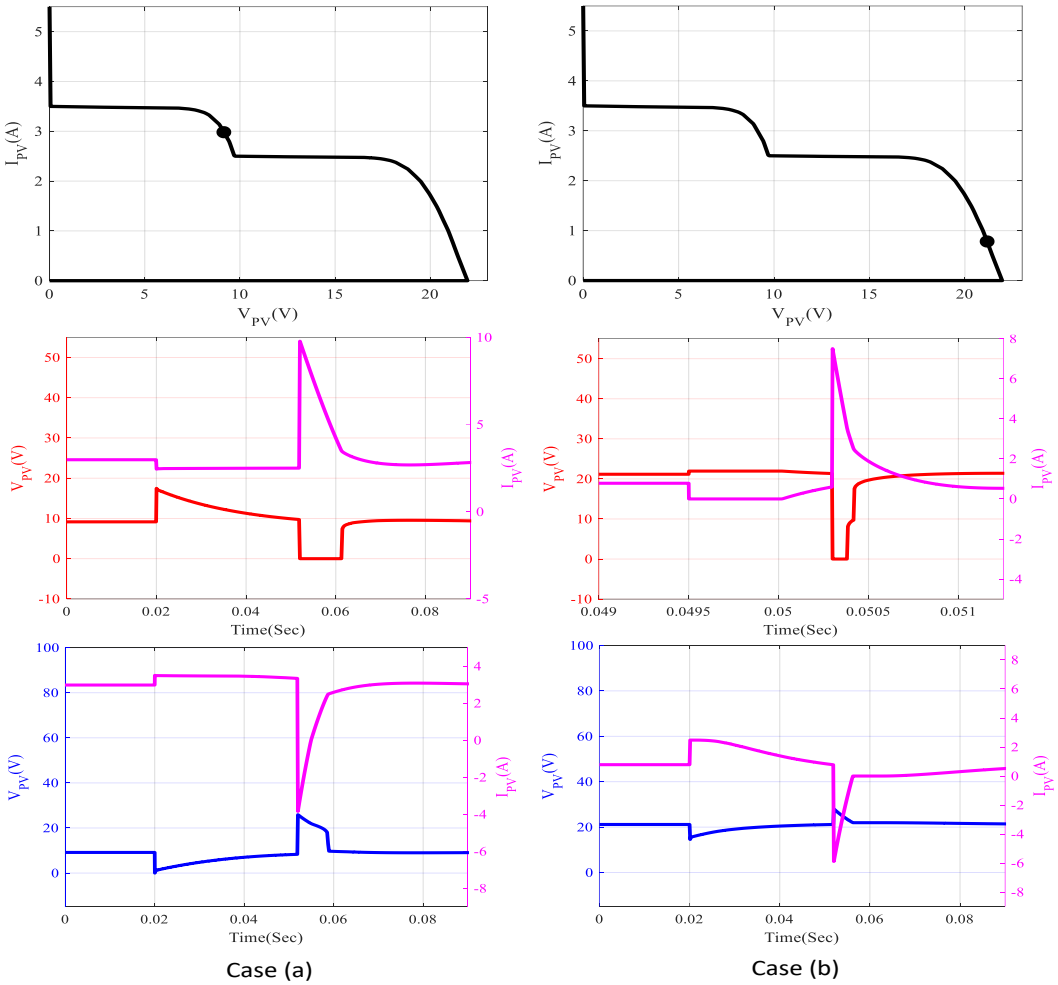

Figure 3.32: The waveforms for low partial shading ratio (from top to bottom: the I-V curve of the PV panel, the left-hand side scanning current and voltage waveforms and the right-hand side scanning current and voltage waveforms).

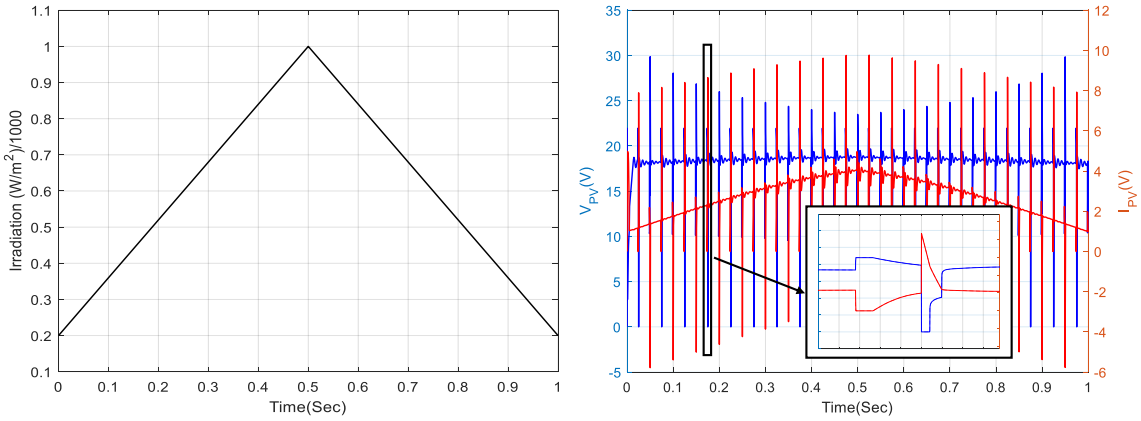

(a) (b)

Figure 3.33: The operation in a dynamic environment. (a) The irradiation. (b) The performance of the proposed method.

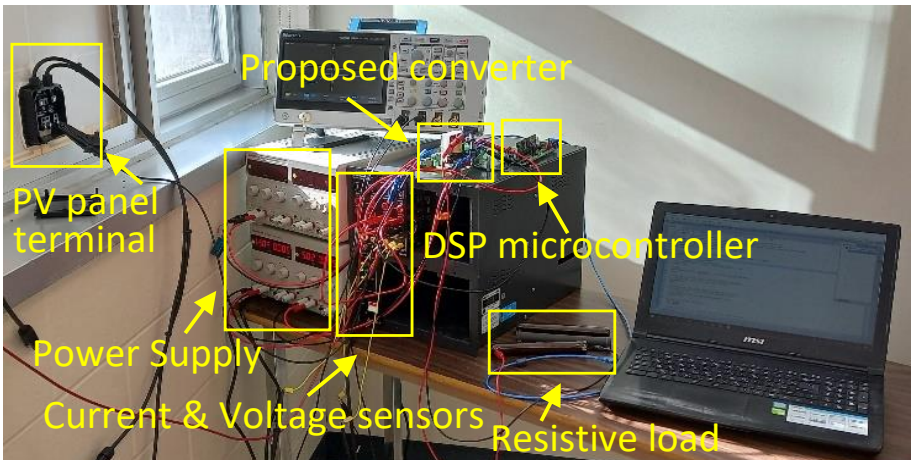

Figure 3.34: The experimental setup for the I-V scanning circuit verification.

density, and the magnetizing inductance equal to 0.3 T and 1 mH, respectively. The number of turns in the primary windings turns is 71 supposing the primary and the secondary voltage values are equal. In addition, the air gap was calculated as 1.4 mm. Also, the wire gauge of the secondary winding is 23 to flow the PV nominal current which is 5 A. The primary winding gauge can be chosen less than the secondary one because it does not carry the nominal current of the PV panel, however, the same gauge value was chosen for the primary windings. The shading condition was created by attaching some pieces of rectangle-shaped paper to the PV cell. The ratio of area covered by the papers to the total area of the PV cell determines the shading ratio.

Fig. 3.35 exhibits the experimental results of the proposed circuit for a high shading value where the ratio of shading is 70%. Two operational points were set by adjusting the resistive load. The RHS and LHS trajectories are distinguished by blue and red colors. In case (a), the resistance of the load is 1.8 Ω and as seen, most parts of the curve were scanned by the RHS operation. To examine the operation of the scanning circuit in higher voltage, the resistive load was adjusted to 25 Ω (case (b)). Unlike to the previous case, most of the I-V curve was scanned in the LHS phase. On the other hand, the operation of the proposed method in light shading conditions (20%) was assessed as highlighted in Fig. 3.36. Similar to the high shading condition, the I-V curve was scanned by the RHS and LHS operations in low and high resistance levels respectively. Also, the voltage of the capacitor at the terminal of the PV panel (V_{in}) is shown in Fig. 3.37. As seen, the voltage drop is around 9.5% which is acceptable.

In addition, in order to further evaluate the capability of the proposed method in the GMPP detection, different shading ratios such as 20%, 40% and 70% were taken into account as shown in Fig. 3.38. When the shading ratio is 70%, the GMPP occurs in a low voltage (point A) and as soon as the shading ratio decreases, the GMPP changes to point B and then to point C. Therefore, the scanning circuit can be used to detect the GMPP. In this way, it can either work as an MPPT algorithm, or it can help the MPPT algorithm of the system by preparing the information about the GMPP to avoid getting stuck at an LMPP.

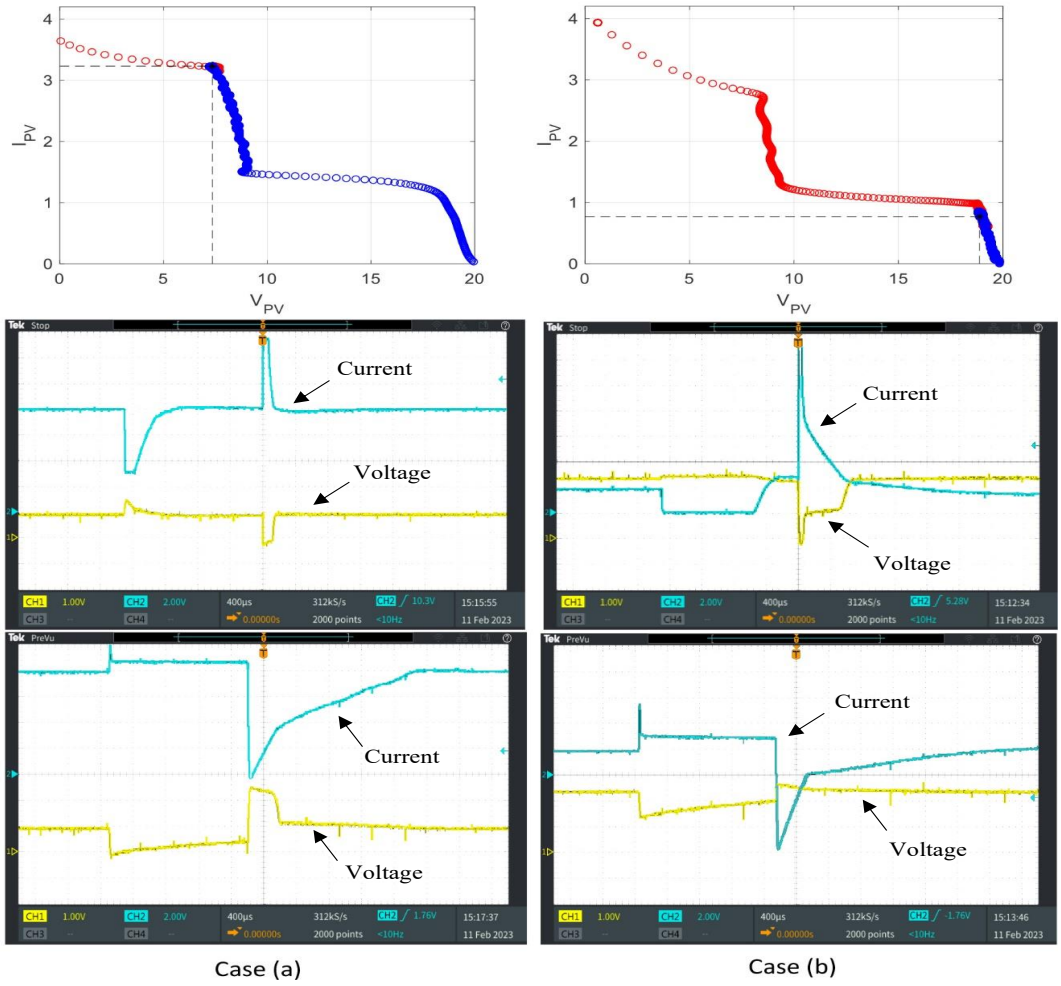

Figure 3.35: The experimental results of the proposed method for the I-V curve in the high partial shading condition.

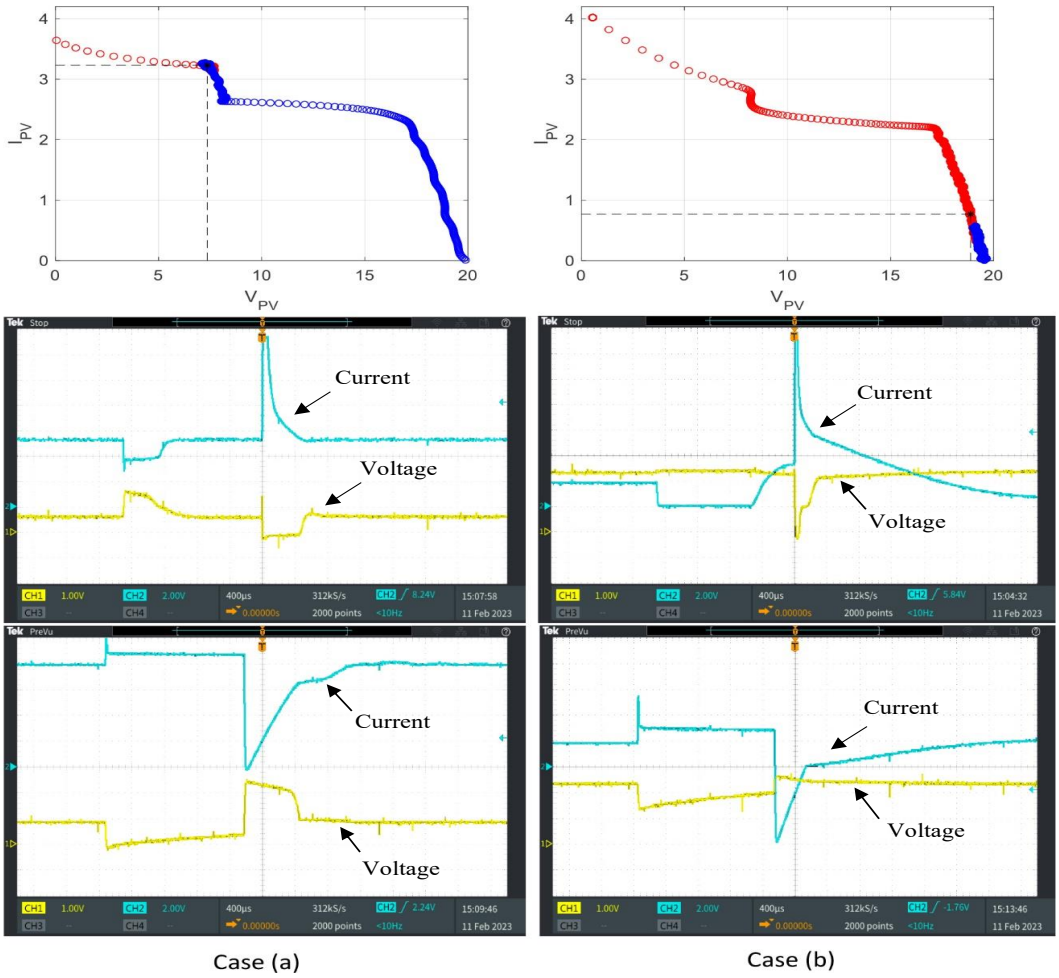

Figure 3.36: The experimental results of the proposed method for the IV curve in the low partial shading condition.

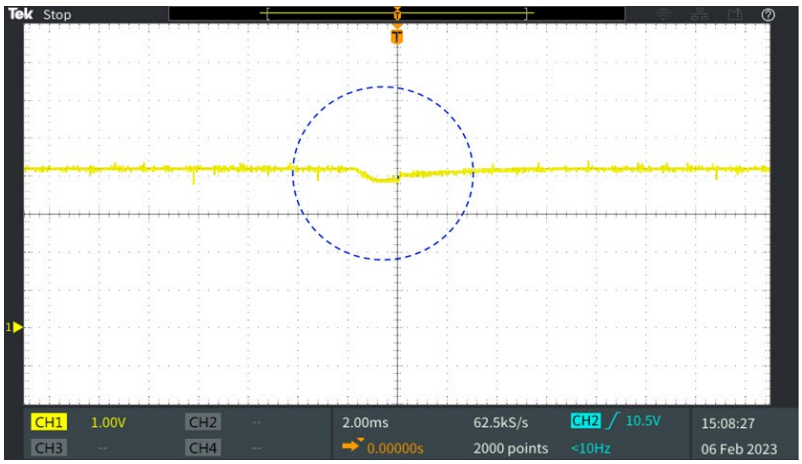

Figure 3.37: The V_{in} waveform when the scanning converter operates.

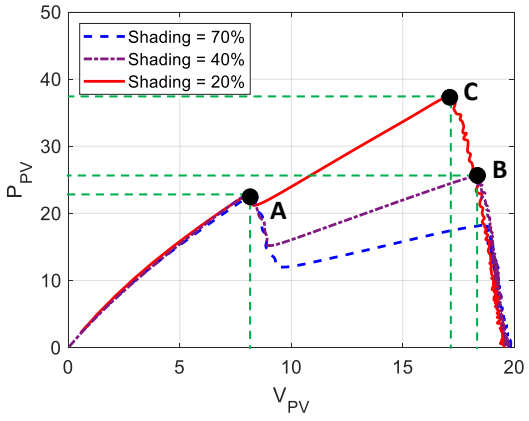

Figure 3.38: The experimental results of the proposed method for the power versus voltage curve when the partial shading value changes.

Chapter 4

A Fast Converter-Based PS Detector

4.1 Introduction

In this chapter, a fast converter-based PS detector is proposed. Besides fast PS detection, it does not have any detrimental effect on the terminal capacitor. First, the notion behind the idea is described, and then it is followed by an implementation. A rising current pulse is required to sweep the I-V curve for the PS detector. To generate this pulse, a wave-shaping circuit is used which operates independently from the terminal optimizer. The main elements design of the PS detector is discussed and a prototype was prepared based on the design criteria for the experimental verification. Finally, some tests were conducted in different PS scenarios and their results are presented to show the performance of the proposed method.

4.2 The Proposed Idea and Its Implementation

When the PV panels are working under uniform shading conditions, the operating voltage is around $0.8 \times V_{oc}$ where V_{oc} is the open-circuit voltage [110]-[112]. On the other hand, the open-circuit voltage value is not affected significantly by changing the irradiation. Consequently, the operating voltage in a normal condition is around $0.8 \times V_{oc\_STC}$ (V_{oc_STC} is the open-circuit voltage of the PV panels at the standard test condition) as it is shown in Fig. 4.1 for four PV panels in series configuration by a dashed area. However, when the system works in this area, it does not mean that PS condition has not occurred. For example, while both points $\boldsymbol{P_P}$ and $\boldsymbol{P_U}$ are in

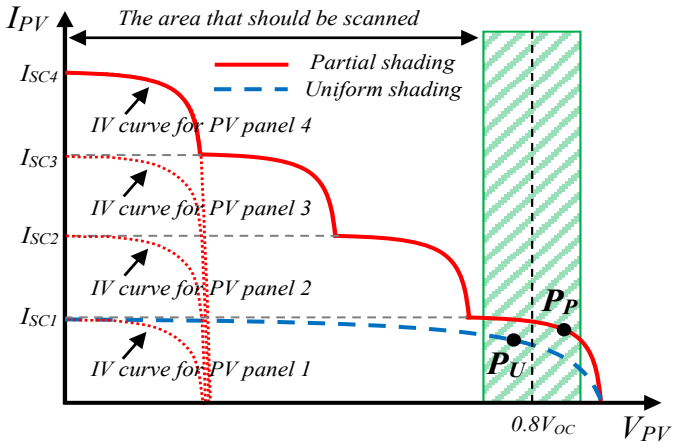

Figure 4.1: The scanning area to detect the PS shading.

the dashed area, just the former is in the PS condition. Despite this fact, there is a significant difference between the operating current and the short-circuit current in the PS condition; therefore, one of the best ways to detect the PS condition is by measuring the short-circuit current of the PV panels. In addition, if the short-circuit current of each PV panel in their series combination is available, their shading rate can be estimated because the short-circuit current is proportional to the irradiation value. Measuring the short-circuit current is not possible easily in practice because a parallel electrolytic capacitor is connected to the series combination of the PV panels and it can be damaged or its lifetime decreases if it becomes short-circuit. Fig. 4.2 exhibits the proposed method to detect the partial shading condition. As seen, a current source is placed in series between the PV panels and the terminal capacitor; therefore, its current is equal to the PV panel current (I_{PV}). To detect the PS condition, its current increases to I_{max} during T_{DE} time. If I_{max} is greater than the PV panel short-circuit current and V_{PV} and I_{PV} are sampled in this period, the PV panels' output characteristics can be scanned. This information can be analyzed to evaluate the irradiation value of each PV panel. In this way, the short-circuit on the terminal capacitor (C_{Tr}) is avoided, however, its voltage drops, because the load is supplied by the PV panels and C_{Tr} during T_{DE}.

The current source generates a short-period pulse; therefore, it can be implemented by controlling the current of a series inductor to have a suitable waveform. When the current of the PV panel increases, its voltage decreases. This feature can be used to shape the current of the series inductor. Fig. 4.3 shows the implementation of the proposed method.

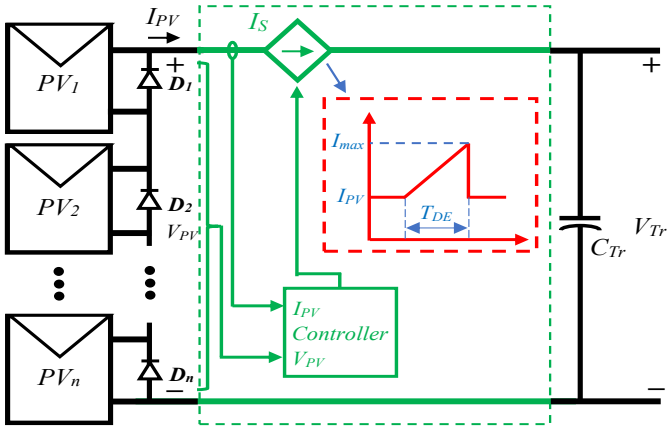

Figure 4.2: Proposed method to detect the PS shading.

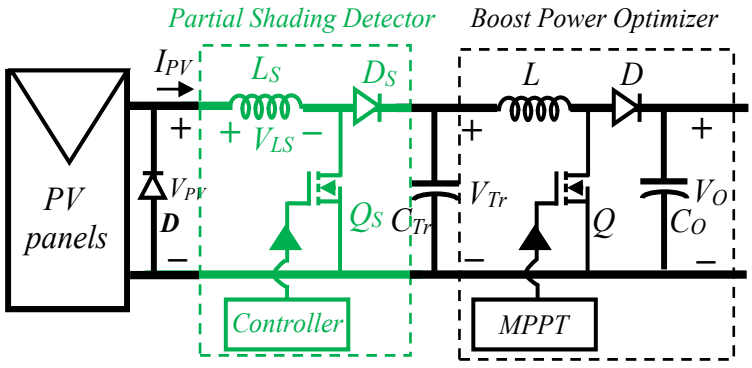

Figure 4.3: Implementation of the proposed method to detect the PS shading using a wave-shaping converter.

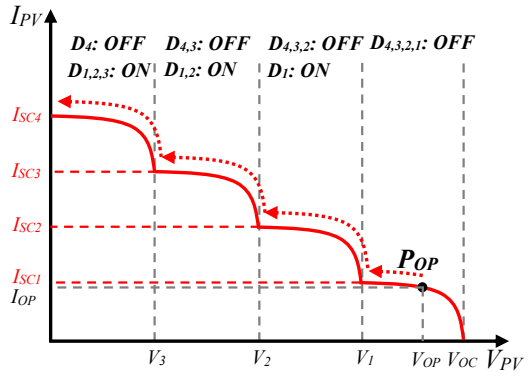

Figure 4.4: Operation of the proposed method on the I-V curve.

As seen, an inductor is placed between the PV panels and C_{Tr}. Also, a MOSFET is used to operate as a wave-shaping circuit in combination with this inductor. When the MOSFET turns on the inductor current increases because of the positive voltage of V_{PV}. Also as mentioned before, the output capacitance of the PV panels is negligible in comparison to C_{Tr}, as a result, if T_{DE} be short enough, V_{Tr} is almost constant during this period. It means that V_{PV} decreases because I_{PV} increases while V_{Tr} is almost constant and greater than V_{PV} during T_{DE}. Consequently, when the MOSFET turns off, the voltage drop across the inductor is negative and its current decreases. In general, the volt-second balance of the inductor is satisfied in this circuit; therefore, the current can be shaped. Fig. 4.4 and Fig. 4.5 show the operation of this method on the I-V curve and its waveforms, respectively. As seen, contrary to the previous method, the current is shaped by switching. Consequently, a small capacitor is required at the terminal of the PV panel to eliminate the switching fluctuation in the current.

When the current is increasing from I_{OP} to I_{max}, the anti-parallel diode of the PV panels becomes forward-biased. For example, in Fig. 4.4, between I_{SC4} and I_{SC3} the anti-parallel diode of PV panel number 4 (D_4) is reverse biased and the other ones are forward biased. On the other hand, if PS is not occured which means all PV panels have the same shading condition, all anti-parallel diodes become reverse-biased simultaneously. Therefore, PS occurrence can be detected by measuring the voltage drop across the anti-parallel diodes during T_{DE}. To implement this method, a measuring device must be mounted at the terminal of each PV panel which increases the complexity and the price of the system. Another solution is measuring the voltage and current at the terminal of the series combination of the PV panel where the PS detecting circuit is installed.

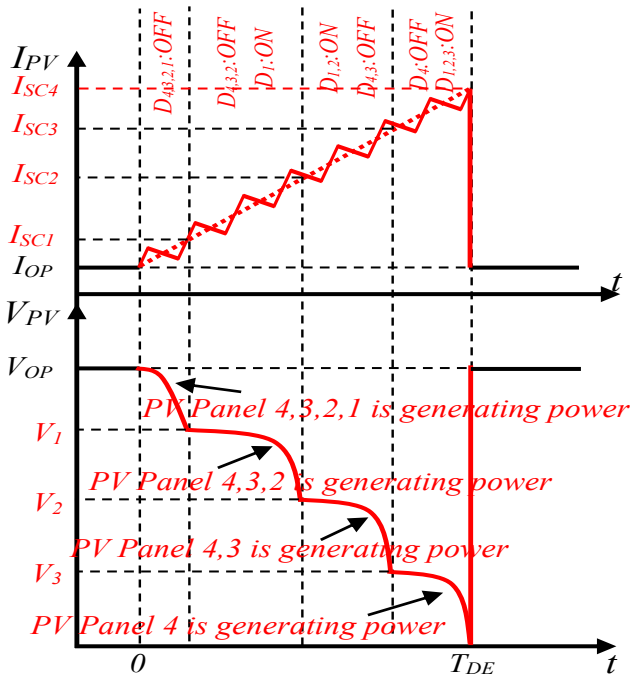

Figure 4.5: Waveforms of the short-circuit current detection circuit.

After sampling the whole curve, PS condition can be detected. Each step on the voltage waveform shows a PV module with different shading conditions and if there is not any step on this waveform, it means the irradiation on the PV modules is uniform.

4.3 PS Detection Circuit Design

Two main parameters of the PS detection circuit are the maximum length of the current pulse (T_{DE}) and the inductor (L_S). The load is supplied by both the PV panel and the terminal capacitor (C_{Tr}) during the PS detection procedure; therefore, the terminal voltage (V_{Tr}) decreases. T_{DE} is determined to limit this voltage drop to an acceptable range. As mentioned before, the operating voltage in non-shading conditions is around $0.8 \times V_{OC}$ and it does not change significantly. But the operating current can be regarded between two maximum and minimum values depending on the irradiation values.

$$I_{OP\_\min} \leq I_{OP} \leq I_{OP\_\max} \tag{4.1}$$

As seen in Fig. 4.6, when the current increases from zero to a maximum short-circuit current (I_{SC_max}), the required time to achieve the output characteristics of the PV panel changes depending on the irradiation value and the PS condition. When the irradiation is uniform and has the maximum value, the required time is T_1 and it happens at the rightmost of the current waveform. On the other hand, this value is T_2 for the minimum uniform irradiation and occurs at the leftmost part of the current waveform. This time is the maximum value (T_{DE}) when the PS condition occurs and there is at least one PV panel with the maximum irradiation value and one PV panel with the minimum irradiation value. Also, the difference between the load power and the generated power by the PV panels during the PS condition is maximum for the maximum irradiation value, however, the PS detection time (T_1) is less than T_{DE}. Therefore, it is not the worst condition in view of the voltage drop of the terminal capacitor during the PS detection. For this purpose, it can be supposed that the load is maximum and PS detection time for the maximum uniform irradiation condition is T_{DE} as seen in Fig. 4.7. In practice, it does not happen but this assumption guarantees the minimum voltage drop for V_{Tr}. Also, to simplify the calculation, it can be supposed that the PV panel voltage drops linearly from V_{OP} to zero. Again, this voltage is less than the PV panel voltage as seen in Fig. 4.7, consequently, the calculated T_{DE} guarantees the voltage drop of V_{Tr}.

Equations (4.2) and (4.3) show the function of PV panel voltage and current during PS detection, respectively. The difference between the generated power and energy by the PV panel and the consumed ones by the maximum load (P_{L_max}) during T_{DE} are shown in (4.4) and (4.5), respectively.

$$i_{pv}(t) = I_{OP\_max} + \frac{I_{SC\_\max} - I_{OP\_max}}{T_{DE}} t \tag{4.2}$$

$$v_{pv}(t) = V_{OP} - \frac{V_{OP}}{T_{DE}} t \tag{4.3}$$

$$\begin{aligned} &P_{L\_max} = V_{OP} I_{OP\_max} \\ &P_{PV} = \left(V_{OP} - \frac{V_{OP}}{T_{DE}} t\right)\left(I_{OP\_max} + \frac{I_{SC\_\max} - I_{OP\_max}}{T_{DE}} t\right) \\ &P_{diff} = P_L - P_{PV} = \\ &\left(\left(2I_{OP\_max} - I_{SC\_\max}\right) + \left(\frac{I_{SC\_\max} - I_{OP\_max}}{T_{DE}}\right) t\right) \frac{V_{OP}}{T_{DE}} t \end{aligned} \tag{4.4}$$

$$E_{diff} = \int_0^{T_{DE}} P_{diff} dt = \left(\frac{2}{3} I_{OP\_max} - \frac{1}{6} I_{SC\_\max}\right) T_{DE} V_{OP} \tag{4.5}$$

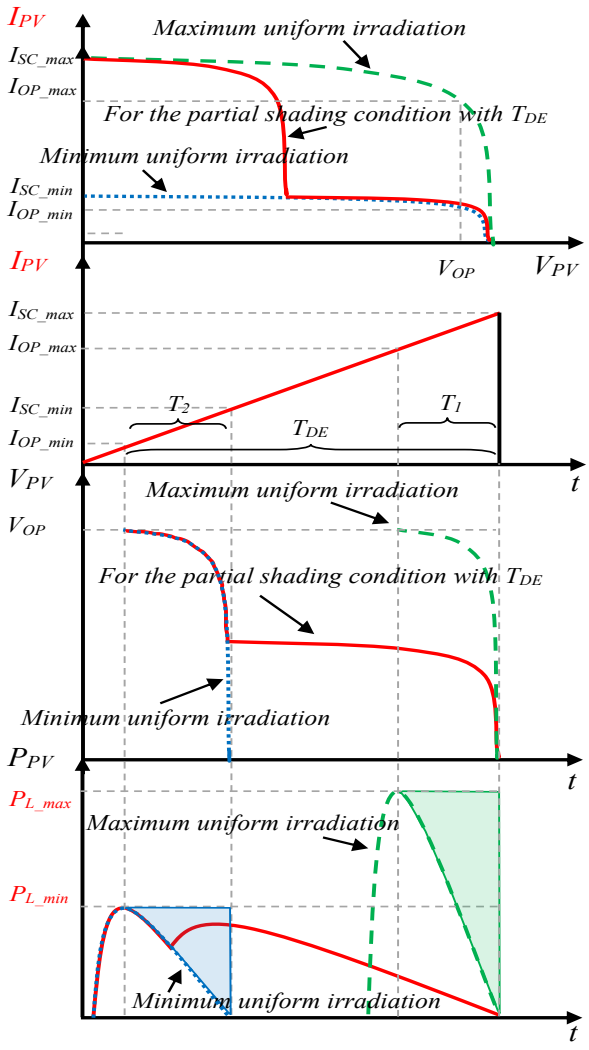

Figure 4.6: Operation of the system for different conditions.

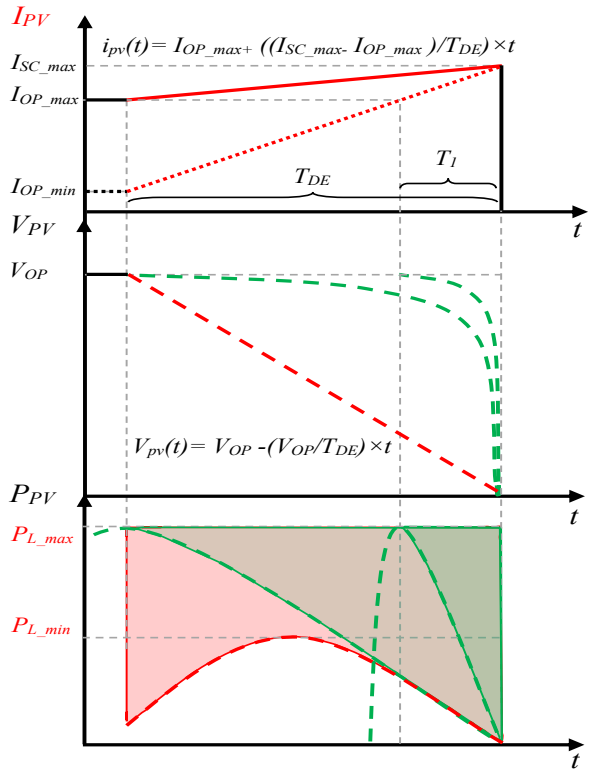

Figure 4.7: Current and Voltage Waveforms for design.

The difference between the generated energy results in a voltage drop at the terminal voltage (V_{Tr}) and it is supplied by the terminal capacitor (C_{Tr}). Supposing, 10% in voltage drop is acceptable, as a result, the supplied energy by C_{Tr} during T_{DE} is shown in (4.6).

$$E_{diff} = \frac{1}{2}C_{Tr}V_{Tr}^2 - \frac{1}{2}C_{Tr}(0.9V_{Tr})^2 = 0.1C_{Tr}V_{Tr}^2 \tag{4.6}$$

V_{Tr} is equal to V_{OP}, therefore, the maximum value of T_{DE} can be calculated by (4.5) and (4.6).

$$T_{DE} = \frac{0.1V_{OP}}{\frac{2}{3}I_{OP\_max} - \frac{1}{6}I_{SC\_\max}}C_{Tr} \tag{4.7}$$

I_{OP_max} is around I_{SC_max}, therefore, T_{DE} can be calculated by (4.8).

$$T_{DE} = \frac{0.2V_{OP}}{I_{OP\_max}}C_{Tr} \tag{4.8}$$

The PS detecting circuit should work in CCM to shape the current and decrease the switching ripples as much as possible. Fig. 4.8 shows the inductor current for CCM, CRM, and DCM. The average of the inductor current is equal to the PV panel current (I_{PV}) and its ripple is shown in (4.9).

$$\Delta I = \frac{V_{PV}}{2L_S f_{sw}}D \tag{4.9}$$

where D and f_{sw} are the duty cycle and the switching frequency, respectively. CRM occurs when I_{PV} is equal to ΔI, therefore, the minimum value of L_S to have CCM can be calculated by (4.2) and (4.9) which is shown in (4.10).

$$L_S \geq \frac{V_{PV}}{2I_{PV}f_{sw}}D \tag{4.10}$$

The maximum value of D is 1, therefore, the value of L_S should be calculated by (4.11) to guarantee the CCM operation.

$$L_S \geq \frac{V_{PV}}{2I_{PV\_\min}f_{sw}} \tag{4.11}$$

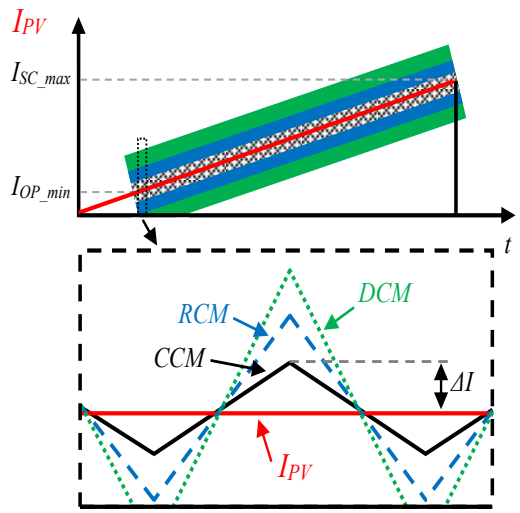

Figure 4.8: Inductor current for different operation modes.

To decrease the switching ripples in I_{PV}, a larger value of L_S should be chosen however a small values capacitor in parallel to the PV panel can be used to decrease these ripples in I_{PV}.

4.4 Experimental Verification

Fig. 4.9 shows a setup for the proposed PS detection method which mainly consists of current and voltage sensors, two ET-M53695 PV panels, resistive load and the PS detection circuit. Each PV panel has two PV modules; therefore, four modules are in series and connected to the PS detection circuit.

Fig. 4.10 exhibits a control system for the PS detection circuit based on UC3843 power supply controller which is a current mode controller. The current ramp reference voltage is generated by charging a 22 uF capacitor at pin 1 of this IC using an internal 1 mA current source. The current ramp is triggered using a timer every 7 seconds and ended by comparing the PV panel voltage with zero using a comparator (LM339). It takes around 20 $msec$ from zero to 5 A for this capacitor and this time can be changed by choosing a different capacitor value. A 0.2 Ω resistor is used in series with the MOSFET, and its voltage is used at pin 3 after a low pass filter to eliminate the high transient spikes caused by switching. This voltage is compared with a 1 V internal voltage, therefore, this value is adjusted for 5 A. Also, the value of this resistor can be

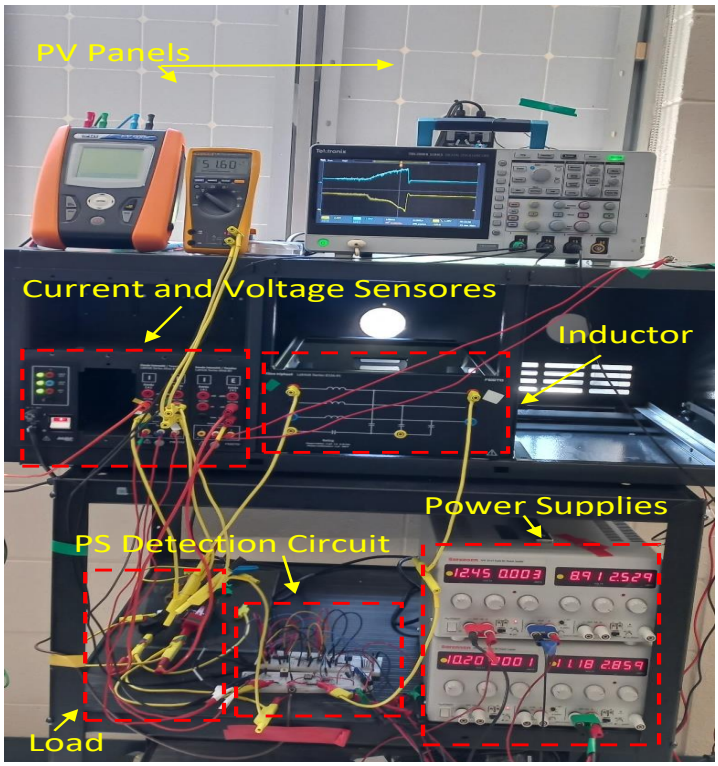

Figure 4.9: A setup for the proposed partial detection method.

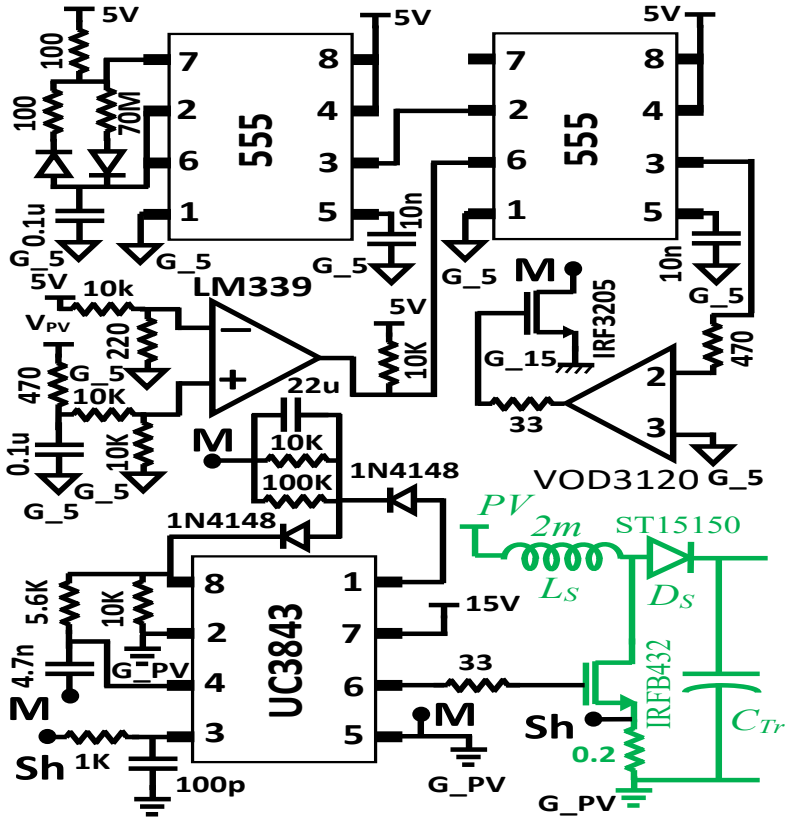

Figure 4.10: A controller for the proposed partial detection circuit.

adjusted based on the PV panel's maximum short-circuit current. The nominal current for these panels is around 5 A and it is almost proportional to the irradiation level, therefore, for irradiation between 200 $\frac{W}{m^2}$ and 1000 $\frac{W}{m^2}$, the operation current is between 1 A and 5 A. In addition, the operating voltage is considered as $0.8 \times V_{OC}$ and V_{OC} is regarded as the nominal open-circuit voltage which is equal to 45 V (22.5 V for each PV panel). C_{Tr} is 1000 uF, therefore, T_{DE} is 1.8 $msec$ according to (4.8). As it was explained, this value is based on the assumption that the PV current changes during T_{DE} for the maximum load (Fig. 4.6), while as it is shown in Fig. 4.7, this value for the maximum load changes during a small duration (T_1). Therefore, in this design, T_{DE} is regarded as 30 $msec$. The second important parameter to design the PS detection method is the minimum value of L_S to work in CCM based on (4.11) which is equal to 450 uH for f_{sw} equal to 50 kHz. This value is chosen as 1 mH to decrease the switching ripples.

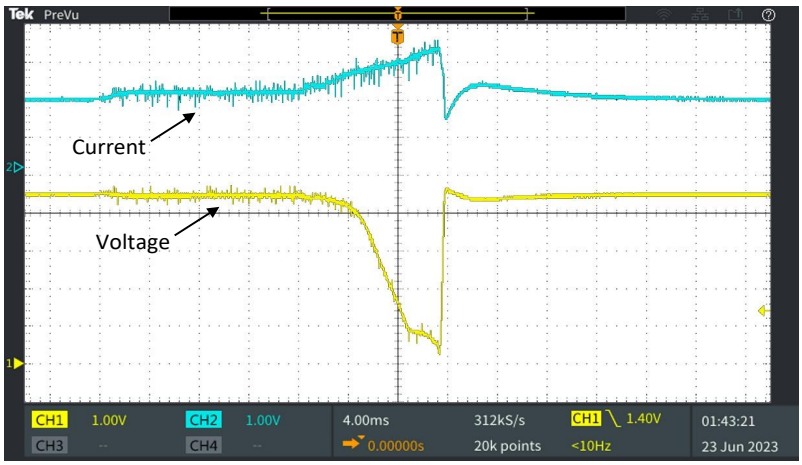

Figure 4.11: Current and voltage of the PV panels with one module in the first scenario.

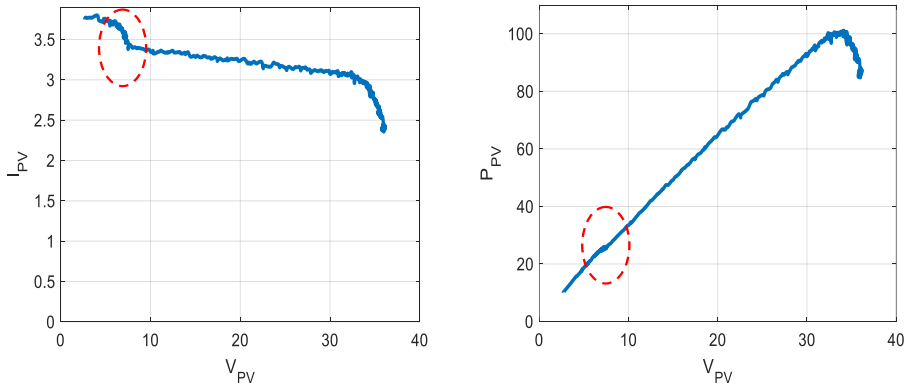

Figure 4.12: Detected current and power versus voltage of the PV panels in the first scenario.

Three scenarios are taken into account to investigate the performance of the proposed PS detection method. In the first one, three PV modules are in the low-rate PS condition. The aim of this scenario is to evaluate the operation of the proposed method to detect the PS condition at a low-rate PS condition and at a lower voltage. Fig. 4.11 shows the voltage and current waveforms for this condition. As seen, there is one step that shows one PV module has a different shading rate. Fig. 4.12 shows the PV current and power versus the PV voltage, respectively. As seen, the PS condition can be recognized easily from these figures.

In the second scenario, the performance of the proposed method is investigated by applying a high shading rate on some PV cells of one PV module to mimic the PS

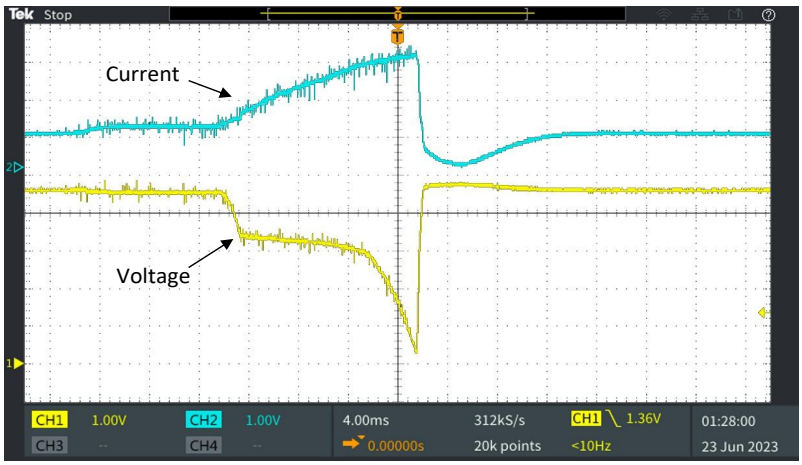

Figure 4.13: Current and voltage of the PV panels with one module in the second scenario.

condition on this PV panel. This scenario aims to evaluate the PS detection accuracy in higher voltages. Fig. 4.13 exhibits the voltage and current waveforms for this case. To show the occurrence of the PS condition better, Fig. 4.14 shows the PV current and the PV power versus the PV voltage for this case. From these two scenarios, it was proved that the PS can be detected easily no matter whether its rate is low or high or if it happens in low or high voltages.

For the third scenario, all four modules are in the PS condition with different rates. Fig. 4.15 exhibits the voltage and current waveforms for this case. Also, Fig. 4.16 shows the PV current and the PV power versus the PV voltage. As seen, there are three steps that indicate all three modules are in the PS condition. As it was explained, the design of the PS detection circuit was based on 10% voltage drop in the terminal capacitor. The voltage waveforms of the terminal voltage are shown in Fig. 4.17, Fig. 4.18 and Fig. 4.19 for the aforementioned scenarios. As seen, the terminal voltage drop is in the acceptable range.

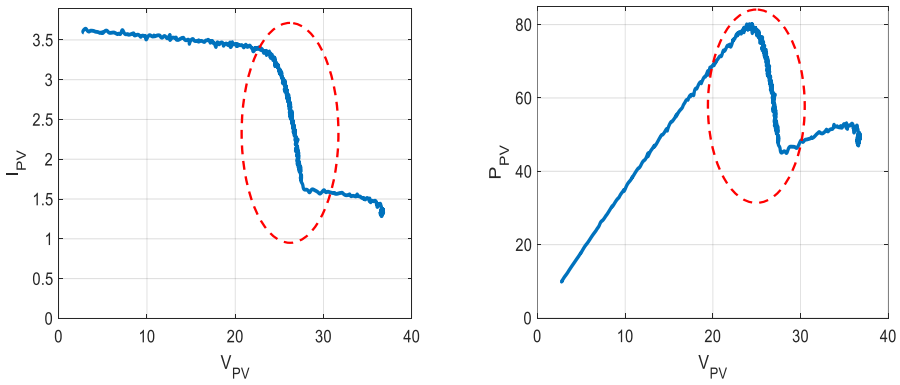

Figure 4.14: Detected current and power versus voltage of the PV panels in the second scenario.

Figure 4.15: Current and voltage of the PV panels with one module in the third scenario.

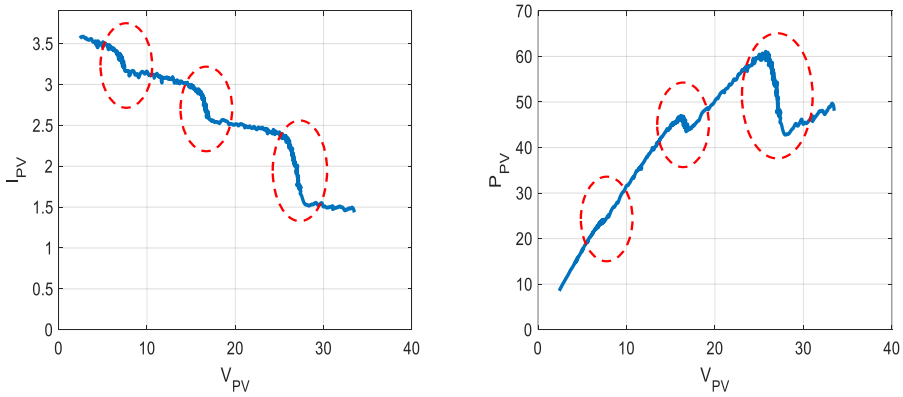

Figure 4.16: Detected current and power versus voltage of the PV panels in the third scenario.

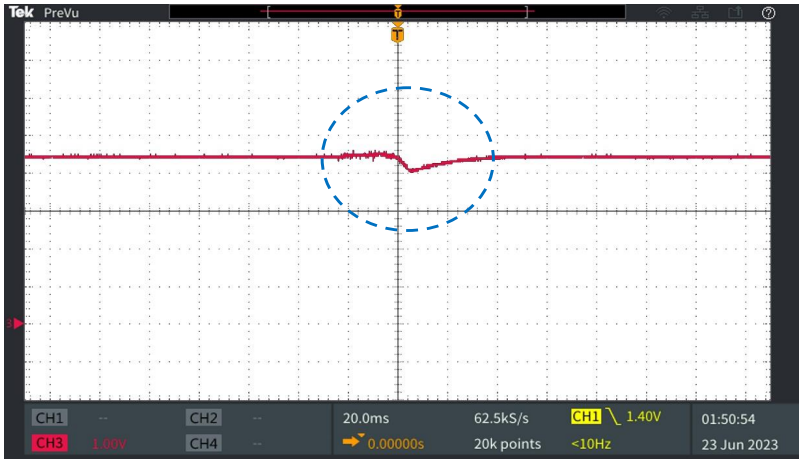

Figure 4.17: Terminal voltage in the first scenario.

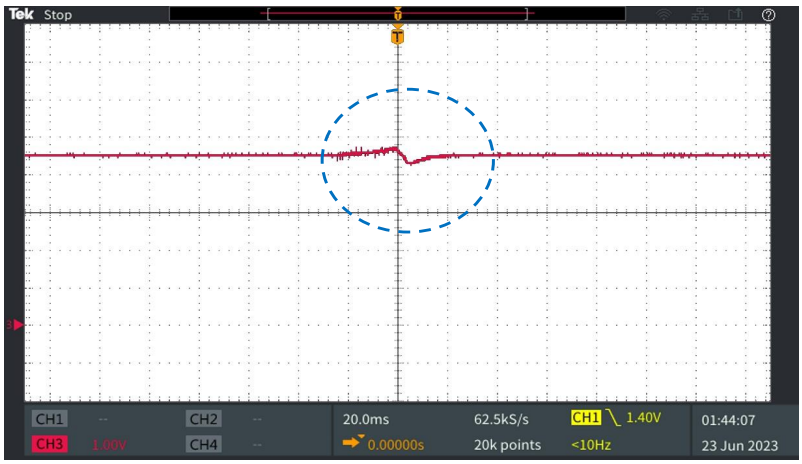

Figure 4.18: Terminal voltage in the second scenario.

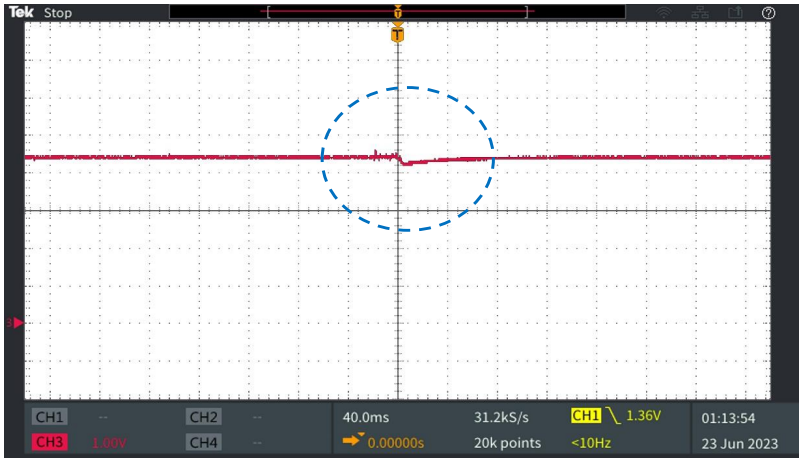

Figure 4.19: Terminal voltage in the third scenario.

Chapter 5

The Valley Switching Based Boost Power Optimizer for Wide Input Voltage Ranges

5.1 Introduction

In this chapter, the loss analyses of the conventional boost power optimizer are presented. Then, the effects of employing the resonance and valley switching control are studied to investigate their effectiveness in PS conditions. The main sources of losses such as the switching and conduction losses of the MOSFET, the cupper loss of the inductor and the conducting loss of the diode are regarded. It is shown that if the boost power optimizer is designed to use the valley switching control in the PS conditions, the resonance does not have a significant effect in decreasing the losses in the non-shading conditions. To solve this problem, a new boost power optimizer is introduced to employ the valley switching control in wide input voltage ranges. Also, it is shown that all losses are lower than their equivalent value in the proposed converter leading to higher efficiency. Finally, a prototype converter is designed and tested in different input voltage values to verify the effectiveness of the new converter. The experimental results supported the analyses and show the efficiency of the new converter is as high as 98%.

5.2 Losses Analyses of the Traditional Boost Power Optimizer Under Valley Switching Control

Two resonances occur in traditional boost power optimizers (Fig. 2.4). The first one happens when the inductor current reaches the reference maximum current and the MOSFET turns off. The second one is when the diode current becomes zero and it turns off. They are shown in (5.1) and (5.2), respectively. These equations are achieved by supposing constant input and output voltages, and zero resistance of elements such as the converter inductor and equivalent series resistance of the capacitors.

$$\begin{gathered} v_M(t) = V_{in} - V_{in}\cos(\omega_C t) + I_{\max}\sqrt{L}\sin(\omega_C t) \\ , \quad \omega_C = \frac{1}{\sqrt{L\left(C_{oss} + C_D\right)}} \end{gathered} \tag{5.1}$$

$$v_M(t) = V_{in} + (V_o - V_{in})\cos(\omega_C t) \tag{5.2}$$

$$V_{M\min} = 2V_{in} - V_o \tag{5.3}$$

where V_{in}, V_o, v_M, L, C_D, and C_{oss} are the input, the output and the MOSFET voltages, the converter inductor, the diode, and the MOSFET output capacitances, respectively. Also, V_{Mmin} is the minimum point of the MOSFET output voltage oscillations, and as seen in (5.3), it tends to be negative when the output voltage value (V_o) is greater than $2V_{in}$. In this condition, the body diode (D_M) of the MOSFET turns on and clamps the voltage to zero. Fig. 5.1 shows the MOSFET output voltage and the converter inductor current in the current control and the valley switching mode. Supposing working in critical conduction mode and little resonance time (T_r), the average input current (I_{SAve}), the diode current (I_{DAve}), RMS current of converter inductor (I_{Lrms}) and the MOSFET are:

$$I_{DAve} = \frac{I_{\max}}{2}(1 - D) \tag{5.4}$$

$$I_{SAve} = \frac{I_{\max}}{2} \tag{5.5}$$

$$I_{Lrms} = \frac{I_{\max}}{\sqrt{3}} \tag{5.6}$$

$$I_{Mrms} = I_{\max}\sqrt{\frac{D}{3}} \tag{5.7}$$

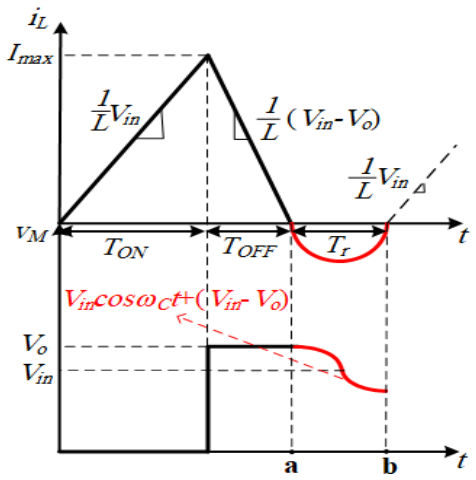

Figure 5.1: Inductance current and the MOSFET output voltage for the conventional boost power optimizer.

where I_{max} and D are the maximum reference current, and converter duty cycle, respectively. Power losses of the converter inductor (P_{LCon}), diode (P_{DCon}), conducting losses of the MOSFET (P_{CoCon}) and its ON/OFF state switching losses ($P_{SwConOn}$ and $P_{SwConOff}$) can be calculated using these values.

$$P_{LCon} = R_S \frac{I_{\max}^2}{3} \tag{5.8}$$

$$P_{DCon} = \frac{V_F I_{\max}}{2}(1-D) \tag{5.9}$$

$$P_{CoCon} = R_{on} \frac{I_{\max}^2}{3} D \tag{5.10}$$

$$P_{SwConOff} = \frac{f_{sw}}{2} I_{\max} V_o t_{OFF} \tag{5.11}$$

$$P_{SwConOn} = \frac{f_{sw}}{2} C_{oss} (V_o - 2V_{in})^2 \tag{5.12}$$

$$f_{sw} = \frac{V_{in}(V_o - V_{in})}{L I_{max} V_o} \tag{5.13}$$

where V_F, R_{on} and t_{OFF} are the diode forward voltage, inductor winding resistance, and turn-off time of the MOSFET, respectively. Equation (5.12) indicates that if the input voltage is more than half of the output voltage, the switching losses are not zero. This condition occurs when the non-shading condition exists and the voltage of GMPP is

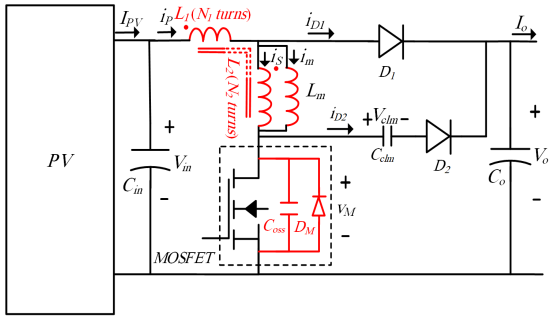

Figure 5.2: Proposed boost power optimizer.

close to the output voltage value. These losses are important from another viewpoint because the system usually works in non-shading conditions, therefore, the efficiency of the system decreases significantly. Regarding this fact, using resonance is not helpful to decrease the boost power optimizer losses, consequently, a new topology should be introduced to take advantage of the resonance and increase the converter efficiency.

5.3 Proposed Converter

As shown in Fig. 5.2, a converter is proposed in this research aiming at reducing the switching and conduction losses of the MOSFET, the ohmic losses of the inductor, the diode and input bridge losses due to forward voltage drop. The inductor winding is divided into two windings ($N = N_1 + N_2$) that are wound on the same core to produce coupled inductors. Therefore, the size and the cost of the proposed converter remain unchanged in comparison to the conventional converter. The first winding (N_1) is placed in the conventional inductor location and the other one (N_2) is added to the MOSFET branch. Also, an auxiliary capacitor (C_{clm}) and an additional diode (D_2) are used to clamp the second inductor voltage such that only the first winding (N_1) conducts the falling magnetizing current when the MOSFET turns off. The three main operation states of the proposed converter are explained as follows:

State 1) MOSFET ON: This case is illustrated in Fig. 5.3. The diode output capacitance is not considered because it has a much lower value in comparison to the MOSFET output capacitance and it does not affect the operation of the converter predominantly. Supposing constant input voltage, the magnetizing current (i_m) and the primary current

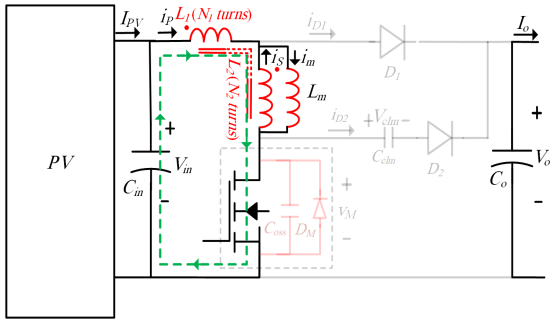

Figure 5.3: Proposed converter when the MOSFET turns on.

of the coupled inductance (i_p) can be written as:

$$i_m(t) = \frac{1}{L_m}\frac{N_2}{N_1+N_2}V_{in}t \tag{5.14}$$

$$i_p(t) = \frac{1}{L_m}\left(\frac{N_2}{N_1+N_2}\right)^2 V_{in}t \tag{5.15}$$

State 2) MOSFET OFF: When the MOSFET current, which is the same as the primary current, reaches the maximum reference current (I_{max}), it turns off and a resonance occurs between the diodes and the MOSFET output capacitance and inductors. Both diodes (D_1 and D_2) conduct when their capacitance voltage becomes positive. The diode D_2 turns off when the secondary leakage energy discharges to the capacitor C_{clm} and the magnetizing current flows to the output capacitance (C_o) through the primary diode (D_1). The reason is that when the converter starts working, the capacitor C_{clm} is charged through inductance L_2 and its voltage goes up till its equivalent series resistance energy dissipation becomes equal to the secondary leakage inductance energy in steady state condition. At this moment, the magnetizing energy discharges through the primary winding and diode D_1 to the output capacitor. Consequently, the magnetizing current falls to zero. The equivalent circuit in this state is shown in Fig. 5.4. In this state, the magnetizing current (i_m) and the primary current of the coupled inductance (i_p) can be written as:

$$i_m(t) = I_{\max} - \frac{N_2}{N_1}\frac{1}{L_m}\left(V_o - V_{in}\right)t \tag{5.16}$$

$$i_p(t) = \frac{N_2}{N_1}I_{\max} - \left(\frac{N_2}{N_1}\right)^2\frac{1}{L_m}\left(V_o - V_{in}\right)t \tag{5.17}$$

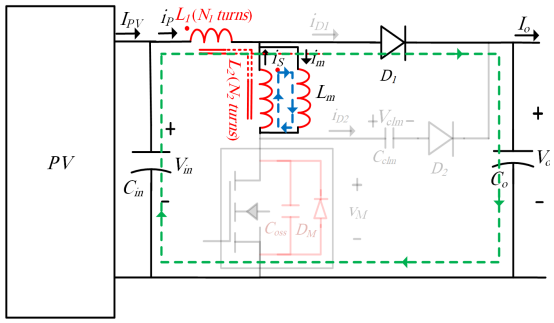

Figure 5.4: Proposed converter when the MOSFET turns off.

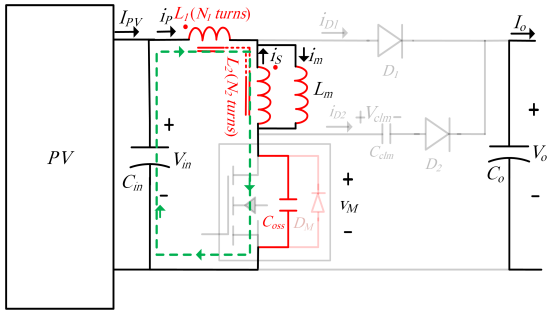

Figure 5.5: Proposed converter when the current reaches zero.

State 3) Zero primary winding current: When the primary winding current reaches zero, another resonance occurs between the MOSFET output capacitance and inductors. Fig. 5.5 exhibits the equivalent circuit in this state. The initial and oscillating voltage equations of the MOSFET capacitance are:

$$v_M(0) = V_{in} - \frac{N_1 + N_2}{N_1}(V_{in} - V_o) \tag{5.18}$$

$$v_M(t) = V_{in} + \frac{N_1 + N_2}{N_1}(V_o - V_{in})\cos(\omega_N t) \quad , \quad \omega_N = \frac{N_1 + N_2}{N_2\sqrt{L_m C_{oss}}} \tag{5.19}$$

$$V_{M\,\min} = 2V_{in} - V_o - \left(\frac{N_2}{N_1}\right)(V_o - V_{in}) \tag{5.20}$$

Comparing the value of V_{Mmin} obtained in the conventional converter in (5.3) with the one driven in the proposed converter in (5.20) highlights that a considerable reduction

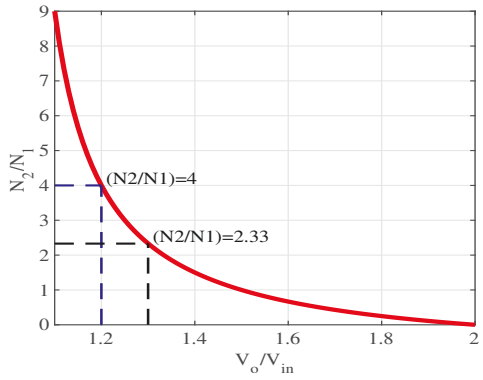

Figure 5.6: Winding radio as a function of voltage ratio.

in the minimum output voltage across the MOSFET achieved in the proposed converter. As a result, the ON state switching losses of the proposed converter decrease. However, the optimal condition is when the MOSFET minimum voltage becomes zero. To this end, the primary and secondary winding turn ratios can be adjusted to decrease the MOSFET minimum voltage to zero as shown in (5.21).

$$\frac{N_2}{N_1} = \frac{2 - \dfrac{V_o}{V_{in}}}{\dfrac{V_o}{V_{in}} - 1} \tag{5.21}$$

Fig. 5.6 shows the winding turn ratio as a function of the output to the input voltage ratio. As seen, having zero minimum output voltage requires a high winding ratio for a low voltage ratio. On the other hand, a higher winding ratio causes a higher peak primary winding current as shown in (5.17), which increases the converter diode current rating and requires larger input and output capacitors. Consequently, having a winding turn ratio around 4 or 2.33 which is achieved for 1.2 and 1.3 voltage ratio, respectively is sufficient. This voltage ratio is sufficient for boosting the PV panel voltage in the normal condition that the voltage at GMPP is around $0.8 \times V_{OC}$.

Fig. 5.7 shows the theoretical MOSFET output voltage and the primary winding theoretical current waveform. The input average current (I_{SAvePr}), the average current of the diode D_1 ($I_{D1AvePr}$), the primary and secondary winding RMS current (I_{PrmsPr} and I_{SrmsPr}), and the MOSFET RMS current (I_{MrmsPr}) can be calculated based on this waveform and supposing negligible resonant time.

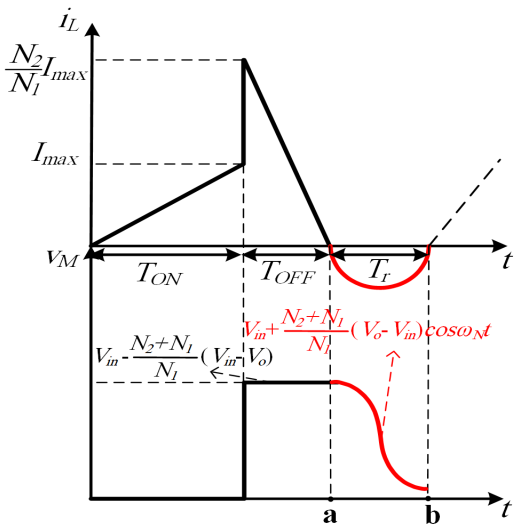

Figure 5.7: Proposed converter primary winding current and the MOSFET output voltage.

$$I_{D1AvePr} = \frac{N_2}{N_1}\frac{I_{\max Pr}}{2}(1 - D_{Pr}) \tag{5.22}$$

$$I_{SAvePr} = \frac{I_{\max Pr}}{2}\left(D_{Pr} + \frac{N_2}{N_1}(1 - D_{Pr})\right) \tag{5.23}$$

$$I_{PrmsPr} = \frac{I_{\max Pr}}{\sqrt{3}}\sqrt{D_{Pr} + \left(\frac{N_2}{N_1}\right)^2(1 - D_{Pr})} \tag{5.24}$$

$$I_{SrmsPr} = I_{\max Pr}\sqrt{\frac{D_{Pr}}{3}} \tag{5.25}$$

$$I_{MrmsPr} = I_{\max Pr}\sqrt{\frac{D_{Pr}}{3}} \tag{5.26}$$

where $I_{\max Pr}$, and D_{Pr} are the reference maximum current and the duty cycle of the proposed converter, respectively. The steady-state output voltage can be achieved using the volt-second balance of the converter inductor for both conventional and proposed converters. This value is shown in (5.27) for the proposed converter, and in (5.28) for the conventional converter.

$$V_o = \frac{N_1 + (N_2(1 - D_{Pr}))}{N_1 + N_2}\frac{1}{(1 - D_{Pr})}V_{in} \tag{5.27}$$

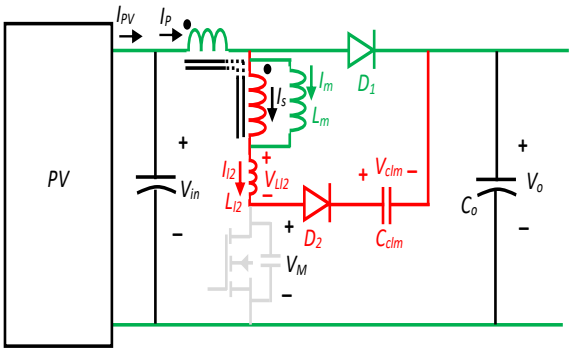

Figure 5.8: The secondary leakage inductance effect (the green and red elements show the magnetizing and secondary leakage currents path, respectively.

$$V_o = \frac{1}{(1-D)} V_{in} \tag{5.28}$$

Equations (5.27) and (5.28) can be used to calculate the relation between the duty cycle of the conventional and the proposed converter to have equal output voltage. Equation (5.29) shows this relation.

$$D = \frac{N_1 D_{Pr}}{N_1 + N_2 (1 - D_{Pr})} \tag{5.29}$$

The secondary winding leakage inductance changes the current shape when the input voltage is low. However it does not have any effect on the voltage drop across the MOSFET; therefore, the minimum resonant voltage does not change. Fig. 5.8 and Fig. 5.9 illustrate the effect of the secondary leakage inductance when the MOSFET turns off. Both diodes D_1 and D_2 turn on at this moment. While D_1 carries the primary current (i_P) to discharge the stored energy in the magnetizing inductance, the diode D_2 provides a path to discharge the stored energy in the secondary leakage inductance to the capacitor C_{clm}. The voltage drop across the primary windings is $V_{in} - V_o$, therefore, the voltage across the secondary windings is $\frac{N_2}{N_1}(V_{in} - V_o)$. When the input voltage is a low value, the secondary voltage is a high value because the output voltage is constant. Therefore, the voltage drop across the secondary leakage inductance is low and the required time to decrease the leakage inductance current to zero is long which changes the shape of the primary current as seen in Fig. 5.9.

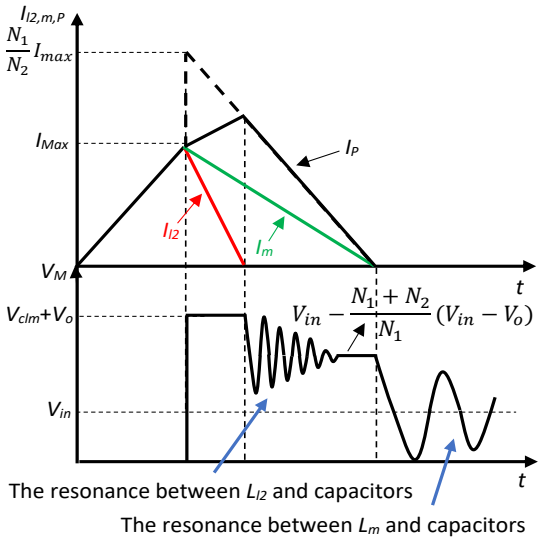

Figure 5.9: The leakage inductance effect on the primary current and the MOSFET output voltage waveforms (red: leakage inductance current, green: magnetizing current).

5.4 Loss analysis of the proposed and conventional converters

Although the main objective of the proposed converter topology is decreasing the switching losses, the other power losses such as the inductor, diode, and MOSFET conduction losses decrease effectively resulting in a highly efficient power optimizer converter. In order to compare the performance of the proposed converter with the conventional one, the average input current, which is the same as the photovoltaic cell output current, should be kept equal. The equalization of (5.5) and (5.23) yields the following relationship between the maximum current reference of proposed and conventional converters.

$$I_{\max Pr} = \frac{1}{\left(D_{Pr} + \frac{N_2}{N_1}(1 - D_{Pr})\right)} I_{\max} \tag{5.30}$$

5.4.1 The MOSFET switching losses

The switching losses of the proposed converter (P_{SwPr}) are divided into two parts including ON-state switching (P_{SwPrOn}) and OFF-state switching ($P_{SwPrOff}$). The OFF-state switching loss is related to a time interval when the MOSFET current reaches the

reference maximum current and the ON-state switching happens when the MOSFET turns on in the minimum point of the resonant voltage in the valley switching mode as follows.

$$P_{SwPrOff} = \frac{f_{swPr}}{2} I_{\max Pr} \left(V_{in} - (1+n)(V_{in} - V_o)\right) t_{OFF} \tag{5.31}$$

$$P_{SwPrOn} = \frac{f_{swPr}}{2} C_{oss} \left(2V_{in} - V_o - \left(\frac{N_2}{N_1}\right)(V_o - V_{in})\right)^2 \tag{5.32}$$

It can be seen that the switching losses are decreased in the proposed converter. It is worth mentioning that the switching frequency of the proposed converter in (5.33) is different from the switching frequency of the conventional one which is shown in (5.13).

$$f_{swPr} = \frac{(n+1)\, V_{in}\, (V_o - V_{in})}{L I_{\max Pr} \left((n+1)\, (V_o - V_{in}) + V_{in}\right)} \tag{5.33}$$

5.4.2 The MOSFET Conduction Loss

The conduction loss of the MOSFET can be calculated as follows:

$$P_{CoPr} = R_{on} \frac{I_{\max pr^2}}{3} D_{Pr} \tag{5.34}$$

Equation (5.30) should be satisfied to compare the conduction loss of the MOSFET for the conventional and the proposed converters, which are shown in (5.10), and (5.34), respectively. Equation (5.35) shows the relation between the MOSFET conduction loss in the proposed and conventional converter.

$$\begin{aligned} P_{CoPr} &= Coeff_M \times P_{CoCon} \\ Coeff_M &= \frac{D_{Pr}}{\left(D_{Pr} + \frac{N_2}{N_1}(1 - D_{Pr})\right)^2} \frac{1}{D} \end{aligned} \tag{5.35}$$

where the duty cycle of the conventional converter (D) can be replaced by (5.29).

$$Coeff_M = \frac{N_1 + N_2\,(1 - D_{Pr})}{N_1 \left(D_{Pr} + \frac{N_2}{N_1}(1 - D_{Pr})\right)^2} \tag{5.36}$$

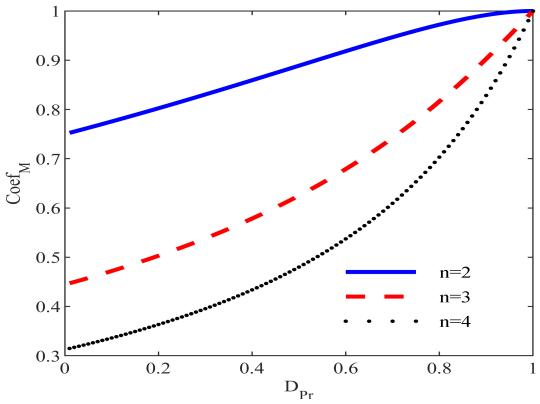

Figure 5.10: Coefficient $Coeff_M$ as a function of duty cycle.

Fig. 5.10 shows $Coeff_M$ as a function of the duty cycle for different winding turn ratios. As can be seen, this coefficient is less than one for all duty cycle ranges which indicates a lower MOSFET conduction loss rather than the conventional converter.

5.4.3 The Inductor conduction Losses

The primary and secondary resistances (R_{pri} and R_{sec}) depend on the winding turn ratio and total winding resistance.

$$R_{pri} = \frac{N_1}{N_1 + N_2} R_S \tag{5.37}$$

$$R_{sec} = \frac{N_2}{N_1 + N_2} R_S \tag{5.38}$$

Their conduction losses can be calculated using the RMS value of the primary and the secondary winding currents, which are shown in (5.24) and (5.25), respectively.

$$P_{pri} = R_{pri} \frac{I^2_{\max pr}}{3} \left(D_{Pr} + \left(\frac{N_2}{N_1} \right)^2 (1 - D_{Pr}) \right) \tag{5.39}$$

$$P_{\text{sec}} = R_{\text{sec}} \frac{I^2_{\max pr}}{3} D_{pr} \tag{5.40}$$

The inductor power loss of the proposed converter is the sum of these two winding losses as follows:

$$P_{LPr} = R_S \frac{I^2_{\max pr}}{3} \left(D_{Pr} + \frac{N_2^2}{N_1 (N_1 + N_2)} (1 - D_{Pr}) \right) \tag{5.41}$$

The proposed converter inductor power loss can be calculated as a function of the conventional converter power loss using (5.12), (5.30), and (5.41).

$$\begin{aligned} P_{LPr} &= Coeff_L P_{LCon} \\ Coeff_L &= \frac{(N_1^2 D_{Pr} + N_2^2 (1 - D_{Pr}) + N_1 N_2 D_{Pr})}{(N_1^2 D_{Pr} + N_2^2 (1 - D_{Pr}) + N_1 N_2)} \end{aligned} \tag{5.42}$$

Fig. 5.11 shows the coefficient $Coeff_L$ as a function of the duty cycle for different winding's turn ratio that is less than one for all duty cycle range, indicating the inductor power loss is always lower in the proposed topology.

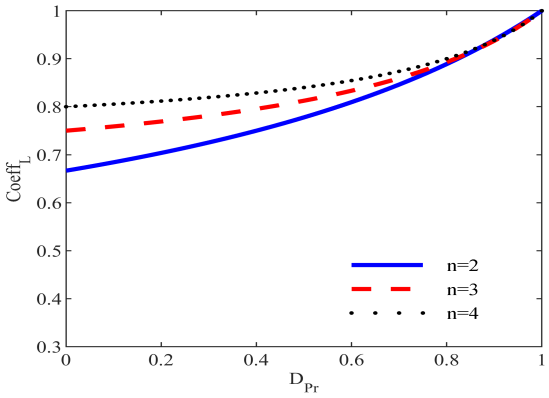

Figure 5.11: Coefficient $Coeff_L$ as a function of duty cycle.

5.4.4 The diode conduction power loss

Diode conduction power loss can be calculated using the average current of diode D_1 supposing negligible secondary winding leakage current. Its average current is shown in (5.22) and the diode conduction power loss is shown in (5.43).

$$P_{DPr} = \frac{N_2}{N_1} \frac{I_{\max Pr}}{2} V_F (1 - D_{Pr}) \tag{5.43}$$

This loss can be written as a function of the conventional converter diode conduction loss using (5.9), (5.29), (5.30), and (5.43).

$$\begin{aligned} P_{DPr} &= Coeff_D P_{DCon} \\ Coeff_D &= \frac{N_2 (1 - D_{Pr})}{N_1 D_{Pr} + N_2 (1 - D_{Pr})} \times \frac{N_1 + N_2 (1 - D_{Pr})}{N_1 (1 - D_{Pr}) + N_2 (1 - D_{Pr})} \end{aligned} \tag{5.44}$$

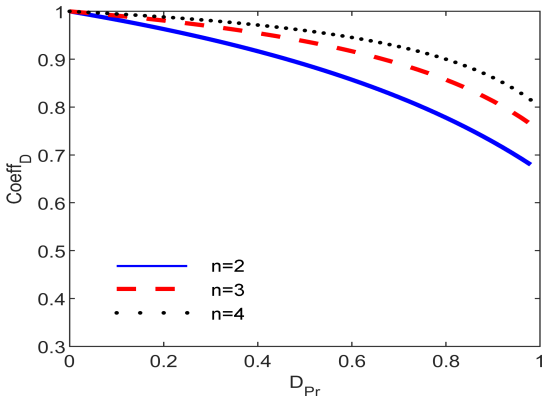

Figure 5.12: Coefficient $Coeff_D$ as a function of duty cycle.

Fig. 5.12 shows coefficient $Coeff_D$ as a function of the duty cycle for different winding turn ratios. As seen in this figure, $Coeff_D$ is less than one which means the diode conduction loss is a lower value in the proposed converter.

5.5 Experimental Verification

Fig. 5.13 and Fig. 5.14 show a prototype and its control circuit for the proposed boost power optimizer, respectively. $IRF640$ MOSFET and $APT100S20BG$ diodes are used in this prototype and the other elements are shown in Table 5.1. The current controller and the zero voltage switching circuits are designed to implement the valley switching operation. In addition, working in the DCM is possible. This operation is useful to compare the output voltage oscillations of the MOSFET in the conventional and proposed converters. To do this, the jumper $J3$ is disconnected to disable the valley switching controller then the MOSFET gate pulse is applied by a pulse generator implemented by a 555 timer IC shown in Fig. 5.13. Also, jumpers $J1$ and $J2$ are employed to change the configuration as the conventional or proposed converter ($J1$ is open and $J2$ is closed for the conventional converter configuration and $J1$ is closed and $J2$ is open for the proposed converter configuration). To highlight the effectiveness of the proposed topology in reducing the losses, the output voltage is set to $48V$ and two scenarios were considered during the tests as follows:

Scenario 1) Low output to input voltage ratio: Fig. 5.15 and Fig. 5.16 show the input current of the primary winding and the output voltage of the MOSFET in the DCM mode for the proposed and conventional boost power optimizer when the input voltage

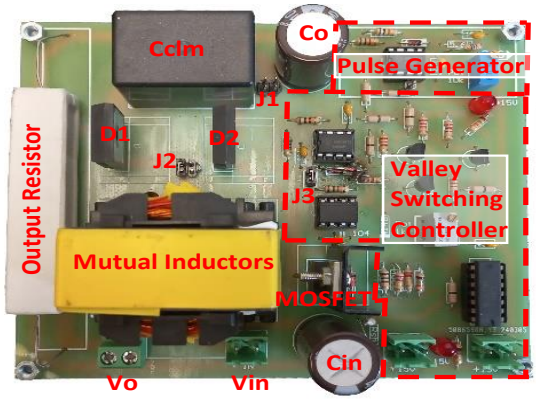

Figure 5.13: Prototype of the proposed boost power optimizer.

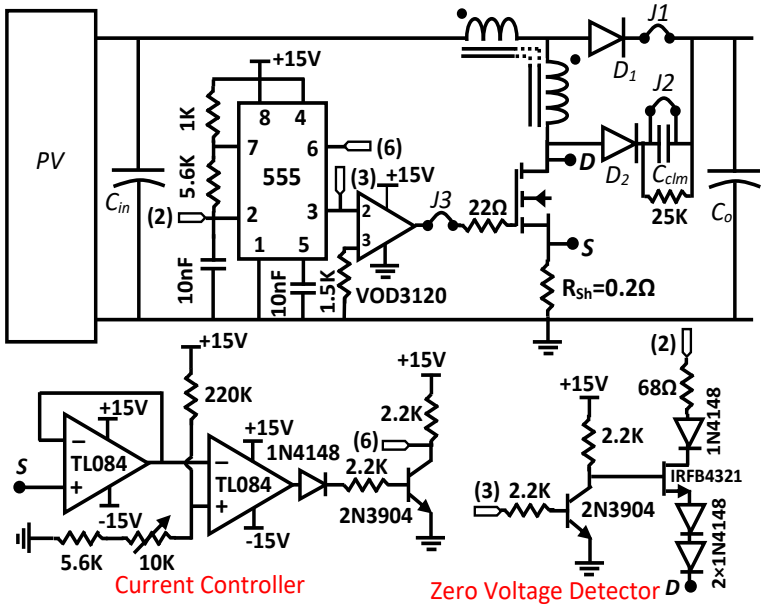

Figure 5.14: Control circuit of the proposed boost power optimizer.

Table 5.1: System specifications for resonance boost power optimizer verification

Parameter	Description	Value/Part number
C_o	Output capacitor	$470uF, 100V$
C_{in}	Input capacitor	$470uF, 100V$
C_{clm}	Auxiliary capacitor	$3uF, 350V$
R_g	The MOSFET gate resistor	$33\Omega, 0.25W$
R_{cs}	Current feedback resistor	$0.2\Omega, 10W$
L	Inductance	$266uH$
N_1	Primary winding turns	5
N_2	Secondary winding turns	20

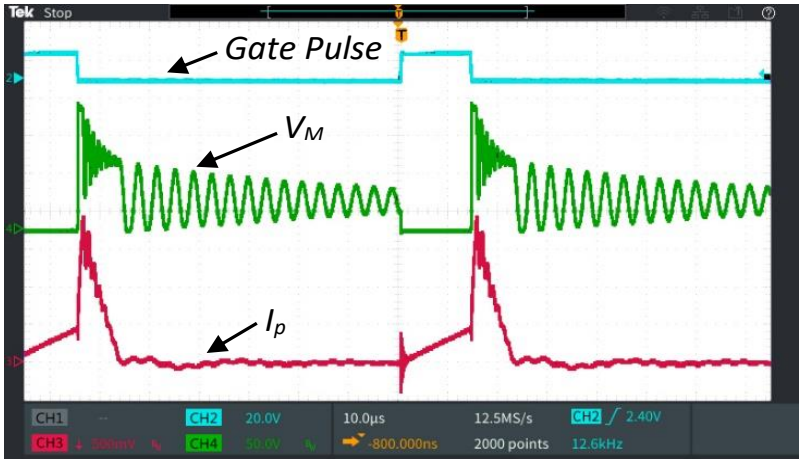

Figure 5.15: The primary winding' current and the MOSFET output voltage for the proposed boost power optimizer in DCM mode and $V_{in} = 40V$.

is $40V$. In this condition, the voltage ratio is 1.2, therefore, the required winding turn ratio to have zero minimum voltage in the proposed boost power optimizer is around 4 according to (5.21). As seen, the minimum point of the MOSFET output voltage is zero for the proposed boost power optimizer. Consequently, if the valley switching mode is activated for the proposed boost power optimizer, the ON-state switching loss will be zero. On the contrary, the minimum point of the MOSFET output voltage is $32V$ for the conventional converter; therefore, if the ON switching of the MOSFET occurs at this point, the ON-state switching loss of the conventional converter is high compared to the proposed converter.

Scenario 2) High output to input voltage ratio: Fig. 5.17 and Fig. 5.18 show the input current of the primary winding and the output voltage of the MOSFET in the DCM

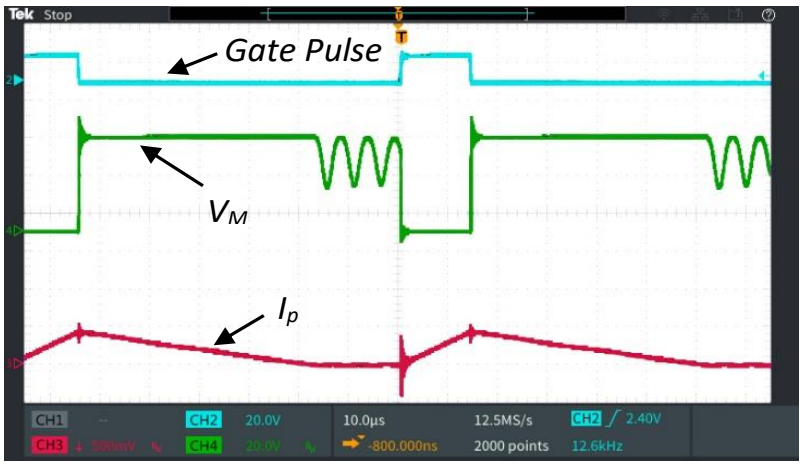

Figure 5.16: The primary winding' current and the MOSFET output voltage for the conventional boost power optimizer in DCM mode and $V_{in} = 40V$.

mode for the proposed and conventional boost power optimizers when the input voltage is $20V$. According to (5.3), when the output voltage to the input voltage ratio increases in the conventional boost power optimizer, the minimum value of the MOSFET output voltage decreases. In this case, the minimum point is $-8V$, therefore, the body diode clamps it to zero. The minimum resonant voltage across the MOSFET in the proposed converter is also zero; therefore, when the voltage ratio is high, the valley switching has a significant effect in decreasing the switching losses in both converters.

In PS conditions, the GMPP voltage occurs in lower ranges, therefore, these conditions are in scenario 2. As explained above, both the conventional and proposal converters have zero resonant voltage across the MOSFET and the valley switching decreases their switching losses significantly. On the other hand, the PV voltage is close to the output voltage in non-shading conditions, consequently, they are in scenario 1, and applying the valley switching does not have a considerable effect in decreasing the switching losses of the conventional converter. While the minimum resonant voltage of the proposed converter becomes zero in these conditions and the valley switching can improve its efficiency considerably.

Fig. 5.19 shows the MOSFET output voltage, the primary winding and the input current for the proposed boost power optimizer when the valley switching mode is activated and the input voltage is $40V$. As seen, the ON-state switching of the MOSFET occurs at the minimum point of its voltage; therefore, the MOSFET output voltage does not oscillate. Also, the input current is smooth and does not have any significant

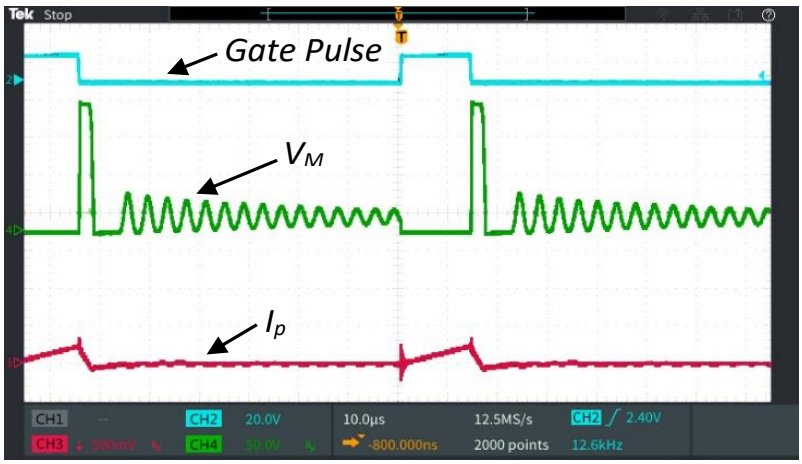

Figure 5.17: The primary winding' current and the MOSFET output voltage for the proposed boost power optimizer in DCM mode and $V_{in} = 20V$.

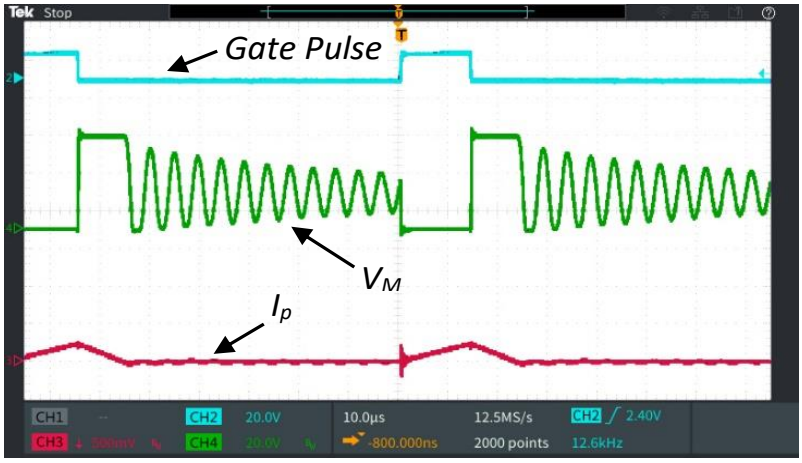

Figure 5.18: The primary winding' current and the MOSFET output voltage for the conventional boost power optimizer in DCM mode and $V_{in} = 20V$.

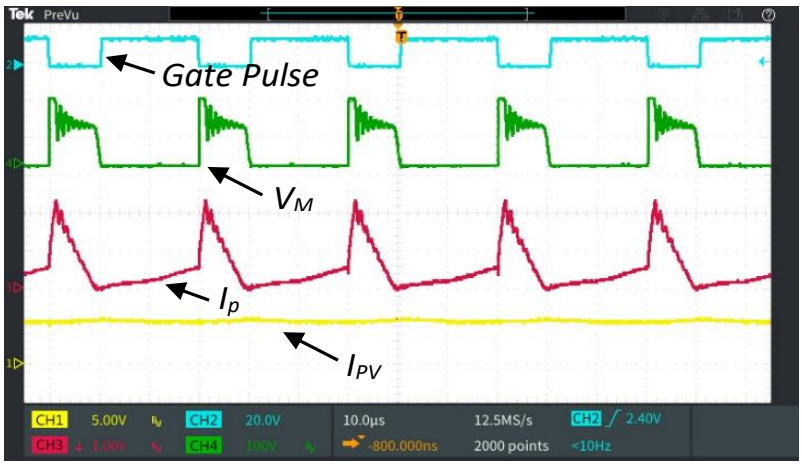

Figure 5.19: The MOSFET output voltage, the primary winding, input and output current for the proposed boost power optimizer in the valley switching mode, $V_{in} = 40V$, and $V_o = 48V$.

Table 5.2: The maximum reference current and the duty cycle of the proposed and conventional boost power optimizer to have equal input current ($V_o = 48V$, $I_{in} = 2.5A$, $N_1 = 5$, and $N_2 = 20$)

Parameter	$V_{in} = 40V$	$V_{in} = 20V$
D_{Pr}	0.50	0.88
D	0.17	0.58
I_{maxPr}	2.0A	3.68A
I_{max}	5A	5A
f_{sw}	5.0kHz	8.78kHz
f_{swPr}	37.59kHz	17.88kHz

ripples. The oscillations on the MOSFET voltage are because of the secondary leakage inductance effect as illustrated in Fig. 5.9 and Fig. 5.15 and do not have any impact on the operation of the valley switching mode.

Table 5.2 shows the duty cycle and the maximum reference current of the conventional and proposed boost power optimizers to have equal input current and output voltage. Two cases are considered for the input voltages. The valley switching mode is considered in the calculation of values for both converters. The maximum reference current and the duty cycle of the conventional and proposed converters are calculated using the input current and the input and output voltages (equations (5.5), and (5.28) for the conventional converter and (5.29) and (5.30) for proposed converter).

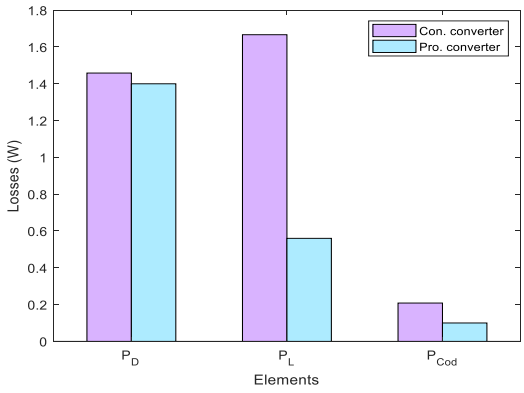

Figure 5.20: Losses of converter elements for $V_{in} = 40V$ (P_D: converter diodes losses, P_L: inductance losses, P_{Con}: MOSFET conduction losses.)

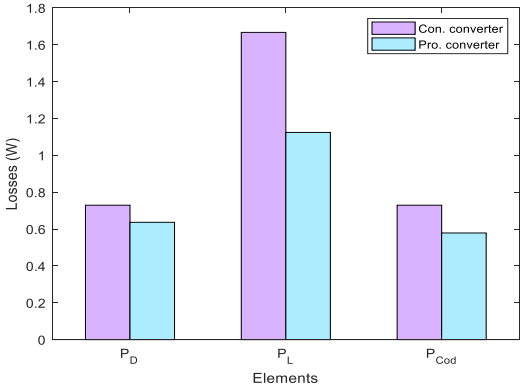

Figure 5.21: Losses of converter elements for $V_{in} = 20V$ (P_D: converter diodes losses, P_L: inductance losses, P_{Con}: MOSFET conduction losses.)

Fig. 5.20 and Fig. 5.21 show power losses for both the proposed and conventional converters for the input voltage equal to $40V$ and $20V$, respectively according to Table 5.2 and the equations presented in the previous sections. As can be seen, losses of all elements have been decreased using the proposed converter. Consequently, the proposed topology has a higher efficiency than the conventional converter as shown in Fig. 5.22. In order to further highlight the performance of the proposed topology, a comparison was also made with some converters in the literature in terms of the number of diodes, MOSFETs, passive elements, and efficiency at $V_{in} = 28V$ as shown in Table 5.3. Not only the proposed power optimizer proposes a higher efficiency and reliability in comparison with other available converters, but also it presents a cost-effective device since less components are used in its topology.

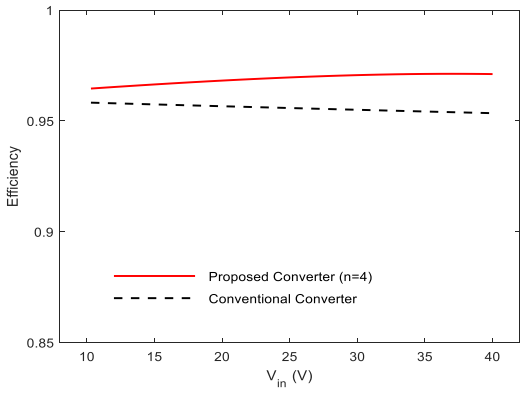

Figure 5.22: The proposed and conventional converter efficiency.

Table 5.3: Comparison between the proposed power optimizer and some similar references in view of circuit components and efficiency.

	[9]	[13]	[16]	Proposed Conv.
Diode	3	2	2	2
MOSFET	2	2	1	1
Resonance Capacitor	1	1	3	0
Magnetic Core	2	1	3	1
Efficiency	$< 92\%$	96%	$< 94\%$	98%

Chapter 6

Conclusions and Future Work

6.1 Concluding Remarks

Achieving highly efficient energy generation in a PV system under PS conditions is a well-known challenge. This is because the PV inverters in the market are not optimally designed to address an uneven solar irradiation on a PV panel surface, leading to a low or zero energy generation. To cope with this issue, this thesis aims to provide a PV generation system with sophisticated parts including an advanced MPPT algorithm, a novel PS detection mechanism, and an enhanced DC-DC power optimizer that can improve the efficiency of PV systems significantly. A sophisticated MPPT algorithm tracks the GMPP with minimum power fluctuations during tracking and steady state periods resulting in a significant decrease in energy losses. Every MPPT algorithm should be accompanied by a PS detection mechanism for its reinitialization otherwise the operating point gets stuck in an LMPP and energy losses increase. This detector is used in other applications such as power balancing converters as a trigger system or for PV cleaning scheduling, as a result, it should be independent of the MPPT algorithm. Apart from the PS mechanism, implementing the MPPT algorithm is important for an efficient PV generation system. The MPPT algorithm can be implemented directly by the inverter. The PV voltage provides the DC bus of the inverter using capacitors to reduce the voltage fluctuations. However, the voltage tracking range of an inverter is restricted due to its minimum DC bus value. A DC-DC boost converter can track the GMPP in low voltage values providing the ability to work in deep PS conditions. Some requirements should be addressed to employ these converters in PS conditions such as high voltage gain ratio and managing the converter losses. Utilizing the resonance is an

effective approach to increase the efficiency of the converter. However, its implementation requires adding more electrical components to the converter resulting in higher cost and complexity. The valley switching technique solves this problem by employing the resonance between the converter inductor and the intrinsic capacitance of the MOSFET. Operating in a wide input voltage range due to the operation in PS conditions is an obstacle to implementing this method. Consequently, a new topology should be used to employ this method effectively. These issues were addressed in this thesis and the following conclusions were drawn:

1. A possible comprehensive solution for solving the problems of the MPPT algorithms is an ANN model to estimate their initial duty cycles, leading to a reduction in the tracking time and power fluctuations. Additionally, this method effectively resolves the issue of getting stuck in an LMPP. In the proposed method, PS conditions are regarded as different shading patterns on the PV cells of a PV panel to calculate the GMPP voltage value accurately. Defining a dominant cell decreases the number of patterns; therefore, a precise dataset can be prepared. Moreover, measuring the shading rate on the PV modules electrically results in avoiding utilizing digital cameras or irradiation sensors. The PSO MPPT algorithm was chosen as the application for the proposed solution to prove its effectiveness in solving the problems of the MPPT techniques. Stability and steady-state analyses illustrate the necessity of such a solution. Also, the stability criteria reveal the origin of different issues in the operation of this MPPT algorithm. Finally, the combination of the proposed ANN model with the PSO algorithm improves the performance of the system as the experimental results prove the correctness of the analyses and validate the efficiency of the proposed MPPT algorithm. The experimental results indicate a 7% improvement in harvested energy employing this technique.

2. The analyses of the traditional scanning methods reveal their deficiencies in the MPPT application and a lack of a sophisticated scanning method. A novel converter was introduced in this thesis which does not require applying a short circuit at the terminal of the PV panel where an electrolytic capacitor is connected, thereby avoiding any detrimental effect on the lifetime of the system. The idea and the explanation of its performance highlight the flexibility of its implementations. Both the push-pull converter employing an isolated transformer and the full bridge converter accompanied by an inductor can be used to implement the

idea. The scanning method is performed in two phases. In the first phase, the RHS of the I-V or P-V curve is scanned then the LHS is scanned immediately. Each scan is done fast, therefore, it can be used as a replacement for the MPPT algorithm in a dynamic environment where the PV panel is installed on a moving object and the GMPP value changes fast in comparison to the usual condition. The experimental results show the voltage drop at the terminal is 9.5% and the scan is done in 6.5 ms.

3. As part of this thesis, different PS detection methods were investigated. It was demonstrated that the traditional methods are ineffective under certain conditions. The PS detection method based on a comparison of two generated power samples fails to detect the PS condition occurrence when it happens slowly. Also, the method based on measuring the voltage drop on the anti-parallel diode of the PV panel is influenced by the operating voltage of the system. In this thesis, the output characteristics of the PV panel are detected using a current pulse. The number of steps on the I-V curve reveals the number of PV modules with different shading values. Therefore, there is no PS condition in the system if there is not any step in its associated curves. Fast PS detection is another advantage of the proposed idea; consequently, it is ideal for different applications such as power-balancing converters. Also, the required circuit implementation is based on the wave-shaping converter resulting in a simple configuration. The experimental results in low, high, and a combination of PS conditions on the PV panels prove the effectiveness of the circuit, with the terminal voltage drop being less than 10% for the worst case.

4. Finally, the proposed boost power optimizer takes advantage of self-resonance caused by the converter inductor and the intrinsic capacitance of the MOSFET. The analyses illustrate that if the traditional converter is solely designed to exploit the resonance in the low voltage value caused by the PS conditions, the reduction in losses is not significant in the non-shading condition because in this situation the minimum resonance voltage of the MOSFET is not low enough. Coupled inductors are employed in the proposed converter to address this issue which decreases the minimum value of the MOSFET voltage to zero, leading to minimum switching losses. In addition, the other losses such as the conducting losses of the MOSFET, inductor, and diode are reduced effectively, resulting in an increase in the

efficiency of the converter in a wide input voltage range. The experimental results demonstrate that the converter achieves an efficiency of 98% while it tracks the GMPP successfully in low voltage ranges.

6.2 Research Perspectives

Based on the research work in this thesis, several recommendations for future studies are presented here:

- The proposed ANN-based MPPT technique is designed for DC/DC power optimizer. Additional research could be performed on the grid-connected or grid-forming inverter controller which is a promising research subject.
- The effect of the grid-connected inverter features such as low voltage ride through, supporting the weak grid, and power sharing in the parallel configuration on the MPPT procedure, especially in PS conditions should be investigated.
- Implementing the fast I-V scanning method directly by the inverter is essential to decrease the final price of the system and extend tracking the GMPP in the PS conditions.
- An artificial intelligence model could be employed to categorize the deficiencies of the PV system by analyzing the acquired I-V curve of the PV panel.
- A new topology could be used to implement the proposed PS-detecting idea as a PS detector and an MPPT converter simultaneously.
- Implementing the PS detector directly by the inverter is promising for PV panel maintenance scheduling which is an interesting research subject.
- Adding the high voltage ratio to the proposed boost power optimizer is recommended to employ the resonance in these types of power optimizers.
- The effect of using the resonance-based power optimizer on the size of filters especially the EMI filter can be promising.

Appendix A

Initial Point Estimator Using Linear Regression

The relation between the temperature, irradiation, depth of shading, and the GMPP voltage values is highly nonlinear; therefore, an ANN model is a better choice compared to other regression methods. To prove this fact, a comparison is made between an ANN and a linear regression model. The number of data is 1050, of which 20% data is chosen randomly for testing and 80% data is chosen for training the model. Fig. A.1 and Fig. A.2 show the result for both test and training data. As seen the ANN model estimates the function better than the linear model. The RMS error of the ANN model is 0.77 while this value is 3.3 for the linear regression.

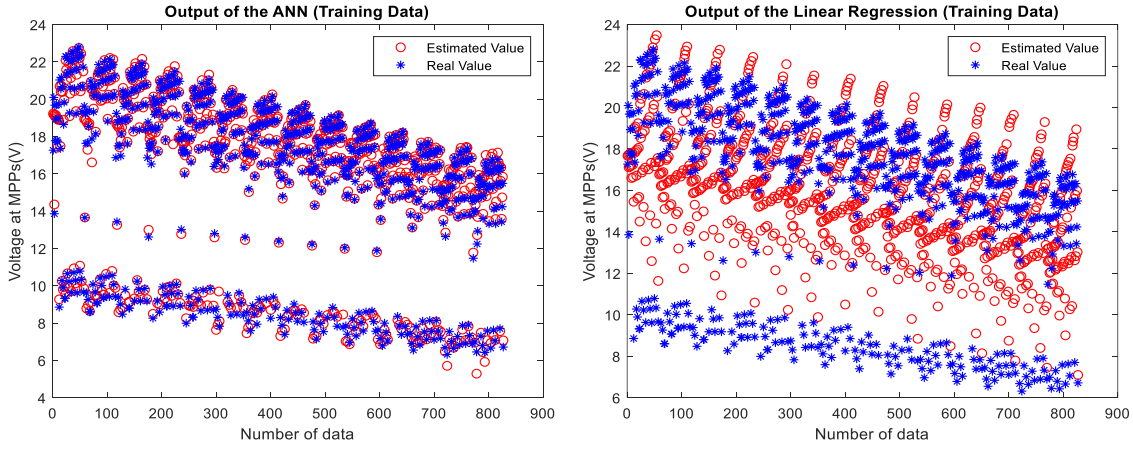

Figure A.1: The output of the ANN and linear regression models for training data.

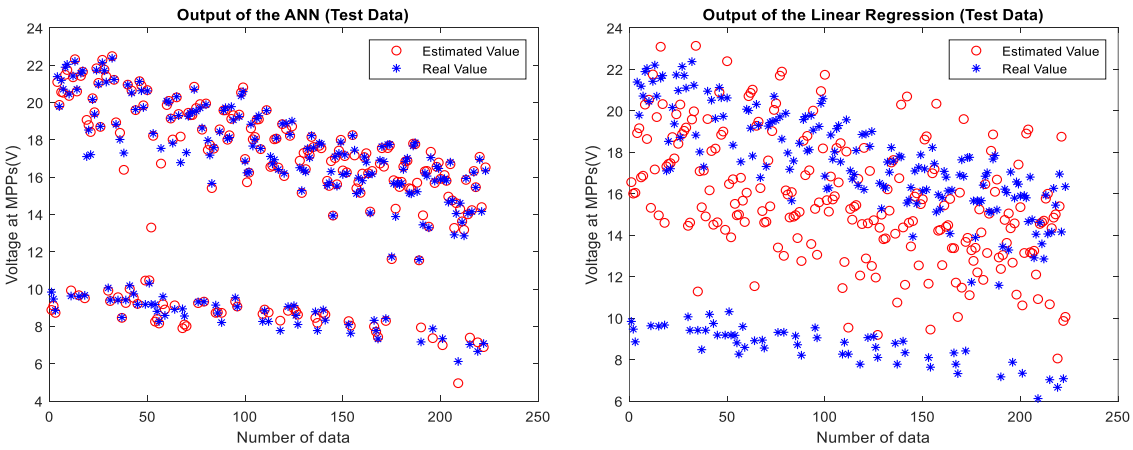

Figure A.2: The output of the ANN and linear regression models for test data.

Appendix B

The Codes for TMS320F335 to Implement the ANN Model

The ANN model was trained in MATLAB software and then the matrices and vectors associated with coefficients and bias values for the hidden layers and output layer were extracted. These values were used in the DSP codes as follows:

```
float32  input_coeff[5][5] = {{0.0755, −1.3923, −2.6250, 15.1610, 0},
                              {1.3729, 0.4663, −14.9845, 9.3237, 0},
                              {0.0219, −0.5447, 1.0075, −19.1421, 0},
                              {−0.1840, −1.8049, −0.1603, 1.7587, 0},
                              {0.1093, −0.0634, −0.0090, 0.0802, 0}};
float32  hidden_one_coeff[5][5] = {{−5.0344, −16.0908, 14.5571, −4.0667, 3.1155},
                                   {−0.6996, −0.0229, −0.0566, −0.1650, 2.0875},
                                   {0.9656, 0.0400, 0.0748, 2.3395, −0.2967},
                                   {−9.0358, 0.9300, 0.1793, 3.1794, 1.9665},
                                   {−2.3297, 5.3535, −3.3218, −5.1711, 1.6562}};
float32  hidden_two_coeff[5] = {−0.5937, −1.8299, −1.3294, −0.3614, 1.1058};
float32  bias_one[5][1] = {{11.1579},
                           {2.0173},
                           {−14.4245},
                           {−1.8145},
                           {0.4257}};
float32  bias_two[5][1] = {{−4.4176},
                           {−0.4566},
                           {2.0179},
                           {−6.5822},
                           {2.6920}};
float32  bias_three = −1.2982;
```

To increase the calculation speed in DSP and avoid the delay, a lookup table is used for *tansig* transfer function instead of using the *math* library. To this end, the output of this function is calculated in MATLAB software for the input values between -5 and 5. To have an acceptable accuracy this range was divided into 200 units.

```
float32  tansig[201] = {−1, −0.9999, −0.9999, −0.9999, −0.9999, −0.9999, −0.9999, −0.9999, −0.9998, −0.9998,
                        −0.9998, −0.9998, −0.9997, −0.9997, −0.9997, −0.9996, −0.9996, −0.9996, −0.9995, −0.9994,
                        −0.9994, −0.9993, −0.9992, −0.9991, −0.9990, −0.9989, −0.9988, −0.9987, −0.9986, −0.9984,
                        −0.9982, −0.9980, −0.9978, −0.9976, −0.9973, −0.9970, −0.9967, −0.9964, −0.9960, −0.9956,
                        −0.9951, −0.9946, −0.9940, −0.9934, −0.9927, −0.9919, −0.9911, −0.9901, −0.9891, −0.9879,
                        −0.9867, −0.9853, −0.9837, −0.9820, −0.9801, −0.9781, −0.9758, −0.9733, −0.9705, −0.9674,
                        −0.9641, −0.9604, −0.9563, −0.9518, −0.9469, −0.9414, −0.9355, −0.9289, −0.9217, −0.9138,
                        −0.9052, −0.8957, −0.8854, −0.8741, −0.8618, −0.8483, −0.8337, −0.8178, −0.8005, −0.7819,
                        −0.7616, −0.7398, −0.7163, −0.6911, −0.6641, −0.6352, −0.6044, −0.5717, −0.5371, −0.5006,
                        −0.4622, −0.4219, −0.3800, −0.3364, −0.2914, −0.2450, −0.1974, −0.1489, −0.09970, −0.05000,
                        0, 0.04990, 0.09960, 0.1488, 0.1973, 0.2449, 0.2913, 0.3363, 0.3799, 0.4218, 0.4621, 0.5005,
                        0.5370, 0.5716, 0.6043, 0.6351, 0.6640, 0.6910, 0.7162, 0.7397, 0.7615, 0.7818, 0.8004, 0.8177,
                        0.8336, 0.8482, 0.8617, 0.8740, 0.8853, 0.8956, 0.9051, 0.9137, 0.9216, 0.9288, 0.9354, 0.9413,
                        0.9468, 0.9517, 0.9562, 0.9603, 0.9640, 0.9673, 0.9704, 0.9732, 0.9757, 0.9780, 0.9800, 0.9819,
                        0.9836, 0.9852, 0.9866, 0.9878, 0.9890, 0.9900, 0.9910, 0.9918, 0.9926, 0.9933, 0.9939, 0.9945,
                        0.9950, 0.9955, 0.9959, 0.9963, 0.9966, 0.9969, 0.9972, 0.9975, 0.9977, 0.9979, 0.9981, 0.9983,
                        0.9985, 0.9986, 0.9987, 0.9988, 0.9989, 0.9990, 0.9991, 0.9992, 0.9993, 0.9993, 0.9994, 0.9995,
                        0.9995, 0.9995, 0.9996, 0.9996, 0.9996, 0.9997, 0.9997, 0.9997, 0.9997, 0.9998, 0.9998, 0.9998,
                        0.9998, 0.9998, 0.9998, 0.9998, 0.9999};
```

The ANN model is used when the MPPT algorithm is initialized to estimate the initial points. Some subroutines are written for matrices and vector multiplication and the lookup table is used for the *tansig* transfer function.

```
if(go_initial == 1)
                {
                Matrix_Multiply(input_coeff, input_vector, res_mul_vec);
                Sum_Vec(res_mul_vec, bias_one, res_sum_vec);
                tsig_fun(res_sum_vec, res_tsig_vec);

                Matrix_Multiply(hidden_one_coeff, res_tsig_vec, res_mul_vec);
                Sum_Vec(res_mul_vec, bias_two, res_sum_vec);
                tsig_fun(res_sum_vec, res_tsig_vec);

                Vec_Multiply(hidden_two_coeff, res_tsig_vec);
                output_real = output_scale + bias_three;
                output_voltage = (output_real + 1.0)/out_data_gain + out_data_offset;

                check_one = input_vector[2][0];
                check_two = input_vector[3][0];
                check_three = d_one;
                check_four = d_two;
                check_five = output_voltage;

                Cur_sf2 = ((output_voltage * 2.0) − 8.0)/50.0;

                PSO_One = Cur_sf2;
                PSO_Two = Cur_sf2 + 0.1;
                PSO_Three = Cur_sf2 − 0.1;
                Pow_One = 0;
                Pow_Two = 0;
                Pow_Three = 0;

                go_on = 1;
                PSO_Initial = 1;
                PSO_Counter = 0;
                }
```

```
void   Matrix_Multiply(float32Mat[5][5], float32vec[5][1], float32out_vec_mul[5][1])
{
    for(ic = 0; ic < 5; ic + +)
      {
        out_vec_mul[ic][0] = 0;
      }
    for(ic = 0; ic < 5; ic + +)
      {
        for(jc = 0; jc < 5; jc + +)
          {
            out_vec_mul[ic][0] = out_vec_mul[ic][0] + Mat[ic][jc] * vec[jc][0];
          }
      }
}
void   Sum_Vec(float32vec_one[5][1], float32vec_two[5][1], float32out_vec_sum[5][1])
{
    for(ic = 0; ic < 5; ic + +)
      {
        out_vec_sum[ic][0] = 0;
      }
    for(ic = 0; ic < 5; ic + +)
      {
        out_vec_sum[ic][0] = vec_one[ic][0] + vec_two[ic][0];
      }
}
void   tsig_fun(float32vec_in_fun[5][1], float32vec_out_fun[5][1])
{
    float32index_fun_f;
    Uint16index_fun_i;
    for(ic = 0; ic < 5; ic + +)
      {
        if(vec_in_fun[ic][0] < −5)
          {
            vec_out_fun[ic][0] = −1;
          }
        if(vec_in_fun[ic][0] > 5)
          {
            vec_out_fun[ic][0] = 1;
          }
        if((vec_in_fun[ic][0] >= −5)&(vec_in_fun[ic][0] <= 5))
          {
            index_fun_f = vec_in_fun[ic][0] * 20.0 + 100.0;
            index_fun_i = index_fun_f;
            vec_out_fun[ic][0] = tansig[index_fun_i];
          }
      }
}
void   Vec_Multiply(float32Vec_inn_one[5], float32vec_inn_two[5][1])
  {
    output_scale = 0.0;
    for(ic = 0; ic < 5; ic + +)
      {
        output_scale = output_scale + Vec_inn_one[ic] * vec_inn_two[ic][0];
      }
}
```

The following codes were used for the PSO MPPT algorithm. The initial particles for the traditional PSO method are chosen randomly while these values are calculated from the ANN model as its codes are shown above.

```
if(PSO_Initial == 0)
{
  if(PSO_Counter == 1)
    {
      Pow_Three = Cur_Pow;
      if(Pow_Three > PSO_Three_Power)
        {
          PSO_Three_Power = Pow_Three;
          PSO_Three_Ind = PSO_Three;
        }
      if(Pow_Three > PSO_Best_Power)
        {
          PSO_Best_Power = Pow_Three;
          PSO_Best_Ind = PSO_Three;
        }
      PSO_One_Next = PSO_One + Omega * (PSO_One - PSO_One_Previous)+
                     PSO_Coeff_One * Rand_Num_One * (PSO_Best_Ind - PSO_One)+
                     PSO_Coeff_Two * Rand_Num_Two * (PSO_One_Ind - PSO_One);
      New_sf2 = PSO_One_Next;
      PSO_One_Previous = PSO_One;
      PSO_One = PSO_One_Next;
    }
  if(PSO_Counter == 2)
    {
      Pow_One = Cur_Pow;
      if(Pow_One > PSO_One_Power)
        {
          PSO_One_Power = Pow_One;
          PSO_One_Ind = PSO_One;
        }
      if(Pow_One > PSO_Best_Power)
        {
          PSO_Best_Power = Pow_One;
          PSO_Best_Ind = PSO_One;
        }
      PSO_Two_Next = PSO_Two + Omega * (PSO_Two - PSO_Two_Previous)+
                     PSO_Coeff_One * Rand_Num_One * (PSO_Best_Ind - PSO_Two)+
                     PSO_Coeff_Two * Rand_Num_Two * (PSO_Two_Ind - PSO_Two);
      New_sf2 = PSO_Two_Next;
      PSO_Two_Previous = PSO_Two;
      PSO_Two = PSO_Two_Next;
    }
  if(PSO_Counter == 3)
    {
      Pow_Two = Cur_Pow;
      if(Pow_Two > PSO_Two_Power)
        {
          PSO_Two_Power = Pow_Two;
          PSO_Two_Ind = PSO_Two;
        }
      if(Pow_Two > PSO_Best_Power)
        {
          PSO_Best_Power = Pow_Two;
          PSO_Best_Ind = PSO_Two;
        }
      PSO_Three_Next = PSO_Three + Omega * (PSO_Three - PSO_Three_Previous)+
                       PSO_Coeff_One * Rand_Num_One * (PSO_Best_Ind - PSO_Three)+
                       PSO_Coeff_Two * Rand_Num_Two * (PSO_Two_Ind - PSO_Three);
      New_sf2 = PSO_Three_Next;
      PSO_Three_Previous = PSO_Three;
      PSO_Three = PSO_Three_Next;
    }
```

```
    if(New_sf2 > 0.9)
      {
        New_sf2 = 0.9;
      }
    if(New_sf2 < 0.1)
      {
        New_sf2 = 0.1;
      }

    go_initial = 0;
    counter = 0;
}
```

Appendix C

The Signal Conditioning and Optocoupler Circuit

The TMS320F28335 DSP operates with 3.3 V signal level while the boost power optimizer works with the logic signal at 5 V level. Also, buffering the output PWM signals of the microcontroller is essential to avoid overloading the device. Other requirements such as protecting the PWM signals from overlapping are required. Therefore, an interface circuit was designed which is shown in Fig. C.1 and Fig. C.2. The high-speed 6N137 optocoupler is used at the output stage while the buffer IC (74HC245), logic gate NOT (74LS04), and logic gate AND (74LS08) are utilized at the input stage. This board can handle 8 PWM signals with a maximum frequency of $10MHz$, therefore, it has enough bandwidth for power electronic applications.

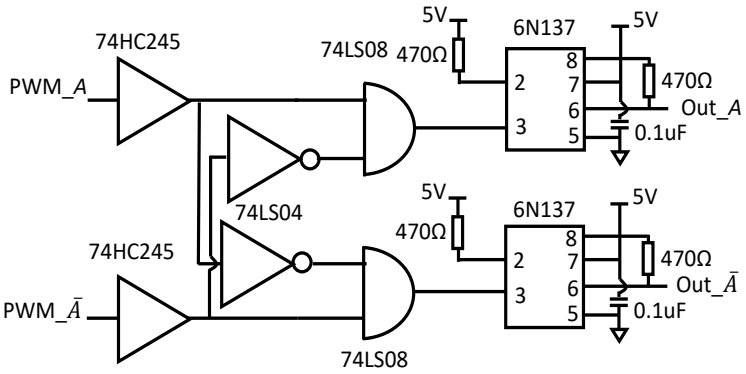

Figure C.1: The signal conditioning and optocoupler circuit for phase A and its complementary.

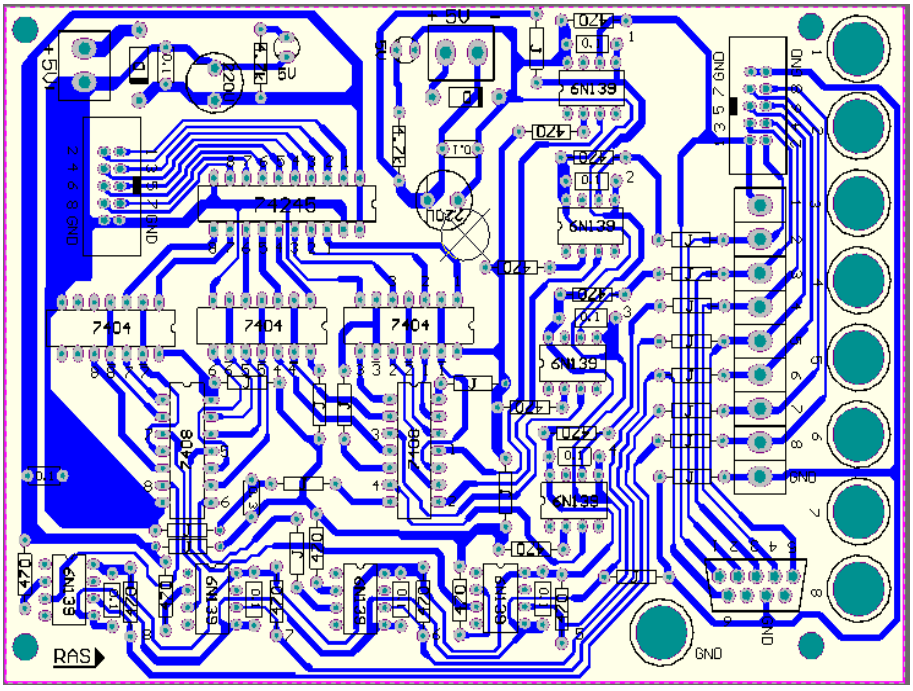

Figure C.2: The signal conditioning and optocoupler PCB.

Bibliography

[1] Union of Concerned Scientists, "Benefits of Renewable Energy Use," https://www.ucsusa.org/resources/benefits-renewable-energy-use, December 2017.

[2] PVcase, "Renewable energy and grid stability: modern infrastructure challenges and solutions," https://pvcase.com/blog/renewable-energy-and-grid-stability-modern-infrastructure-..., February 2024.

[3] Government of Canada, "About renewable energy in Canada," https://natural-resources.canada.ca/our-natural-resources/energy-sources-distribution/renewable-energy/about-renewable-energy-canada/7295, April 2024.

[4] Government of Canada, "Solar Photovoltaic Energy," https://natural-resources.canada.ca/energy/energy-sources-distribution/renewables/solar-photovoltaic-energy/7303, January 2024.

[5] IEA, "Solar PV," https://www.iea.org/energy-system/renewables/solar-pv, July 2023.

[6] REGEN Power, "Which renewable energy is better, wind or solar?," https://regenpower.com/which-renewable-energy-is-better-wind-or-solar/#:~:text=Solar%20energy%20provides%20a%20more,roofs%20of%20houses%20or%20offices., 2024.

[7] Statista, "Cumulative installed capacity of solar photovoltaic power in Canada from 2010 to 2023," https://www.statista.com/statistics/790547/cumulative-installed-solar-pv-power-capacity-in-canada/#:~:text=Solar%20power%20capacity%20in%20Canada,capacity%20of%20100%20megawatts%20each., April 2024.

[8] GREENLANCER, "7 New Solar Panel Technology Trends Shaping the Future of Energy," https://www.greenlancer.com/post/solar-panel-technology-trends#:~:text=Some%20of%20the%20latest%20solar,technology%20to%20streamline%20system%20management., June 2024.

[9] NASA TECHNOLOGY TRANSFER PROGRAM, "Power Generation And Storage High-Efficiency Solar Cell (LEW-TOPS-50)," https://technology.nasa.gov/patent/LEW-TOPS-50., Patent: 9,117,948 9,418,844.

[10] Our World in Data, "Solar photovoltaic module price," https://ourworldindata.org/grapher/solar-pv-prices., May 2024.

[11] M. Kumar, J. C. Rosas-Caro, K. P. Panda, A. Valderrabano-Gonzalez, and G. Panda, "Comprehensive Review of Conventional and Emerging Maximum Power Point Tracking Algorithms for Uniformly and Partially Shaded Solar Photovoltaic Systems," IEEE Access, vol. 11, pp. 31778-31812, March 2023.

[12] S. H. Hanzaei, S. A. Gorji, and M. Ektesabi, "A Scheme-Based Review of MPPT Techniques With Respect to Input Variables Including Solar Irradiance and PV Arrays' Temperature," IEEE Access, vol. 8, pp. 182229-182239, October 2020.

[13] M. D. O. Silva, R. F. Calili, and D. R. Louzada, "Comparative Review of MPPT Algorithms," IEEE 48th Photovoltaic Specialists Conference (PVSC), June 2021.

[14] A. Ali, K. Almutairi, S. Padmanaban, V. Tirth, S. Algarni, K. Irshad, S. Islam, M. H. Zahir, M. Shafiullah, and M. Z. Malik, "Investigation of MPPT Techniques Under Uniform and Non-Uniform Solar Irradiation Condition–A Retrospection," IEEE Access, vol. 8, July 2020.

[15] R. B. Bollipo, S. Mikkili, and P. K. Bonthagorla, "Hybrid, optimal, intelligent and classical PV MPPT techniques: A review," CSEE Journal of Power and Energy Systems, vol. 7, no. 1, pp. 9-33, August 2020.

[16] K. Y. Yap, C. R. Sarimuthu, and J. M.-Y. Lim, "Artificial Intelligence Based MPPT Techniques for Solar Power System: A review," Journal of Modern Power Systems and Clean Energy, vol. 8, no. 6, pp. 1043-1059, October 2020.

[17] J. Dadkhah, and M. Niroomand, "Optimization Methods of MPPT Parameters for PV Systems: Review, Classification, and Comparison," Journal of Modern Power Systems and Clean Energy, vol. 9, no. 2, pp. 225-236, January 2021.

[18] M. Joisher, D. Singh, S. Taheri, D. R. Espinoza-Trejo, E. Pouresmaeil and H. Taheri, "A Hybrid Evolutionary-Based MPPT for Photovoltaic Systems Under Partial Shading Conditions," IEEE Access, vol. 8, pp. 38481-38492, February 2020.

[19] N. Femia, G. Petrone, G. Spagnuolo, and M. Vitelli, "Optimization of perturb and observe maximum power point tracking method," IEEE Transactions on Power Electronics, vol. 20, no. 4, pp. 963–973, July 2005.

[20] M. Kumar, R. Bharti, and D. V. S. K. K. Rao, "Conventional and hybrid perturb & observe based maximum power point tracking for solar system," International Conference on Vision Towards Emerging Trends in Communication and Networking (ViTECoN), March 2019.

[21] D. Sera, L. Mathe, T. Kerekes, S. V. Spataru, and R. Teodorescu, "On the perturb-and-observe and incremental conductance MPPT methods for PV systems," IEEE Journal of Photovoltaics, vol. 3, no. 3, pp. 1070–1078, July 2013.

[22] W. Zhu, L. Shang, P. Li, and H. Guo, "Modified hill climbing MPPT algorithm with reduced steady-state oscillation and improved tracking efficiency," The Journal of Engineering, vol. 2018, no. 17, pp. 1878-1883, November 2018.

[23] M. I. Bahari, P. Tarassodi, Y. M. Naeini, A. K. Khalilabad, and P. Shirazi, "Modeling and simulation of Hill climbing MPPT algorithm for photovoltaic application," International Symposium on Power Electronics, Electrical Drives, Automation and Motion (SPEEDAM), June 2016.

[24] D. Sera, L. Mathe, T. Kerekes, S. V. Spataru, and R. Teodorescu, "On the perturb-and-observe and incremental conductance MPPT methods for PV systems," IEEE Journal of Photovoltaics, vol. 3, no. 3, pp. 1070–1078, July 2013.

[25] S. Khadidja, M. Mountassar, and B. M'hamed, "Comparative study of incremental conductance and perturb & observe MPPT methods for photovoltaic system," International Conference on Green Energy Conversion Systems (GECS), March 2017.

[26] H. Al-Atrash, I. Batarseh, and Khalid Rustom, "Effect of Measurement Noise and Bias on Hill-Climbing MPPT Algorithms," IEEE Transactions on Aerospace and Electronic Systems, vol. 46, no. 2, pp. 745-760, April 2010.

[27] E. M. Ahmed and M. Shoyama, "Novel stability analysis of variable step size incremental resistance INR MPPT for PV systems," 37th Annual Conference of the IEEE Industrial Electronics Society (IECON), November 2011.

[28] S. Jain and V. Agarwal, "A new algorithm for rapid tracking of approximate maximum power point in photovoltaic systems," IEEE Power Electronics Letters, vol. 2, no. 1, pp. 16–19, March 2004.

[29] X. Li, H. Wen, Y. Hu, L. Jiang, and W. Xiao, "Modified beta algorithm for GMPPT and partial shading detection in photovoltaic systems," IEEE Transactions on Power Electronics, vol. 33, no. 3, pp. 2172–2186, March 2018.

[30] H. Wang, L. Vinayagam, H. Jiang, Z. Q. Cai, and H. Li, "New MPPT solar generation implemented with constant-voltage constant-current DC/DC converter," 51st International Universities Power Engineering Conference (UPEC), September 2016.

[31] S. Malathy and R. Ramaprabha, ”Maximum Power Point Tracking Based on Look Up Table Approach,” Advanced Materials Research, vol. 768, pp. 124–130, September 2013.

[32] J. K. Udavalakshmi and M. S. Sheik, ”Comparative study of perturb & observe and look-up table maximum power point tracking techniques using MATLABISimulink,” International Conference on Current Trends towards Converging Technologies (ICCTCT), March 2018.

[33] A. M. Farayola, A. N. Hasan, and A. Ali, ”Curve fitting polynomial technique compared to ANFIS technique for maximum power point tracking,” 8th International Renewable Energy Congress (IREC), March 2017.

[34] M. Seyedmahmoudian, R. Rahmani, S. Mekhilef, A. M. T. Oo, A. Stojcevski, T. K. Soon and A. S. Ghandhari, "Simulation and Hardware Implementation of New Maximum Power Point Tracking Technique for Partially Shaded PV System Using Hybrid DEPSO Method," IEEE Transactions on Sustainable Energy, vol. 6, no. 3, pp. 850-862, April 2015.

[35] M. Kermadi, Z. Salam, J. Ahmed and E. M. Berkouk, "An Effective Hybrid Maximum Power Point Tracker of Photovoltaic Arrays for Complex Partial Shading Conditions," IEEE Transactions on Industrial Electronics, vol. 66, no. 9, pp. 6990-7000, Oct. 2018.

[36] H. Li, D. Yang, W. Su, J. Lu and X. Yu, "An Overall Distribution Particle Swarm Optimization MPPT Algorithm for Photovoltaic System Under Partial Shading," IEEE Transactions on Industrial Electronics, vol. 66, no. 1, pp. 265-275, April 2018.

[37] C. Manickam, G. R. Raman, G. P. Raman, S. I. Ganesan and C. Nagamani, "A Hybrid Algorithm for Tracking of GMPP Based on P&O and PSO With Reduced Power Oscillation in String Inverters," IEEE Transactions on Industrial Electronics, vol. 63, no. 10, pp. 6097-6106, July 2016.

[38] K. L. Lian, J. H. Jhang and I. S. Tian, "A Maximum Power Point Tracking Method Based on Perturb-and-Observe Combined With Particle Swarm Optimization," IEEE Journal of Photovoltaics, vol. 4, no. 2, pp. 626-633, Jan. 2014.

[39] S. Javed, K. Ishaque, S. A. Siddique and Z. Salam, "A Simple Yet Fully Adaptive PSO Algorithm for Global Peak Tracking of Photovoltaic Array Under Partial Shading Conditions," IEEE Transactions on Industrial Electronics, vol. 69, no. 6, pp. 5922-5930, June 2022.

[40] S. Obukhov, A. Ibrahim, A. A. Z. Diab, A. S. A. Sumaiti and R. Aboelsaud, "Optimal Performance of Dynamic Particle Swarm Optimization Based Maximum Power Trackers for Stand-Alone PV System Under Partial Shading Conditions," IEEE Access, vol. 8, pp. 20770-20785, Jan. 2020.

[41] R. B. A. Koad, A. F. Zobaa and A. El-Shahat, "A Novel MPPT Algorithm Based on Particle Swarm Optimization for Photovoltaic Systems," IEEE Transactions on Sustainable Energy, vol. 8, no. 2, pp. 468-476, April 2017.

[42] K. Guo, L. Cui, M. Mao, L. Zhou and Q. Zhang, "An Improved Gray Wolf Optimizer MPPT Algorithm for PV System With BFBIC Converter Under Partial Shading," IEEE Access, vol. 8, pp. 103476-103490, June 2020.

[43] S. Mohanty, B. Subudhi, and P. K. Ray, "A New MPPT Design Using Grey Wolf Optimization Technique for Photovoltaic System Under Partial Shading Conditions," IEEE Transactions on Sustainable Energy, vol. 7, no. 1, pp. 181-188, January 2016.

[44] I. S. Millah, P. C. Chang, D. F. Teshome, R. K. Subroto, K. L. Lian, and J.-F. Lin, "An Enhanced Grey Wolf Optimization Algorithm for Photovoltaic Maximum Power Point Tracking Control Under Partial Shading Conditions," vol. 3, pp. 392-408, May 2022.

[45] S. Mohanty, B. Subudhi, and P. K. Ray, "A Grey Wolf-Assisted Perturb & Observe MPPT Algorithm for a PV System," IEEE Transactions on Energy Conversion, vol. 32, no. 1, pp. 340-347, March 2017.

[46] H. Gundogdu, A. Demirci, S. M. Tercan, and U. Cali, "A Novel Improved Grey Wolf Algorithm Based Global Maximum Power Point Tracker Method Considering Partial Shading," IEEE Access, vol. 12, pp. 6148-6159, January 2024.

[47] J. Ahmed and Z. Salam, "A maximum power point tracking (MPPT) for PV system using cuckoo search with partial shading capability," Applied Energy, vol. 119, pp. 118–130, April 2014.

[48] S. K. Sahoo, M. Balamurugan, S. Anurag, R. Kumar, and V. Priya, "Maximum power point tracking for PV panels using ant colony optimization," Innovations in Power and Advanced Computing Technologies (i-PACT), April 2017.

[49] C. González-Castaño, C. Restrepo, S. Kouro, and J. Rodriguez, "MPPT Algorithm Based on Artificial Bee Colony for PV System," IEEE Access, vol. 9, March 2021.

[50] Y. P. Huang, M. Y. Huang and C. E. Ye, "A Fusion Firefly Algorithm With Simplified Propagation for Photovoltaic MPPT Under Partial Shading Conditions," IEEE Transactions on Sustainable Energy, vol. 11, no. 4, pp. 2641-2652, Oct. 2020.

[51] R. Motamarri, and N. Bhookya, "JAYA Algorithm Based on Lévy Flight for Global MPPT Under Partial Shading in Photovoltaic System," IEEE Journal of Emerging and Selected Topics in Power Electronics, vol. 9, no. 4, pp. 4979-4991, August 2021.

[52] I. Shams, S. Mekhilef and K. S. Tey, "Improved-Team-Game-Optimization-Algorithm-Based Solar MPPT With Fast Convergence Speed and Fast Response to Load Variations," IEEE Transactions on Industrial Electronics, vol. 68, no. 8, pp. 7093-7103, Aug. 2021.

[53] S. G. Malla, P. Malla, J. M. R. Malla, R. Singla, P. Choudekar, R. Koilada and M. K. Sahu, "Whale Optimization Algorithm for PV based Water Pumping System Driven by BLDC Motor Using Sliding Mode Controller," IEEE Journal of Emerging and Selected Topics in Power Electronics, Early Access.

[54] K. S. Tey, S. Mekhilef, M. Seyedmahmoudian, B. Horan, A. T. Oo, and A. Stojcevski, "Improved Differential Evolution-Based MPPT Algorithm Using SEPIC for PV Systems Under Partial Shading Conditions and Load Variation," IEEE Transactions on Industrial Informatics, vol. 14, no. 10, pp. 4322-4333, October 2018.

[55] N. Kumar, I. Hussain, B. Singh, and B. K. Panigrahi, "Rapid MPPT for Uniformly and Partial Shaded PV System by Using JayaDE Algorithm in Highly Fluctuating Atmospheric Conditions," IEEE Transactions on Industrial Informatics, vol. 13, no. 5, pp. 2406-2416, October 2016.

[56] M. Seyedmahmoudian, R. Rahmani, S. Mekhilef, A. M. T. Oo, and A. Stojcevski, "Simulation and Hardware Implementation of New Maximum Power Point Tracking Technique for Partially Shaded PV System Using Hybrid DEPSO Method," IEEE Transactions on Sustainable Energy, vol. 6, no. 3, pp. 850-862, July 2015.

[57] N. Kumar, I. Hussain, B. Singh, and B. K. Panigrahi, "MPPT in Dynamic Condition of Partially Shaded PV System by Using WODE Technique," IEEE Transactions on Sustainable Energy, vol. 8, no. 3, pp. 1204-1214, July 2017.

[58] P. Manoharan, U. Subramaniam, T. S. Babu, S. Padmanaban, J. B. Holm-Nielsen, M. Mitolo and S. Ravichandran, "Improved Perturb and Observation Maximum Power Point Tracking Technique for Solar Photovoltaic Power Generation Systems," IEEE Systems Journal, vol. 15, no. 2, pp. 3024 - 3035, June 2021.

[59] C. Pradhan, M. K. Senapati, S. G. Malla, P. K. Nayak and T. Gjengedal, "Coordinated Power Management and Control of Standalone PV-Hybrid System With Modified IWO-Based MPPT," IEEE Systems Journal, vol. 15, no. 3, pp. 3585-3596, Sep. 2020.

[60] J. P. Ram, D. S. Pillai, N. Rajasekar and S. M. Strachan, "Detection and Identification of Global Maximum Power Point Operation in Solar PV Applications Using a Hybrid ELPSO-P&O Tracking Technique," IEEE Journal of Emerging and Selected Topics in Power Electronics, vol. 8, no. 2, pp. 1361-1374, Feb. 2019.

[61] S. Mohanty, B. Subudhi and P. K. Ray, "A Grey Wolf-Assisted Perturb & Observe MPPT Algorithm for a PV System," IEEE Transactions on Energy Conversion, vol. 32, no. 1, pp. 340-347, March 2017.

[62] X. Meng, F. Gao, T. Xu and C. Zhang, "Fast Two-Stage Global Maximum Power Point Tracking for Grid-Tied String PV Inverter Using Characteristics Mapping Principle," IEEE Journal of Emerging and Selected Topics in Power Electronics, vol. 10, no. 1, pp. 564-574, Feb. 2022.

[63] H. M. El-Helw, A. Magdy and M. I. Marei, "A Hybrid Maximum Power Point Tracking Technique for Partially Shaded Photovoltaic Arrays," IEEE Access, vol. 5, pp. 11900-11908, June 2017.

[64] W. Zhang, G. Zhou, H. Ni and Y. Sun, "A Modified Hybrid Maximum Power Point Tracking Method for Photovoltaic Arrays Under Partially Shading Condition," IEEE Access, vol. 7, pp. 160091-160100, Oct. 2019.

[65] S. Allahabadi, H. Iman-Eini and S. Farhangi, "Fast Artificial Neural Network Based Method for Estimation of the Global Maximum Power Point in Photovoltaic Systems," IEEE Transactions on Industrial Electronics, vol. 69, no. 6, pp. 5879-5888, June 2022.

[66] S. Hosseini, S. Taheri, M. Farzaneh, H. Taheri, "A High-Performance Shade-Tolerant MPPT Based on Current-Mode Control," IEEE Transactions on Power Electronics, vol. 34, no. 10, pp. 10327-10340, October 2019.

[67] A. M. S. Furtado, F. Bradaschia, M. C. Cavalcanti and L. R. Limongi, "A Reduced Voltage Range Global Maximum Power Point Tracking Algorithm for Photovoltaic Systems Under Partial Shading Conditions," IEEE Transactions on Industrial Electronics, vol. 65, no. 4, pp. 3252-3262, April 2018.

[68] J. Ahmed and Z. Salam, "An Accurate Method for MPPT to Detect the Partial Shading Occurrence in a PV System," IEEE Transactions on Industrial Informatics, vol. 13, no. 5, pp. 2151-2161, October 2017.

[69] K. Chen, S. Tian, Y. Cheng and L. Bai, "An Improved MPPT Controller for Photovoltaic System Under Partial Shading Condition," IEEE Transactions on Sustainable Energy, vol. 5, no. 2, pp. 978-985, July 2014.

[70] S. Selvakumar, M. Madhusmita, C. Koodalsamy, S. P. Simon and Y. R. Sood, "High-Speed Maximum Power Point Tracking Module for PV Systems," IEEE Transactions on Industrial Electronics, vol. 66, no. 2, pp. 1119-1129, Feb. 2019.

[71] E. I. Batzelis, S. A. Papathanassiou and B. C. Pal, "PV System Control to Provide Active Power Reserves Under Partial Shading Conditions," IEEE Transactions on Power Electronics, vol. 33, no. 11, pp. 9163-9175, November 2018.

[72] A. Ramyar, H. Iman-Eini and S. Farhangi, "Global Maximum Power Point Tracking Method for Photovoltaic Arrays Under Partial Shading Conditions," IEEE Transactions on Industrial Electronics, vol. 64, no. 4, pp. 2855-2864, April 2017.

[73] R. Kotti and W. Shireen, "Efficient MPPT control for PV systems adaptive to fast changing irradiation and partial shading conditions," Solar Energy, vol. 114, pp. 397-407, March 2015.

[74] D. Vinnikov, R. Kosenko, A. Chub, and E. Liivik, "Shade-tolerant photovoltaic microinverter with time adaptive seamless P-V curve sweep MPPT," 19th European Conference on Power Electronics and Applications (EPE'17 ECCE Europe), September 2017.

[75] S. Madichetty, S. Mishra and A. J. Neroth, "Maximum Power Point in a Single Step: A Novel Method for PV Industry," IEEE Power Electronics Magazine, vol. 8, no. 3, pp. 48-54, September 2021.

[76] A. F. Murtaza, H. A. Sher, K. Al-Haddad and F. Spertino, "Module Level Electronic Circuit Based PV Array for Identification and Reconfiguration of Bypass Modules," IEEE Transactions on Energy Conversion, vol. 36, no. 1, pp. 380-389, March 2021.

[77] P. K. Peter and V. Agarwal, "On the Input Resistance of a Reconfigurable Switched Capacitor DC-DC Converter-Based Maximum Power Point Tracker of a Photovoltaic Source," IEEE Transactions on Power Electronics, vol. 27, no. 12, pp. 4880-4893, December 2012.

[78] Y. Kuai and S.Yuvarajan, "An electronic load for testing photovoltaic panels," Journal of Power Sources, vol. 154, no. 1, pp. 308-313, March 2006.

[79] A. G. Galeano, M. Bressan, F. J. Vargas and C. Alonso, "Shading Ratio Impact on Photovoltaic Modules and Correlation with Shading Patterns," Energies, vol. 11, no. 4:852, April 2018.

[80] Y. Mahmoud and E. F. El-Saadany, "A Novel MPPT Technique Based on an Image of PV Modules," IEEE Transactions on Energy Conversion, vol. 32, no. 1, pp. 213-221, March 2017.

[81] M. K. A. Smadi and Y. Mahmoud, "Image-Based Differential Power Processing for Photovoltaic Microinverter," IEEE Transactions on Energy Conversion, vol. 36, no. 2, pp. 619-628, June 2021.

[82] M. Dhimish, V. Holmes, B. Mehrdadi, M. Dales and P. Mather, "Output-Power Enhancement for Hot Spotted Polycrystalline Photovoltaic Solar Cells," IEEE Transactions on Device and Materials Reliability, vol. 18, no. 1, pp. 37-45, March 2018.

[83] Y. Hu, W. Cao, J. Wu, B. Ji and D. Holliday, "Thermography-Based Virtual MPPT Scheme for Improving PV Energy Efficiency Under Partial Shading Conditions," IEEE Transactions on Power Electronics, vol. 29, no. 11, pp. 5667-5672, Nov. 2014.

[84] J. H. Teng, H. C. Wu, Z. H. Wu and W. H. Huang, "Efficient Partial Shading Detection for Photovoltaic Generation Systems," IEEE Transactions on Sustainable Energy, vol. 14, no. 4, pp. 2249-2259, Oct. 2023.

[85] J. Ahmed and Z. Salam, "An Accurate Method for MPPT to Detect the Partial Shading Occurrence in a PV System," IEEE Transactions on Industrial Informatics, vol. 13, no. 5, pp. 2151-2161, Oct. 2017.

[86] J. Ahmed and Z. Salam, "An Enhanced Adaptive P&O MPPT for Fast and Efficient Tracking Under Varying Environmental Conditions," IEEE Transactions on Sustainable Energy, vol. 9, no. 3, pp. 1487-1496, July 2018.

[87] M. Z. Ramli and Z. Salam, "A Simple Energy Recovery Scheme to Harvest the Energy from Shaded Photovoltaic Modules During Partial Shading," IEEE Transactions on Power Electronics, vol. 29, no. 12, pp. 6458-6471, Dec. 2014.

[88] S. W. Lee and H. L. Do, "Single-Stage Bridgeless AC–DC PFC Converter Using a Lossless Passive Snubber and Valley Switching," IEEE Transactions on Industrial Electronics, vol. 63, no. 10, pp. 6055-6063, Oct. 2016.

[89] J. M. Wang and S. T. Wu, "A Synchronous Buck DC-DC Converter Using a Novel Dual-Mode Control Scheme to Improve Efficiency," IEEE Transactions on Power Electronics, vol. 32, no. 9, pp. 6983–6993, Sept. 2019.

[90] R. Sangrody, M. Pouresmaeil, M. Marzband and E. Pouresmaeil, "Resonance-based optimized buck LED driver using unequal turn ratio coupled inductance," IEEE Transactions on Power Electronics, Vol. 35, No. 12, pp. 13068-13076, Dec. 2020.

[91] R. Sangrody, H. Sangrody, M. Marzband and E. Pouresmaeil, "Semi-valley switching method for buck LED driver to increase its efficiency and performance," IET Power Electronics, Vol. 13, No. 10, pp. 1966-1973, Aug. 2020.

[92] H. Nene, C. Jiang, and S. Choudhury, "Efficiency and THD Optimization Based on an Interleaved PFC Converter Using Digital Controller with Integrated Valley Switching Control Feature," IEEE Texas Power and Energy Conference (TPEC), February 2019.

[93] H. Nene, C. Jiang and S. Choudhury, "Digital Controller with Integrated Valley Switching Control for Light Load Efficiency and THD Improvements in PFC Converter," IEEE Applied Power Electronics Conference and Exposition (APEC), March 2017.

[94] L. Huber, B. T. Irving and M. M. Jovanovic, "Effect of Valley Switching and Switching-Frequency Limitation on Line-Current Distortions of DCM/CCM Boundary Boost PFC Converters," IEEE Transactions on Power Electronics, vol. 24, no. 2, pp. 339-347, 2009.

[95] R. T. Ryan, J. G. Hayes, R. J. Morrison and D. N. Hogan, "Improved Zero-Crossing Distortion of A Boundary-Conduction-Mode Boost Converter with Digital Average-Current-Mode Control," IEEE Applied Power Electronics Conference and Exposition (APEC), March 2018.

[96] Q. Li, K. Yao, J. Song, H. Xu and Y. Han, "A Series Diode Method of Suppressing Parasitic Oscillation for Boost PFC Converter Operated in Discontinuous Conduction Mode," IEEE Transactions on Power Electronics, vol. 33, no. 1, pp. 407-424, 2018.

[97] X. Ren, Z. Guo, Y. Wu, Z. Zhang and Q Chen, "Adaptive LUT-based Variable On-time Control for CRM Boost PFC Converters," IEEE Transactions on Power Electronics, vol. 33, no. 9, pp. 8123-8136, 2018.

[98] Y. Zhou, X. Ren, Z. Guo, Z. Zhang, Q. Chen and K. Yao, "A More Accurate Variable On-Time Control for CRM Flyback PFC Converters," IEEE Energy Conversion Congress and Exposition (ECCE), May 2018.

[99] C. Zhao and X. Wu, "Accurate Operating Analysis of Boundary Mode Totem-Pole Boost PFC Converter Considering the Reverse Recovery of MOSFET," IEEE Transactions on Power Electronics, vol. 33, no. 12, pp. 10013-10043, 2018.

[100] Y. G. Li, "A Novel Control Scheme of Quasi-Resonant Valley-Switching for High-Power-Factor AC-to-DC LED Driver," IEEE Transactions on Industrial Electronics, vol. 62, no. 8, pp. 4787-4794, 2015.

[101] L. F. L. Villa, T.-P. Ho, J.-C. Crebier and B. Raison, "A Power Electronics Equalizer Application for Partially Shaded Photovoltaic Modules," IEEE Transactions on Industrial Electronics, vol. 60, no. 3, pp. 1179-1190, March 2013.

[102] M. Tahmasbi-Fard, M. Tarafdar-Hagh, S. Pourpayam and A.-A. Haghrah, "A Voltage Equalizer Circuit to Reduce Partial Shading Effect in Photovoltaic String," IEEE Journal of Photovoltaics, vol. 8, no. 4, pp. 1102-1109, July 2018.

[103] A. H. Chang, A.-T. Avestruz and S. B. Leeb, "Capacitor-Less Photovoltaic Cell-Level Power Balancing using Diffusion Charge Redistribution," IEEE Transactions on Power Electronics, vol. 30, no. 2, pp. 537-546, February 2015.

[104] P. S. Shenoy, K. A. Kim, B. B. Johnson and P. T. Krein, "Differential Power Processing for Increased Energy Production and Reliability of Photovoltaic Systems," IEEE Transactions on Power Electronics, vol. 28, no. 6, pp. 2968-2979, June 2013.

[105] P. Sharma and V. Agarwal, "Exact Maximum Power Point Tracking of Grid-Connected Partially Shaded PV Source Using Current Compensation Concept," IEEE Transactions on Power Electronics, vol. 29, no. 9, pp. 4684-4692, September 2014.

[106] H. Delavaripour, B. M. Dehkordi, H. A. Zarchi and E. Adib, "Increasing Energy Capture From Partially Shaded PV String Using Differential Power Processing," IEEE Transactions on Industrial Electronics, vol. 66, no. 10, pp. 7672-7682, October 2019.

[107] P. Sharma and V. Agarwal, "Maximum Power Extraction From a Partially Shaded PV Array Using Shunt-Series Compensation," IEEE Journal of Photovoltaics, vol. 4, no. 4, pp. 1128-1137, July 2014.

[108] A. Chub, D. Vinnikov, R. Kosenko, and E. Liivik, "Wide Input Voltage Range Photovoltaic Microconverter With Reconfigurable Buck–Boost Switching Stage," IEEE Transactions on Industrial Electronics, vol. 64, no. 7, pp. 5974-5983, July 2017.

[109] S. A. Arshadi, B. Poorali, E. Adib, and H. Farzanehfard, "High Step-Up DC–AC Inverter Suitable for AC Module Applications," IEEE Transactions on Industrial Electronics, vol. 63, no. 2, pp. 832-839, February 2016.

[110] J. Ahmed and Z. Salam, "An Improved Method to Predict the Position of Maximum Power Point During Partial Shading for PV Arrays," IEEE Transactions on Industrial Informatics, vol. 11, no. 6, pp. 1378-1387, December 2015.

[111] Z. Bi, J. Ma, K. L. Man, J. S. Smith, Y. Yue and H. Wen, "An Enhanced 0.8VOC-Model-Based Global Maximum Power Point Tracking Method for Photovoltaic Systems," IEEE Transactions on Industry Applications, vol. 56, no. 6, pp. 6825-6834, November-December 2020.

[112] J. Ahmed, and Z. Salam, "An Improved Method to Predict the Position of Maximum Power Point During Partial Shading for PV Arrays," IEEE Transactions on Industrial Informatics, vol. 11, no. 6, pp. 1378-1387, December 2015.

[113] W. D. Soto, S. A. Klein and W. A. Beckman, "Improvement and validation of a model for photovoltaic array performance," Solar Energy, vol. 80, no. 1, pp. 78-88, January 2006.

[114] K. Ishaque, Z. Salam, S. Mekhilef and A. Shamsudin, "Parameter extraction of solar photovoltaic modules using penalty-based differential evolution," Applied Energy, vol. 99, pp. 297-308, November 2012.

[115] J. A. Gow and C. D. Manning, "Development of a model for photovoltaic arrays suitable for use in simulation studies of solar energy conversion systems," Sixth International Conference on Power Electronics and Variable Speed Drives (Conf. Publ. No. 429), September 1996.

[116] H.-L. Tsai, C.-S. Tu and Y.-J. Su, "Development of Generalized Photovoltaic Model Using MATLAB/SIMULINK," Proceedings of the World Congress on Engineering and Computer Science, October 2008.

[117] W. T. d. Costa, J. F. Fardin, D. S. L. Simonetti and L. d. V. B. M. Neto, "Identification of photovoltaic model parameters by Differential Evolution," IEEE International Conference on Industrial Technology, March 2010.

[118] C. Hua, J. Lin and C. Shen, "Implementation of a DSP-controlled photovoltaic system with peak power tracking," IEEE Transactions on Industrial Electronics, vol. 45, no. 1, pp. 99-107, February 1998.

[119] S. Moballegh and J. Jiang, "Partial shading modeling of photovoltaic system with experimental validations," IEEE Power and Energy Society General Meeting, July 2011.

[120] K. A. Kim, G.-S. Seo, B.-H. Cho and P. T. Krein, "Photovoltaic Hot-Spot Detection for Solar Panel Substrings Using AC Parameter Characterization," IEEE Transactions on Power Electronics, vol. 31, no. 2, pp. 1121-1130, February 2016.

[121] G. R.Walker, "Evaluating MPPT converter topologies using a matlab PV model," Journal of Electrical & Electronics Engineering, Australia, vol. 21, no. 1, January 2001.

[122] M. Garaj, H. S. H. Chung, A. W. I Lo and Huai Wang, "Analysis of solar panel's lumped equivalent circuit parameters using LASSO," IEEE Energy Conversion Congress and Exposition (ECCE), Baltimore, MD, USA, 2019.